COVER-DEPTH MODELLING AND ERROR CORRECTION OF OBJECT MAPPING IN REINFORCED CONCRETE STRUCTURES IN THE NEAR-FIELD OF GROUND PENETRATING RADAR

CHAM YUI KEI

PhD

The Hong Kong Polytechnic University

2024

The Hong Kong Polytechnic University

Department of Land Surveying and Geo-Informatics

Cover-Depth Modelling and Error Correction of Object Mapping in Reinforced Concrete Structures in the Near-Field of Ground Penetrating Radar

Cham Yui Kei

A thesis submitted in partial fulfillment of the requirements for the degree of Doctor of Philosophy

April 2022

CERTIFICATE OF ORIGINALITY

I hereby declare that this thesis is my own work and that, to the best of my knowledge and belief, it reproduces no material previously published or written, nor material that has been accepted for the award of any other degree or diploma, except where due acknowledgement has been made in the text.

CHAM Yui Kei

Abstract

The quality of construction works and integrity of building structures are interrelated with the reliability, durability, safety, lifespan and cost efficiency of maintenance for all built structures and elements throughout their entire life. To ensure the quality of work and identify the potential defects as early as possible, inspection and certification of quality of works and material for new works, addition and alteration (A&A) works and modification works, and mandatory regular routine inspection of existing buildings are performed on-site. To save project time and cost, the modern diagnostic technique provides quick, reliable and non-subjective traceable evidence to the engineer prior to making a proper engineering judgment. The modern non-destructive testing and evaluation technique neither not damages the appearance and function of the building element nor interferes with the enjoyment of the user. With the advanced technology development in sensing and intelligent data processing, ground penetrating radar (GPR) offers a powerful nor invasive approach to accurately locate and measure unseen objects inside non-metallic objects and below ground. GPR measures the travelling time of the reflected wave and estimates the object's depth. Thus, GPR is an indirect measurement method, and its vertical measurement accuracy and quality level (QL) are ±40% under QL-B2/2P as set out in Specification for Underground Utility Detection, Verification and Location, PAS:2014 published by the Institution of Civil Engineers (ICE). For cover depth measurement by GPR, relevant code, standards, and specifications regarding accuracy are still in the nurturing stage.

The objective of this study is to develop a standard model to recognize the potential sources of error, minimize and correct the error, and evaluate the uncertainty in the GPR measurement of concrete reinforcement cover. In the beginning, the study focused on recognizing the potential errors from various sources and classified them into three different areas including the host material, the ray-path geometry, and equipment & signal processing (Chapter 3). Then, the study evaluates potential errors through (1) different ray-path models with associated mathematical models, (2) and experimental validation in both air and controlled reinforced concrete samples.

Having reviewed the deficiency of the current single trilateration model under ASTM, models taken into account of the antenna separation and oblique angle, and target object size and depth in semi-trilaterated and full trilaterated ray-path models with associated mathematical

expression respectively were validated by experiment (Chapter 4). The potential sources of error and uncertainty mentioned (Chapter 3) were evaluated based on the experimental results (Chapters 4 and 5). A refined algorithm based on a semi-trilateration model and root mean square error algorithm was developed and tested concerning the confidence level and interval (Chapter 6).

According to the experimental results, the following conclusions were drawn,

(1) Effect of accurate concrete cover depth measurement in the reactive near field and Fresnel region using high-frequency 2GHz antenna – an error ranging from 34.5-136.1% in the near field in comparison to the 1.2-28.2% in the Fresnel region. Accurate measurement in near-field regions is highly limited and is not recommended.
(2) Effect of ages of concrete on accuracies of cover depth measurement – the variation of average estimated depth is 0.13mm and 0.02mm at early Day 56 and at Day 90 and afterwards respectively. The result also showed that the dielectric constants and Two-Way Travel Time were decreasing and became steady, and the peak frequencies were increasing steadily for different cover depths at Day 90 and afterwards over the age of hardened concrete. The result is closely related to the cement hydration process which converts free water to bound water.
(3) Uncertainty, confidence level and interval of refined algorithm based on semi-trilateration method will be defined after experimental validation on real concrete elements.

The abovementioned work provides a standard model and measurement method to accurately estimate the concrete cover depth with comprehensive consideration of different potential sources of errors from the formation of host materials, i.e. fresh concrete to hardened concrete, the use of equipment and signal process, and ray-path and mathematical models. The findings also provide clear guidance to stakeholders, including clients, engineers, surveyors, and operators, on achieving accurate and reliable cover depth measurement with confidence in GPR measurement.

List of publications

Journal papers:

Cham Y.K. & Lai, W.L.W. (2023), "An Experimental Study of GPR Near Field Problem in Depth Ranging of Buried Objects, Hindawi, Advances in Civil Engineering, Vol 2023, Article ID 6865847. (Published)

Cham Y.K. & W.L.W. (Under Review), Effects of ages on accuracies of cover depth measurements by GPR, *Tunnelling and Underground Space Technology*.

Acknowledgements

I would like to express my deepest gratitude to my chief supervisor, Dr Wallace Lai, who has the passion, enthusiasm, and motivation to convey a spirit of excellent research. Without his kindness, patience, and tolerance to help and encourage me, I would not continuously explore new knowledge.

I would also like to sincerely express my appreciation to my co-supervisor Chair Professor C. S. Poon for the instruction and encouragement on my research. His insightful and crucial comments and criticism motivated me to yield a broad scientific perspective and thorough research output.

In addition, a thank you to my LSGI and CEE teammates, Janet, Ray, Phoebe, Xie Fei and Mr. Ho, and Hei gor and Shing gor of CEE, for the inspiring discussion and technical advice, and the sharing of experience and knowledge.

Also, I would like to express my sincere thanks to my friend and ex-colleague Ir Albert KWOK Wing Keung who encouraged and gave strong support to my PhD study. And special thanks to Sr K.K. LO, my ex-colleague from BRE PolyU who initiate me to start up the PhD study.

Finally, I am extremely grateful to my best and most important support from my parent and my son for their love and all-round support.

Table of contents

List of figures

List of tables

1. Introduction

1.1. Surveying and mapping the reinforcement

1.1.1. Quality of construction work - Inspection and building diagnosis

Hong Kong is one of the global financial centres in the world with a high population density. A total of approximately 35,700 residential buildings and approximately 5,300 non-residential buildings out of a total stock of 41,000 private buildings in Hong Kong as of the end of 2019 (LCS, 2020). In 2020, 20,888 residential units were completed and forecast completions of 18,228 and 19,987 residential units in 2021 and 2022 respectively (RVD, 2021). To ensure the quality and integrity of construction materials and provide a safe and reliable structure throughout its entire building life, inspections on the quality of building elements during construction and regular routine structural monitoring of existing buildings are vital. Reinforcement is an essential construction material in reinforced concrete structures which is designed to take up different stresses, especially tensile stress. Reinforcement including quantities, location, orientation and thickness of concrete cover to protect it is designed by the engineer and specified in the drawing and is the most important quality control item in site inspection and building diagnostic to satisfy the requirement in construction works and facilitate non-destructive works for maintenance and addition & alternation works, respectively.

Modern diagnostic techniques by non-destructive testing (NDT) methods provide compliance checks of quality of works and allow detection of defects, both internal and external, inside building materials such as concrete and reinforcement. The major advantage of NDT is testing without destroying the structure. NDT methods, including rebound hammer testing, half-cell potentiometer testing, rebar locator and ultrasonic testing, are best blended. For example, results of rebound hammer test and ultrasonic test on the characteristics of concrete are significantly interfered with by the embedded reinforcement inside especially those in small cover depth. In addition, as-built structural drawings are normally absent, making the actual on-site location of the rebar not fully match the drawings. Covermeter can then be applied to identify the rebar locations, cover depths and orientations prior to performing other non-destructive tests. But there are limitations: (1) it requires the skilful and experienced officer to examine each rebar location; (2) the test is time-consuming because it requires detailed measurement steps, (3) detailed digital data

acquisition and traceable records cannot be provided, therefore the result is somehow subjective and easily affected by surrounding embedded objects such as heavily reinforced stirrups and diagonal trimming bars around openings, and (4) measured results are not correlated to the other important parameters of interest such as moisture content, strength and age of concrete.

1.1.2. Locating of reinforcement inside concrete using Ground Penetrating Radar (GPR)

Ground penetrating radar (GPR), provides an alternative near-surface geophysical (NSG) non-invasive and non-destructive method for underground utility surveying and mapping (Annan, 2004; Daniels, 2004; Jol, 2009; Lai et al., 2018).

In a GPR system, it is composed of a monostatic antenna, a control panel and a display screen. Inside the monostatic antenna, two separate antennas including transmitter (Tx) and receiver (Rx) are housed in a container with the standard configuration of separation distance between Tx and Rx. GPR antenna (Tx) emits electromagnetic wave (EM wave) signals that penetrate through mixtures of construction material or layers of soil and the signal is reflected to the GPR antenna (Rx) once the signal encounters objects with significant dielectric contrasts with the host material. The processing unit digitizes and re-constructs the signal in radargrams.

GPR traverses along the grid map on the surface of the concrete element. The coordinates (x,y,d) of the utilities or reinforcement inside concrete can be obtained. The planar coordinates (x,y) of the GPR antenna are positioned by the grid map and the relative position of the apex of hyperbolic shape reflection can be identified.

For the estimation of the depth of reinforcement from the concrete surface, the propagation velocity of the GPR wave and the travelling time to and from the GPR antenna and the reflected object, i.e. two-way travel time (TWTT), are the key factors concerned. The propagation velocity of the GPR wave in the host material can be evaluated by different algorithms and the two-way travel time (TWTT) of the apex of hyperbolic shape reflection can be obtained via the radargram. With the estimated velocity and TWTT, the depth of the target can be calculated as below,

$$d = V * \frac{t}{2} \tag{1.1-1}$$

where V is the estimated propagation velocity of the GPR wave, t is the half of the time of flight of the GPR wave between the antenna and the target, i.e. two-way travel time, and d is the estimated depth of the target object.

According to ASTM, for the antenna with a common separation distance, a GPR wave ray-path is modelled as shown in Figure 1.1.2-1. When the antenna is located at the position of x_i, the two-way travel time (TWTT), t_i, of the GPR wave ray-path is greater than the TWTT, t_0, for the antenna at the position of x_0, where it is located directly on top of the target object. The reflected signal received appears as a diffractive hyperbola in the radargram. This hyperbola provides important information associated with spatial and lateral distance to measure wave travelling time.

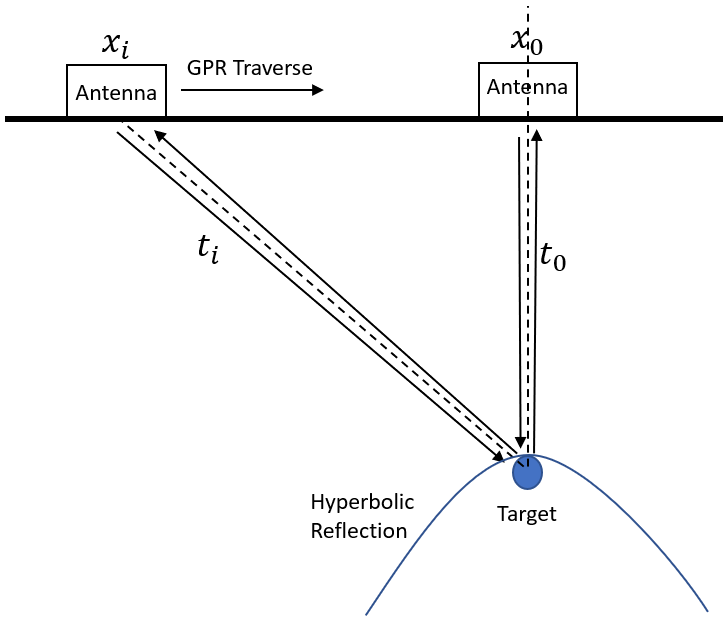

Figure 1.1.2-1 Model of GPR wave travel path (antenna and target as point source)

Nowadays, GPR with different ranges of frequency is applied to identify objects below ground for utility surveys and reinforcement or pipes inside reinforced concrete elements. The specification, limitation and uncertainty of GPR measurement based on validated models are questionable. For uncertainty of measurement, the modelling of the hyperbolic form of reflected wave received, i.e. (x_i, t_i), evaluates the propagation errors as shown in Figure 1.1.2-1.

1.1.3. Requirement of concrete cover depth measurement by different standards and specifications

In the world of underground utilities survey, there are different standards and specifications published by different countries and regions (Anspach, 2002; Australia, 2013; CJJ, 2003; HKIUS, 2012, 2014; ICE, 2014; Malaysia, 2006; PolyU, 2019a, 2019b) . Different factors were specified when conducting the survey including chose of equipment, workflow and data post-processing. Specification for underground utility detection, verification and location, PAS 128, (ICE, 2014) specified the accuracy requirements or uncertainty evaluation of the results when the survey type is by detection as tabulated in Table 1.1-1.

Quality Level (QL)	Sub-QL	Survey Method	Accuracy	
			Horizontal	Vertical
D	D	Review records, Oral recollection	/	/
	D	Records, Cursory Site Inspection Anecdotal Evidence	Indicative Location	/
	D	Search/collect/analyze records	/	/
	QL-D	Desktop utility records search	/	/
C	C	Survey and plot visible above-ground utility features	/	/
	C	Surface Feature Correlation and Interpretation, Site survey	Approximate Location	/
	C	Survey surface appurtenances of utilities	/	/
	QL-C	Site reconnaissance	/	/
B	B	Geophysical Methods	Applicable tolerance defined by the project	/
	B	Survey and Trace	±300mm	±500mm
	B	Geophysical Methods	/	/
	QL-B4	Detection	/	/
	QL-B3		±500mm	/
	QL-B3P			
	QL-B2		±250mm or ±40% of detected depth whichever is greater	±40% of detected depth
	QL-B2P			
	QL-B1		±150mm or ±15% of detected depth whichever is greater	±15% of detected depth
	QL-B1P			
		Surface Detection	/	/
	Reliable	Pipe cable loactor	±150mm or ±15% of detected depth whichever is greater	±15% of detected depth (burial depth samller than 3m)
		Ground penetrating radar	±150mm or ±15% of detected depth whichever is greater	
A	A	Actual exposure and subsequent measurement of subsurface utilities	Applicable horizontal survey and mapping accuracy as defined or expected by the project owner	±15mm
	A	Potholing	±50mm	±50mm
	A	Excavate test holes	±100mm	±100mm
	QL-A	Verification	±50mm	±25mm
		Site Check	±165mm or 0.1*depth whichever is bigger (Covering 90% of representative sample points)	±165mm or 0.1*depth whichever is bigger (Covering 90% of representative sample points)
	(American) ASCE 38-02 Standard Guideline for the Collection and Depiction of Existing Subsurface Utility Data			
	(Australia) AS 5488-2013 Classification of Subsurface Utility Information(SUI)			
	(Malaysia) Standard Guideline for Underground Utility Mapping			
	(Britain) PAS 128-2014 Specification for Underground Utility Detection, Verification and Location			
	(Hong Kong) Guide to Utility Survey by Non-destructive Method(using Pipe/Cable Locator in Hong Kong)			
	(Hong Kong) Specification for Nondestructive testing, surveying, imaging and diagnosis for underground utilities-1.1/1.2			

Table 1.1-1Comparison of accuracy requirements from standards and specification from various countries and regions (F. Xie, 2020)

1.1.4. Survey types

Four different survey types were classified in different levels of detail, i.e. from macro- to microscopic point of view, including survey type D-design utility records search, survey type C-site reconnaissance, survey type B-detection and survey type A-verification. Ground Penetrating Radar (GPR) is one of the methods in electromagnetic locating methods in survey type B by detection. In “B-detection” type of survey, is subdivided into four quality levels of detection works from low accuracy to high accuracy in terms of horizontal and vertical survey measurement, i.e.

QL-B4 to QL-B1. Considering depth measurement, the accuracy of vertical depth measurement specified in QL-B2 is that the actual vertical depth should be within ±40% of the detected depth of the target object. And, for QL-B1, the accuracy of vertical depth measurement is highest which requires the actual vertical depth should be within ±15% of the detected depth of the target object when multiple geophysics techniques are applied. The accuracy requirement set out in PAS is based on empirical estimations by the practitioners and clients' expectations. While, for concrete cover depth measurement, it is neither no code nor standards that mention the specified requirement nowadays. This thesis suggested a solution to the depth estimation algorithm with an evaluation of uncertainty by root mean square errors.

1.1.5. Research questions

Unlike the underground utilities survey, there is not much attention has been drawn to the quality level or accuracy level of estimating the concrete cover depth of the rebar in the code, standards, and specifications by using GPR as a non-destructive testing method.

To sum up, the research studies and the proposed work are summarized below,

1) What is the level of accuracy/uncertainty in using GPR to estimate the cover depth of reinforcement inside the concrete element, including the standard deviation/variance?
2) What is the confidence level to best estimate the cover depth of rebar inside the concrete element within a certain range/quality level? (i.e. certain range/quality level (±Y) = estimated depth ± X × standard deviation, where X is the coverage/quality factor)

1.2. Research objectives

To tackle the above questions, this thesis studied the following objectives,

1. The recognition of potential sources of errors during the estimation of concrete cover depth by using GPR from the host material, geometry of ray-path to the instrumentation & signal processing.

   Recognition of potential sources of errors includes: (a) the host material itself, i.e. dielectric and conductivity properties as it is key factors governing the propagation of electromagnetic waves; (b) geometry of ray-path, indicating the model adopted to describe

the GPR wave travel path; and (c) the equipment & signal processing, i.e. GPR digitization setting and time-zero setting in signal processing.

2. Depth estimation using GPR by semi-trilateration method – model and evaluate the uncertainty

   Depth estimation by ASTM D6432-2019 (circular object and single trilateration method) is based on the assumption that the transmitting and receiving antenna and target object are point-form sources. This assumption incurs errors in the estimation of GPR wave velocity and concrete cover depth measurement since the simplified method omitted (1) the separation of antennas and (2) the radius of the target object. The method was finetuned by considering the separation distance between transmitter and receiver and the oblique angle between the alignment of the target object and the traverse of the antenna.

3. Depth estimation using GPR by full trilateration method – model and evaluate the uncertainty

   Depth estimation by full trilateration considers not only the antenna separation of transmitter and receiver and oblique angle but also the size and depth of the target object. However, the depth of the as-built information may not be obtainable. This method combines both the semi- and full trilateration algorithms to approximate depth. The semi-trilateration algorithm is used to obtain an approximate depth and this value is then input into the full trilateration algorithm.

4. Develop an algorithm for depth estimation using GPR by semi-trilateration method

   Develop and propose a new algorithm with consideration of adjustment in measurement error to accurately estimate the cover depth by using GPR.

5. Depth estimation using GPR by semi-trilateration method with a newly developed algorithm

   Evaluate the uncertainty level of the estimated result by GPR measurement and the relationship with sources of errors including properties of host materials, GPR antenna centre frequency, depth of the target object and GPR digitization setting and time-zero setting in signal processing.

1.3. Organization of this thesis

This chapter, Chapter 1, provides an overview of the importance of non-destructive testing to inspect and evaluate the quality of construction works by GPR, and introduces the application of GPR and the research work to estimate the cover depth accurately. The literature review includes (1) the understanding of EM waves, (2) antenna types and features, such as frequency, resolution, and configuration, (3) the permittivity of materials and their interaction, (4) the hydration process, (5) property of concrete and its structures, (6) models to study different algorithms for depth estimation method by common offset antenna, and (7) uncertainty evaluation.

In Chapter 3, recognition and explanation of all possible sources of errors influencing the estimation of concrete cover depth by GPR including host material, geometry of ray-path, and equipment & signal processing. (Research objective 1)

In Chapter 4, models and evaluates the ray-path models using semi- and full trilateration methods with consideration of antenna separation and size, and depth of the target object respectively. Experiments were conducted and validation of the estimated cover depth was performed. The effect of near-field and far-field problems on accuracies of cover depth measurements is also studied. (Research objective 2 and 3)

In Chapter 5, uncertainty on the estimation of the concrete cover depth of rebar will be evaluated after the consideration of ray-path trajectory errors including the effect of the ages of concrete and the moisture content of the concrete.

In Chapter 6, an accurate algorithm to estimate the cover depth based on the semi-trilateration method and statistical root mean square errors will be developed. This new algorithm will be validated via the experiment on concrete walls with true cover depth. Besides, the new accurate depth estimation algorithm will incorporate confidence level and confidence interval by considering the identified errors in Chapter 3 as observational errors and scattering errors and propagating them into the new algorithm based on the semi-trilateration method.

In Chapter 7, the findings, contribution to knowledge, recommendations and limitations of this research are concluded.

2. Literature review

2.1. Electromagnetics and dielectric material

2.1.1. Electromagnetics and Maxwell's equations

Maxwell's Equations are the most influential equations in science and the fundamental importance in describing the classical electromagnetic phenomena that underpin modern information and communication technologies. A set of four equations of Maxwell's Equations describe the properties and interrelations of electric and magnetic fields and are expressed as below, i.e. Equation 2.1.1-1 to 2.1.1-4.

$$\nabla \cdot D = \rho \tag{2.1.1-1}$$

$$\nabla \cdot \mathrm{B} = 0 \tag{2.1.1-2}$$

$$\nabla \times \mathrm{E} = -\frac{\partial B}{\partial t} \tag{2.1.1-3}$$

$$\nabla \times \mathrm{H} = J + \frac{\partial D}{\partial t} \tag{2.1.1-4}$$

where, ∇ = gradient operator,

$\nabla \cdot$ = divergence operator,

$\nabla \times$ = curl operator,

D (C/m^2) = electric flux density,

B (Tesla) = magnetic flux density,

E (V/m) = electric field intensity,

H (A/m) = magnetic field intensity,

ρ = electric charge density, and

J (A/m^2) = current density.

For Equation 2.1.1-1, Gauss's law for electric fields (differential form) reveals the electric field produced by electric charge diverges from positive charge and converges upon negative charge. For Equation 2.1.1-2, Gauss's law for magnetic fields in differential form explains the divergence of the magnetic field at any point is zero. Faraday's law (differential form) of Equation 2.1.1-3

indicates a circulating electric field is produced by a magnetic field that varies with time. Finally, the Ampere-Maxwell law of Equation 2.1.1-4 discusses a circulating magnetic field produced by an electric current and by an electric field that varies with time (Fleisch, 2008).

2.1.2. Constitutive parameters of material

Maxwell's equations are applicable to both free charges and currents, and bound charges and currents with the help of constitutive equations. For isotropic and homogeneous materials, the relevant equations are expressed in Equations 2.1.2-1, 2.1.2-2 and 2.1.2-3, which involved three constitutive parameters including electrical conductivity, dielectric permittivity and magnetic permeability (Balanis, 2012; Knoll, 1996 and Lai, 2006).

$$J = \sigma E \quad (2.1.2\text{-}1)$$

$$D = \varepsilon E \quad (2.1.2\text{-}2)$$

$$B = \mu H \quad (2.1.2\text{-}3)$$

where, J = current density,

σ = electrical conductivity (S/m),

E = electric field intensity,

D = electric flux density,

ε = the dielectric permittivity (F/m),

B = magnetic flux density,

μ = the magnetic permeability (H/m), and

H = magnetic field density,

Electrical Conductivity

Conductivity represents the electrical property of the material, and it indicates the ability of the material to conduct electric current. Hence, it is the reciprocal of electrical resistivity. According to Equation 2.1.2-1, the current density (J) is directly proportional to the electric field intensity (E) when an external electric field is applied to the material. For material with higher conductivity, its

electrons at the outermost shell can be easily detached from the nucleus. These electrons can more freely inside the material and electric current can be formed once an external field is applied.

Dielectric permittivity

Dielectric materials are materials that its electrons cannot move freely and are bound around the nucleus (Landau et al, 2013). These electrons can only be slightly deflected from the nucleus to form an internal electric field when an external electric field is applied. The orientation of the internal electric field is against the external electric field which forms an equilibrium inside the material's atoms (William, 2007). This phenomenon is called 'polarization'. The density of electric flux during polarization is expressed in Equation 2.1.2-2. In electromagnetism, the permittivity is formed by a real part (ε') and an imaginary part (ε"). The real part of the complex permittivity dictates the propagation velocity of the electromagnetic wave and the imaginary part of the complex permittivity governs the absorption of the electromagnetic wave in the materials. The real part of the complex permittivity can be expressed in Equation 2.1.2-4 as the relative permittivity.

$$\varepsilon_r = \frac{\varepsilon'}{\varepsilon_0} \tag{2.1.2-4}$$

where, ε_r = relative permittivity and becomes a unitless quantity,

ε' = real part of the complex permittivity, and

ε_o = the permittivity of vacuum, 8.854 x 10^{-6} F/m

Magnetic permeability

The permeability of a material relates to the degree of magnetization after applying a magnetic field (Fetzlaff, 2007; Jiles, 2015) and is expressed in Equation 2.1.2-3. Similar to relative permittivity, relative permeability is commonly used and can be expressed as Equation 2.1.2-5.

$$\mu_r = \frac{\mu}{\mu_0} \tag{2.1.2-5}$$

where, μ_r = relative permeability of the material,

μ = the magnetic permeability of the material, and

μ_o = the magnetic permeability of free space, 1.26 x 10^{-6} H/m

2.1.3. Hydration process after mixing water and cement

In the production of concrete, the major components including cement, fine aggregates, coarse aggregates and water are mixed and a chemical reaction, i.e. hydration, takes place. In the hydration process, water reacts with an anhydrous compound and produces a new chemical product. Non-hydrated cement reacts with water and conducts both chemical and physicomechanical changes with setting and hardening (Hewlett & Liska, 2019). The wet concrete gradually increases in viscosity and hardens in the first 28 days after mixing. The strength of the concrete continues to develop for a year after mixing. Hydration of Portland Cement (PC) consists of different clinker materials including alite (tricalcium silicate, C_3S), belite (dicalcium silicate, C_2S), tricalcium aluminate (C_3A), calcium aluminate ferrite (C_4AF), free calcium oxide and alkali sulphates, and calcium sulphate with water simultaneously at its own rates. The hydration process can be classified into different stages including Pre-Induction Stage, Induction Stage, Acceleration Stage and Post-Acceleration stage. In the Pre-Induction stage (at the initial), when cement contact with water, ionic species dissolve into the liquid phase and the hydrate phase starts. K+, Na+, Ca^{2+}, and silicate ions form from dissolved alkali sulphates, calcium sulphate and tricalcium silicate. A layer of precipitates formed at the surface, i.e. calcium-silicate-hydrate (C-S-H). In the Induction stage, the overall hydrate rate declines significantly for a few hours as the concentration of calcium hydroxide (CH) reaches maximum. concentration remains constant as the amount consumed due to the formation of ettringite (Aft) is balanced by the amount dissolved from gypsum. In the Acceleration Stage, nucleation and growth of C-S-H (also called 'second-stage CSH') and CH exists. C_2S starts hydrating substantially. Liquid phase Ca^{2+} and concentration decline as $Ca(OH)_2$ starts precipitating and increasing Aft formation and adsorption of on C-S-H respectively. Lastly, in the Post-Acceleration Stage, the hydrate rate slows down due to a combination of different factors (1) the unconsumed Portland cement materials get less, (2) the diffusion process dominates, and (3) C_2S concentration increases which causes the decline of formation rate of CH. During hydration, several factors decide the kinetics including (1) quantity and form of calcium sulphate, (2) fineness of cement particles, (3) water/cement ratio, (4) curing conditions, (5) temperature, and (6) chemical admixtures. The nanostructure and microstructure of the formed hydrated materials are governed by the composition of the binder, water/cement ratio, temperature of hydration, chemical admixture and the time of hydration (Hewlett & Liska, 2019).

In the hydration process, as the water/cement (W/C) ratio is one of the dominant factors in forming cement pasts and mortars, the changes in the W/C ratio will affect strength, porosity, permeability and durability. The increase in the W/C ratio will increase the porosity of hardened concrete and also lead to much free water not hydrated with cement resulting in decreasing the permeability and strength of concrete. It then affected the durability of the concrete. In cement paste microstructure studies for hardened Portland cement pastes with different W/C ratios, the visualized result shown in the electron imaging revealed that the amount of pore and crystalized structures increased. Portland cement paste made with W/C of 0.3 develops a compact structure matrix with little or no apparent crystallinity. While Portland cement paste formed with W/C of 1 develops a structure with observable pores and is less dense (Hewlett & Liska, 2019). In addition to the W/C ratio, there are two other factors that determine the pore system including aggregate to cement ratio and degree of hydration (Neville, 1995).

2.1.4. Pores Structure of hardened concrete

Hardened concrete is a porous material. The volume of pores varies with the W/C ratio initially and the formation of chemical products during the hydration process. In fully saturated Portland cement pastes, pores are filled with “free” water, i.e. volume of pores is equal to the volume of “free” water. During the hydration process, a fraction of “free” water becomes “bound” water under a chemical reaction. The content of “bound” water in hardened Portland cement paste is related to the content of cement in different phases and the degree of hydration. A study of the porosity by different methods on 2 years age mature Portland cement pastes made with different W/C ratios is shown in Table 2.1.4-1. The result showed that the porosity increases for Portland cement pastes made with W/C = 0.30 to 1.00. The study measured the amount of “free” water removed from Portland cement pastes by drying method and extraction of “free” water with acetone and ethyl occupied the pores (Hewlett & Liska, 2019).

W/C	“Free” water removed by Drying method	“Free” water extracted by acetone and ethyl method
0.30	0.142	0.098
0.50	0.299	0.204
0.70	0.417	0.350
1.00	0.555	0.473

Table 2.1.4-1 The porosity of Portland Cement pastes hydrated for 2 years at 20oC by different methods (Hewlett & Liska, 2019)

The pore system can be classified as (1) macro-pores with hydraulic radii between <1 and 1000nm, (2) pores with smaller radii called gel pores which combined with hydrated product, and (3) pores with greater radii called capillary pores which increases with increase of water/cement ratio. Figure 2.1.4-1 shows the pore distribution of hydrated concrete, mortar and paste at 0.45 W/C ratio.

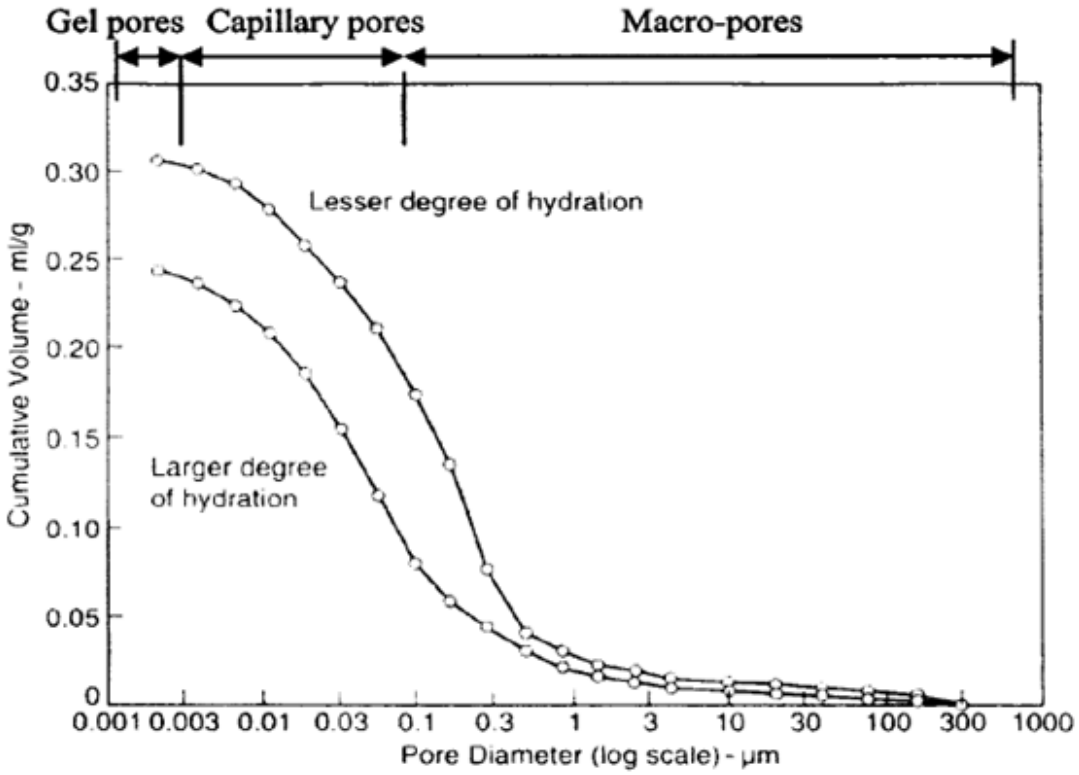

Figure 2.1.4-1 The pore distribution of More Hydrated Concrete, Mortar and Paste at a W/C ratio of 0.45 (Nevill, 1995)

Macro-pores - It is formed by air bubbles trapped inside concrete due to inadequate compaction of concrete and/or excessive free water during hydration. Macro-pores such as honeycomb and segregation can be found on concrete surfaces.

Capillary pores – These are formed due to voids inside concrete that are not fully occupied by hydrated products. Its size and shape vary and they are inter-connected to form a water transport system randomly.

Gel pores – These are the pores within the structure of the hydrated product. They are interconnected with interstitial spaces between the needle-plate and foil-shaped gel particles (Neville, 1995)

2.1.5. Models of structure of hydrated product and C-S-H Nanostructure

Several models to study the structure of hydrated products have been developed by different researchers to enhance the overall understanding of essential phenomena including concepts related to strength development and durability. One of the best models to study the structure of C-S-H is described by the Feldman-Sereda (F-S) model. The model interpretated that the structure consists of randomly oriented C-S-H layers with water absorbed on the surface of the C-S-H layers, water occupied between the interlayers of C-S-H layers and water in the form of capillary water as shown in Figure 2.1.5-1 The symbol "O" shows water absorbed on the surface of the C-S-H layers and the symbol "X" shows the interlayer hydrate water and cavity forms for capillary water. The model implied a very large surface area for the gel and was proved by different experiments such as water sorption and N_2 sorption measurements (Hewlett & Liska, 2019).

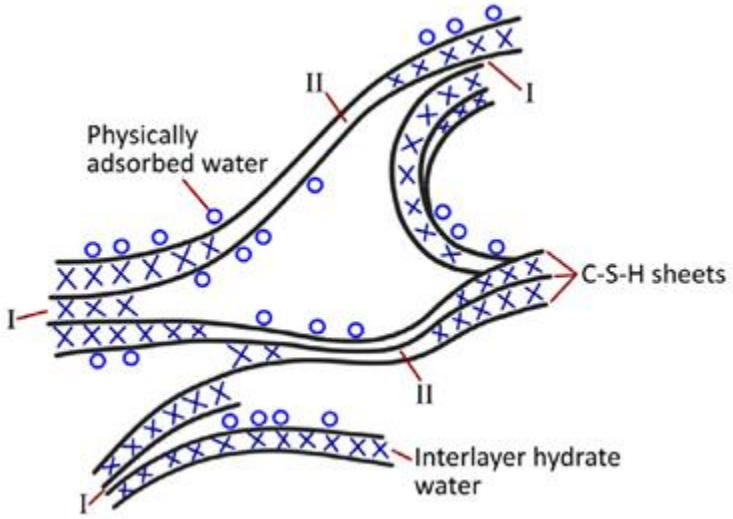

Figure 2.1.5-1 Schematic of the structure of C-S-H gel according to Feldman and Sereda (P.C. Hewlett and M. Liska, (2019))

2.1.6. Dielectric properties of concrete during hydration

The characteristics of electromagnetic (EM) absorption and reflection of materials are governed by (1) electromagnetic permittivity(e), (2) permeability (m), and (3) conductivity(s). Construction materials such as concrete are having its dielectric properties due to their non-metallic nature and good electrical insulation to direct current (Dinh et al., 2021). As concrete is a non-magnetic material, the permeability of concrete is assumed to be equal to the permeability in free space, i.e. $m_0 = 4\pi.10\text{-}7$ H/m, (Laurens et al., 2005 & Cassidy, 2008). Concrete is a cement-based matrix with different free water content trapped in the pores as mentioned above. The study of the dielectric properties of concrete can help to better understand the microstructure of concrete as concrete is highly dependent on water content which greatly affects the dielectric permittivity and conductivity of concrete (Dinh et al., 2021). Concrete is a heterogeneous material and is composed of different states from solid aggregates to air pores and water-filled gel pores during hydration and hardening afterwards. As mentioned in sections 6.2 and 6.3, the free water chemically reacts with cement and is physically bound, and gel pore and pores structures formed during hydration. Hence, the relative permittivity of concrete is determined by the distribution of different states and water content inside concrete. As dielectric permittivity is frequency dependent, bound water and free water respond at low frequencies, i.e. 10 Hz – 1MHz, and high frequencies, i.e. more than 1 GHz, respectively. Thus, the level of frequency response helps to determine the microstructure inside the hardened concrete and water content (Dinh et al., 2021).

2.1.6.1 Permittivity

The enclosed volume of material can be measured by dielectric permittivity, ε, which is expressed as a complex value relative to the permittivity of free space ε_0:

$$\mathcal{E} = \mathcal{E}_0\mathcal{E}_r = \mathcal{E}_0(\mathcal{E}_r' - j\mathcal{E}_r^{"}) \qquad (2.1.6.1\text{-}1)$$

where, $\varepsilon_0 \approx$ 8.854 × 10-12 F/m, and

j = imaginary unit (with $j^2 = -1$).

Combining it with the Maxwell-Amphère Law and the electric conductivity:

$$\nabla \times H = j\omega\varepsilon'\left(1 - j\frac{\sigma + \omega\varepsilon^{"}}{\omega\varepsilon'}\right)E \qquad (2.1.6.1\text{-}2)$$

where, H = magnetic field,

E = electric field, and

ω = angular frequency.

The real part, $\mathcal{E}_r^{'}$, relates to EM wave phase shift, delay, and dispersion when travelling through a medium. The imaginary part $\mathcal{E}_r^{''}$ relates to EM wave losses during travelling in the medium. Losses are measured by the loss tangent:

$$E\ tan\delta\ = \frac{\mathcal{E}_r^{''}}{\mathcal{E}_r^{'}} \qquad (2.1.6.1\text{-}3)$$

Permittivity is frequency dependence and can be described as different types of the polarizability of material under EM field: (1) interface polarization (or called Maxwell-Wagner effect) – surface dipoles respond to EM field, (2) dipolar polarization – it applies to all materials which dipoles of the material try to align with EM field and causing a net dipole moment, (3) ionic polarization – it applies to crystallized material which dislocation of ions occur under EM field, and (4) electronic polarization – the movement of an atom's nucleus with respect to the centre of charge formed and cloud of electron responds to EM field (Dinh et al., 2021).

2.1.6.2 Dielectric dispersion in Debye relaxation model of materials' particles

Dipolar polarization can be explained by the Debye relaxation equation, and Cole and Cole's model as below,

$$\varepsilon_r(f) = \varepsilon_{r,\infty} + \frac{\varepsilon_{r,0} - \varepsilon_{r,\infty}}{1 + j\omega\tau} \qquad (2.1.6.2\text{-}1)$$

where, f = frequency,

ω = angular frequency, 2πf

$\varepsilon_{r,\infty}$ = complex relative permittivity nearing infinity

$\varepsilon_{r,0}$ = complex relative permittivity at f = 0

τ = relaxation time

In a normal environment, the net volume density is equal to zero under an equilibrium situation even the orientation of action of dipolar molecules changes randomly due to the thermal effect with neighbouring molecules. When the EM field occurs, each dipole moment experiences torque as the dipole tries to orientate parallel to the field direction. The dipole moment relaxes and is realigned randomly in order to achieve equilibrium status once the EM field is removed. The period of this relaxation time is described below and the relaxation behaviour happens at a specific frequency,

$$\tau = \frac{1}{2\pi f_{relaxation}} \quad (2.1.6.2\text{-}2)$$

When the EM wave frequency is less than the relaxation frequency, the dipolar orientation of materials' particles follows the varying applied EM field. The real component of complex permittivity is determined by the amount of energy stored since the rate of change of orientation of all molecules follows the rate of change of the EM field which yields bulk polarization. When EM wave frequency reaches the relaxation frequency, the materials' particles keep in motion but are no longer able to follow the rate of change of the EM field. The rate of change of movement of materials' particles induced by the EM field is too fast and difficult for the particles to follow, and incapable of achieving bulk polarization so the imaginary part of the complex permittivity reaches the peaks. As such, a significant amount of energy is converted to heat, and it is also the principle of microwave heating applications. This phenomenon is called dielectric dispersion. When EM wave frequency is beyond the relaxation frequency, polarization effects tend to be minimal as the dipolar orientations of materials' particles are unable to follow the applied EM field due to the inertia of the molecules or the viscosity of the medium (Dinh et al., 2021). This phenomenon can be explained as an imaginary part of ε_r in Figure 2.1.6.2-1.

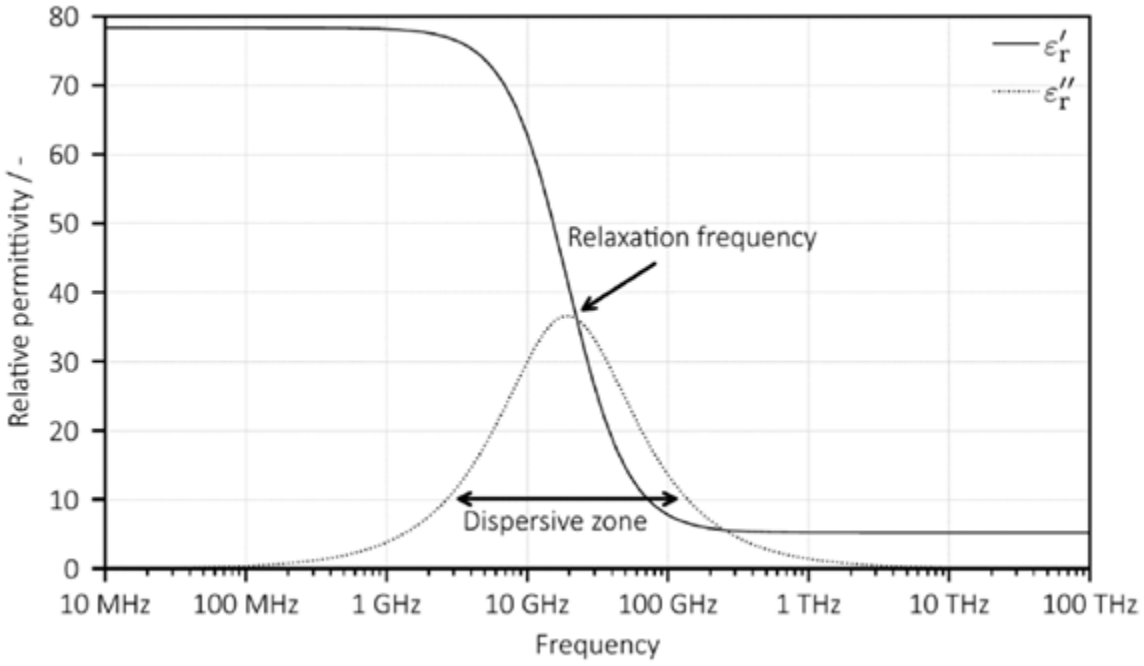

Figure 2.1.6.2-1 The permittivity of pure water (Dinh et al., 2021)

Debye's model, and Cole and Cole's model simulated polarization mechanism for pure material and composite material with different regions of dielectric dispersion and spectrum of relaxation time respectively. Comparing the range of time of relaxation between free water and composite materials containing water under microwave region, i.e. 17.1GHz at 25^{o}C. The permittivity loss is prominent at above 500MHz as free water is contained in composite materials. For EM wave frequency ranging between 10 to 3000MHz, most materials follow the real component of complex permittivity since exhibiting permittivity relaxation and the imaginary component takes place under the same frequency. The imaginary component reaches maximum frequency (t_f) and gradually drops. At relaxation time (t), the absorption mechanism is prominent (Lai and Wiggenhauser, 2010).

2.1.6.3 Permittivity of free and bound water in material

Pure water, H_2O, is a homogeneous polar material with permanent electric dipole moments. Water molecules exhibit dipolar orientation polarization. When the EM field is applied, polar molecules of water rotate and align to the direction of the field. Its permanent dipole moments are much greater than the induced dipole moment by an externally applied EM field. Thus, the dielectric constant and polarizability of water are higher than solid materials. Similarly, as shown in Figure 2.1.6.2-1, the magnitude of relative permittivity of free water in the real part is larger than the solid materials. This implies that dipolar polarization and relaxation behaviour is performed for particles that are free to rotate, i.e. free water, instead of being restricted in motion, i.e. bound water. Comparatively, the change of permittivity for dry solid material and air is relatively smaller than that with the presence of moisture under the same frequency (Dinh et al., 2021).

2.1.6.4 Permittivity of concrete during hydration

The permittivity of hardened concrete varies from 4 to 20 as it is composed of a different phase of materials including a solid phase of aggregates, non-reacted cement residues, hydrated product, and etc., a gaseous phase of air, and liquid phase of water, i.e. free water and physically bounded water. Table 2.1.6.4-1 shows the relative conductivity and permittivity of different construction materials.

Material	Conductivity, σ (mS/m)	Relative permittivity, ε_r
Vacuum	0	1
Air	$3 \times 10^{-12} - 8 \times 10^{-12}$	1.000536
Concrete – dry	1–10	4–10
Concrete – wet	10–100	10–20
Limestone – dry	$10^{-7} - -10^{-3}$	4–8
Limestone – wet	10–100	6–15
Sandstone – dry	$10^{-7} - -10^{-3}$	4–7
Sandstone – wet	10^{-3}–0.01	5–15
Sand – dry	10^{-4}–1	3–6
Sand – wet	0.1–10	10–30
Water	0.1–10	78 (25 °C)–88
Water (ice)	10^{-6}–1	3
Seawater	4000	81–88
Seawater (ice)	10–100	4–8

Table 2.1.6.4-1 Typical values of relative permittivity (real component) and conductivity at a frequency of 100MHz (Dinh et al., 2021)

The permittivity of material can be found by measuring the EM wave travelling time to and from the antenna and target object such as rebar, i.e. Two-Way Travel Time (TWTT), and calculated by the following equation,

$$v = \frac{D}{T/_2} = \frac{c}{\sqrt{\varepsilon'}} \qquad (2.1.6.4\text{-}1)$$

where, v = EM wave travelling speed in the medium,

D = cover depth of target object,

T = Two-Way Travel Time (TWTT),

C = Speed of light in air, and

ε' = real part of dielectric permittivity.

2.1.7. Characterization of dielectric dispersion through GPR measurement and Short-Time Fourier Transform (STFT) and Wavelet Transform (WT)

Short-Time Fourier Transform (STFT) - The signal of an EM wave composed of sinusoidal functions over an entire signal in the time domain. The classical Fourier transform can evaluate

the frequency response and distribution of the stationery signal over the entire signal in a plot. To study the frequency response in a particular period for a non-stationery signal, the algorithms of short-time Fourier transform (STFT) in Joint time-frequency analysis (JTFA) provide a detailed Fourier transform which transforms the one-dimensional signal into a two-dimensional time-frequency plot and concentrated in time and frequency as a function. The algorithm of STFT is expressed as below,

$$STFT[x(t)] \equiv X(\tau, \omega) = \int_{-\infty}^{\infty} x(t)\omega(t-\tau)e^{-j\omega t}dt \qquad (2.1.7\text{-}1)$$

where, $\omega(t)$ = window function (e.g. Hanning window) for a specified period; and

$x(t)$ = time domain for a specified period.

The window length controls the resolution of time and frequency of the STFT. A narrow window results in a fine time resolution and consequently a poor resolution of frequency since a signal with a short period of time in a narrow window which causes a wide bandwidth, i.e. low frequency/spectral leakage occurs. While a wide window results in a fine frequency and a poor resolution of time since wide windows have a long period of time which causes a narrow frequency bandwidth, i.e. blurred target of interest. This window effect is essential, and the size of the window length depends on the characteristics and area of interest of the signal (Lai and Wiggenhauser, 2010).

Wavelet Transform - GPR received wavelet signals composed of low-frequency and high-frequency signals. To study the low-frequency and high-frequency components obtained due to direct wave and the dielectric contrast between the reflected signal from the target object and the host material with a co-relationship between amplitude and time spectrum respectively, wavelet transform is applied. WT is a multi-resolution analysis (MRA) method. It decomposes and analyzes signals of interest into multi-levels of frequency resolution with respect to time and frequency domain, and analysis non-stationary and dispersed signals by the mothed of dilation via stretches of time length. The algorithm of WT is expressed below in integral continuous form (Lai et al., 2014; Baili et al., 2009 and Lu et al., 2020).

$$WT_{u,a} =< s, \psi_{u,a} > = \int_{-\infty}^{\infty} s(t)\, \psi^{*}_{u,a}(t) dt \qquad (2.1.7\text{-}2)$$

where, s(t) is called father wavelet/scaling function, and

$\psi_{u,a} = \frac{1}{a}\psi\left(\frac{t-u}{a}\right)$ is called mother wavelet,

And, a = scale factor, $2^{\frac{1}{v}}$, where v = 1,2,3,… for Continuous Wavelet Transform (CWT),

A = scale factor, 2^{j}, where j = 1,2,3, ... for Discrete Wavelet Transform (DWT),

u = shift factor

$\psi^{*}_{u,a}$, = complex value is adopted (Morlet wavelet or Gabor wavelet) .

In WT, a wavelet is formed by two functions called father wavelet and mother wavelet. The father wavelet and mother wavelet represent smooth and low-frequency components of the reflected signal, i.e. low pass filter (LPF), and detail and high-frequency components of the reflected signal, i.e. high pass filter (HPF), respectively. Through the dilating process of mother wavelet, the breakdown process and further produces another low and high-frequency component which forms a sub-branch of the father wavelet and mother wavelet, and the processes continues to the interest of frequencies. With the function of dilation and shifting of the wavelet along the time axis in the A-scan, WT analyzes transient signal with good time resolution at high frequency but relatively poor frequency resolution and good frequency resolution at low frequency but relatively poor time resolution. Compared to STFT and WT, STFT analyzes frequency components of the signals in a fixed duration of time intervals while WT analyzes the whole signals without limitation of time window interval in a short time (Lai et al., 2014; Baili et al., 2009 and Lu et al., 2020).

2.2. Theory of GPR

Maxwell's equation described classical electromagnetism and indicated the interrelationship between time-varying electric and magnetic fields. Based on this concept, radar systems were developed to obtain object information by using the travel path of the electromagnetic wave generated by the radar system (Skolnik, 1980) and radars are widely used for the study of geology, hydrology, mineralogy, archaeology and civil engineering (Benedetto & Pajewski, 2015; Bristow & Jol, 2003; Conyers, 2013; Moorman & Michel, 2000; Schultz, 2012).

2.2.1 Antenna Design

2.2.1.1 Continuous wave and impulse antenna

In general, there are two types of GPR antenna design including continuous wave (frequency domain) and impulse (time domain) (Travassos et al., 2018). A continuous-wave GPR antenna emits electromagnetic waves continuously with infinite time duration and simultaneously receives the emitted wave. This type of GPR antenna detects objects but is limited to measuring distance due to constant signals. As such, its configuration is enhanced by modulation such as frequency modulated continuous wave (FMCW) (Deng & Liu, 1999), stepped frequency continuous wave (SFCW) (Kong & By, 1995 and Wong et al., 2016), and frequency modulated interrupted continuous wave (FMICW) (Fioranelli, 2013). While the impulse GPR antenna excites a very short time duration pulse which requires a rapid switching of the trigger system and a much higher sampling frequency for the analogue-to-digital converter.

2.2.1.2 Geometry of antenna

In terms of the geometry of antenna, it can be classified as dipole antennas, horn antennas, bowtie antennas, as shown in Figure 2.2.1.2-1, etc. (Balanis, 2011; Silver, 1984; Stutzman & Thiele, 2012).

Figure 2.2.1.2-1 Bowtie antenna (GSSI Palm 2Hz GPR)

Antenna polarization, directivity and the emission pattern produced can be varied by antenna design which characterizes the antenna performance to meet the application need. For example, it

is good to use a dipole antenna for boundary layer detection (Höfinghoff & Overmeyer, 2013), horn antenna fits the purpose for application in forest litter and forensic surveys (Almeida et al., 2015; André et al., 2014), and bowtie antenna is good to apply for detection of landmines (Giannakis et al., 2015). The typical radiation pattern of the horizontal geometry dipole antenna is shown in Figure 2.2.1.2-2. The radical axis represents the relative strength of the emitted signal. This thesis uses the common and commercially available dipole antenna, i.e. GSSI 2GHz, as shown in Figure 2.2.1.2-1

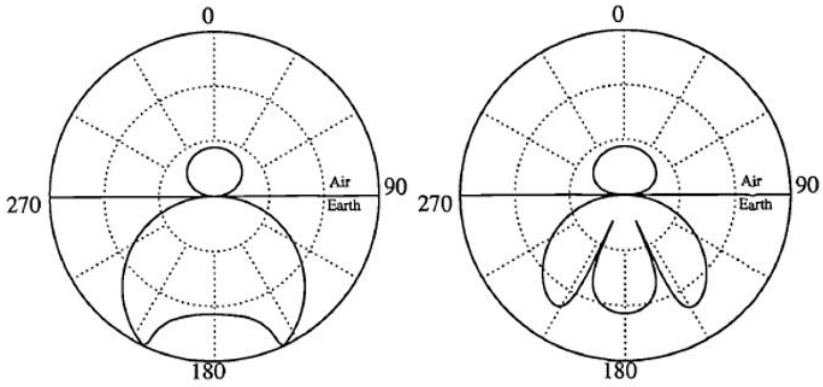

Figure 2.2.1.2-2 A typical radiation pattern in both H (left) and E (right) planes of a horizontal geometry dipole antenna

2.2.1.3 Monostatic and bistatic antenna

A GPR dipole antenna can be categorized into monostatic and bistatic antennae which the setting of the transmitter and the receiver are housed together or separated respectively. In the GPR survey, the setting of transmitter and receiver perform different modes of survey to meet the survey purposes, including common offset (Sham & Lai, 2016; Xie et al., 2018, common mid-point (CMP) (Jacob & Urban, 2016; Steelman & Endres, 2012) and wide-angle reflection and refraction (WARR) (Galagedara et al., 2005; Klysz et al., 2004). For a common offset survey, the transmitter and receiver are collocated with a constant separation between each other during the survey to collect survey data (Lambot et al., 2004; Lambot et al., 2004). For the CMP survey, the setting of the antenna and receiver are closely located with a separation equal to zero initially and they will be moved away from each other in opposite directions with equal distances to the common mid-point during the survey. While, for the WARR, the transmitter is set at a fixed position and the

receiver will move away from the transmitter during the survey to acquire data. Different modes of survey are illustrated in Figure 2.2.1.3-1 and these modes of antenna setting determine the diverse geometries of GPR signal travel paths and, as a result, various reflection patterns obtained in the radargram for an identical target. Specific algorithms are required for computation and data analysis.

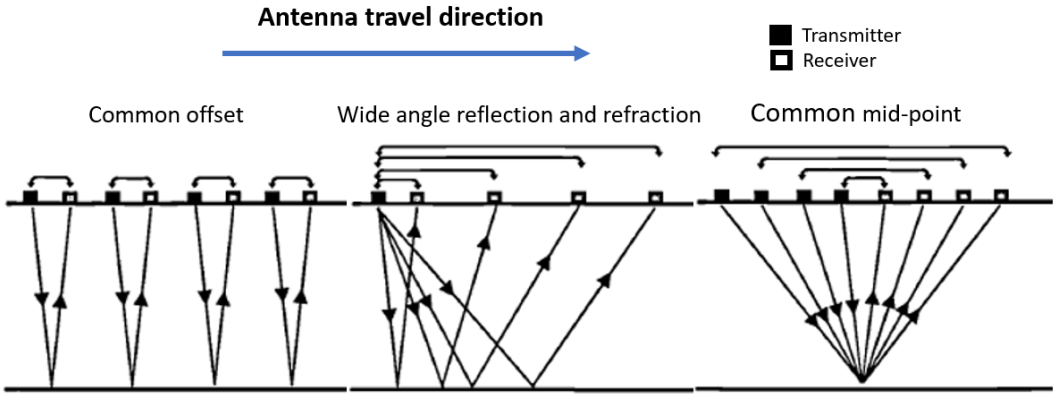

Figure 2.2.1.3-1 GPR wave travel paths of various modes of antenna setting for GPR survey (Giannopoulos, 1998)

In this thesis, all GPR survey was performed by using dipole in common offset mode and radargram data was analysed by corresponding algorithms as discussed in Section 2.4. Within the near field, the GPR wave is propagated mainly by induction. In the far field, the propagation of the GPR wave can be approximated by the ray path method. This thesis focuses on the study of objects buried in the near and far field.

2.2.2 EM (GPR) wave in dielectric material

Maxwell's equation explains the propagation of electromagnetic waves in free space and dielectric materials through oscillating the electric and magnetic field (Hippel & Morgan, 1955) as shown in Figure 2.2.2-1.

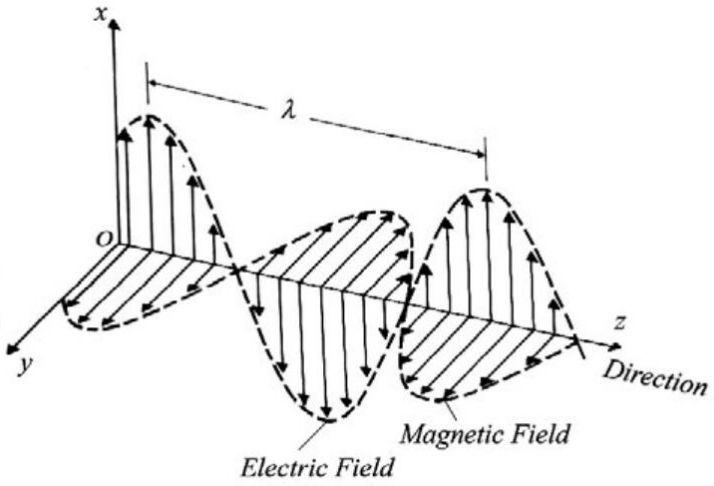

Figure 2.2.2-1 Propagation of oscillating electromagnetic waves (Lindbäck, 2015)

Electromagnetic waves generated by radiation sources spread into the surrounding space spherically. A reasonable assumption made is that the generated electromagnetic wave can be considered as a plane wave at a distance where the source is far away (Giannopoulos, 1998). This assumption formed the basis of the following explanation and one-dimensional wave propagation is assumed.

2.2.2.1 Wave propagation in lossless material

For free space and perfect dielectric materials, the electric conductivity is equal to zero, i.e. $\sigma = 0$, which are known as lossless materials. The propagation of electromagnetic waves can be expressed by Equation 2.2.2.1-1,

$$\frac{\partial^2 E}{\partial z^2} = \mu\varepsilon\frac{\partial^2 E}{\delta t^2} \qquad (2.2.2.1\text{-}1)$$

where, z-axis = the propagation of the wave in z direction,

t = propagation time

μ = the magnetic permeability

ε = the dielectric permittivity

Refer to Equation 2.2.2.1-1, the propagation velocity can be written as Equation 2.2.2.1-2,

$$v = \sqrt{\frac{\partial^2 z}{\partial t^2}} = \frac{1}{\sqrt{\mu\varepsilon}} \quad (2.2.2.1\text{-}2)$$

For free space, the electromagnetic wave propagation velocity, i.e. *c*, can be calculated by Equation 2.2.2.1-3,

$$c = \frac{1}{\sqrt{\mu_0 \varepsilon_0}} \approx 0.2998 m/ns \quad (2.2.2.1\text{-}3)$$

where, ε_0 = the dielectric permittivity in free space, and

μ_0 = magnetic permeability in free space

The electromagnetic wave propagation velocity after combining the permittivity and permeability in Equation 2.2.2.1-2 and relative permeability mentioned in Section 2.1.2 can be re-wrote as Equation 2.2.2.1-4,

$$v = \frac{c}{\sqrt{\mu_r \varepsilon_r}} \quad (2.2.2.1\text{-}4)$$

where, *v* = electromagnetic wave propagation velocity in any dielectric medium such as concrete,

c = electromagnetic wave propagation velocity in vacuum,

ε_r = relative dielectric permittivity of the material, and

μ_r = relative magnetic permeability of the material

The values of magnetic permeabilities (μ_r) can be assumed to be equal to unity as it is insignificant and approximately equivalent to that of free space, except for those materials with large portions of ions (Daniels, 2004; Strangway, 1967). Equation 2.2.2.1-4 can be simplified as Equation 2.2.2.1-5,

$$v = \frac{c}{\sqrt{\varepsilon_r}} \quad (2.2.2.1\text{-}5)$$

2.2.3 GPR Survey

2.2.3.1 Near-field and far-field

A GPR wave is generated by an antenna with a specified wavelength, λ. That antenna can be considered as a single point source at the centre of a spherical volume and the radius, r, of the spherical volume is λ. For a spherical volume with the region of $r < \lambda$, this region close to the source point is called the "Near-field" region. For a spherical volume with the region of $r > 2\lambda$, this region far away from the source point is called the "Far-field" or "Fraunhofer" region. While, for a spherical volume with the region of $\lambda < r < 2\lambda$, it is called a "transition field" (Balanis, 2005).

In the near-field region, GPR transfers energy via the source point, i.e. antenna, to the substrate surface by quasi-stationery field, induction field and radiated field, and energy is exchanged in the near field. Target coupled energy from the source fields and the signal will be coupled in the far-field region (Jol M., 2009). In other words, GPR wave propagation switches from electromagnetic induction to ray-path mode in near-field and far-field respectively. While, in the transition field, both induction and ray-path modes exist (Ludwig, 1971).

2.2.3.2 Transmission of GPR wave into host material

In a GPR survey, the GPR system transmits a pulse to the antenna and the transmitter inside the GPR antenna emits an electromagnetic signal into the host material. The signal is reflected when it encounters an object with a significant difference in dielectric relative to the host material and the reflected signal is received by the receiver inside the antenna. The signal travel time is recorded by the GPR system, and the signal travel velocity is correctly estimated by Equation 2.1.6.4-1. Hence, the depth of the target inside the host material can be estimated by Equation 2.2.3.2-1

$$D = v \times \frac{T}{2} \qquad (2.2.3.2\text{-}1)$$

where, v = EM wave travelling speed in the host material,

D = cover depth of target object,

T = Two-Way Travel Time (TWTT),

2.2.3.2.1 Conical form spread of transmission

Electromagnetic waves emitted by the GPR antenna into the host material in a conical form and spread out increase with increase in depth. The depth and width of the cone are set out by the condition of the host material and by the frequency of the antenna. The higher frequency of the

GPR wave emitted by the antenna results in a narrower conical form of transmission (Dojack, 2012).

2.2.3.2.2 Reflection and refraction of GPR Wave

The GPR wave transmits into the host material if the GPR wave encounters non-metallic material. Its propagation direction also changes due to the change in transmission medium, i.e. refracted wave, as explained by Snell's law. Some of the GPR waves transmitted by the antenna will be reflected to the antenna when the GPR wave comes across a significant difference in dielectric permittivity between the object and the host material. The amount of reflected energy is determined by the contract in relative dielectric permittivity.

2.2.3.2.3 Transmission loss

In the generation of GPR waves, coupling effects will be processed, i.e. GPR antenna is excited by an electrical pulse, between ground-coupled antenna. The coupling effect will take place before the GPR wave propagates into the host material and results in loss of transmission energy.

2.2.3.2.4 Energy attenuation

GPR wave is transmitted into the host material by energy coupling. During wave propagation, some energy will be lost and absorbed by the material. Heat is one of the fundamental forms of loss. The attenuation describes the loss of energy and the attenuation rate is determined by Equation 2.2.3.2.4-1 and 2.2.3.2.4-2.

$$\alpha = \omega \left[\frac{\mu\varepsilon}{2} \left(\sqrt{1 + \frac{\sigma^2}{\varepsilon^2 \omega^2}} - 1 \right) \right]^{1/2} \quad (2.2.3.2.4\text{-}1)$$

$$\omega = 2\pi f \quad (2.2.3.2.4\text{-}2)$$

Where, α = The attenuation factor (db/m),

ω = Angular frequency,

f = Frequency,

σ = Electric conductivity,

$\mu = \mu_r \mu_o$ = Magnetic permeability of a material, μ_r = Relative permeability and μ_0 = Permeability of a free space (4π x 10^{-7})

$\varepsilon = \varepsilon_r \varepsilon_0$ = Permittivity of a material, ε_r = Relative permittivity, ε_0 = Permittivity of a free space (8.854 x 10^{-12} Fm^{-1}).

The scattering will also cause attenuation and will induce clutter noise in the radargram.

2.2.3.3 Types of GPR wave

An interaction between GPR wave and host material is that different GRP waves will be created as explained in Figure 2.2.3.3-1 including air wave, ground wave, refracted and critically refracted wave, and reflected wave (Huisman, et al., 2003).

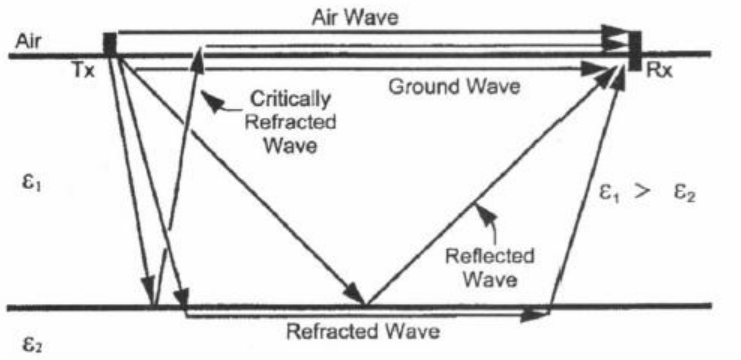

Figure 2.2.3.3-1 GPR wave propagation in host material with different dielectric constant (Giannopoulos, 1998)

Air wave – The electromagnetic wave emitted by the transmitter to the receiver via the air as medium, i.e. the travelling speed, c = 0.2998 m/ns, which will first received by the receiver. The air wave can be neglected if the antenna is thoroughly shielded.

Ground wave – The electromagnetic wave generated by the transmitter propagates along the ground surface to the receiver. For small separation between transmitter and receiver, i.e. common offset antenna, the travelling time difference from transmitter to receiver between the air wave and the ground wave is little and is not able to distinguish by the GPR system. This is commonly referred to as a 'direct wave'.

Refracted wave – The refracted electromagnetic wave can only be received and recorded under survey by using the common mid-point method and wide-angle reflection and refraction method.

Critically refracted wave – The reflected electromagnetic wave is critically refracted at the surface of the host material.

Reflected wave – The reflected electromagnetic wave can be received and recorded when the GPR wave bounces back to the receiver when encountering an interface between two different materials with significant dielectric differences. The amplitude of the reflected wave is proportional to the amplitude of the incident wave and is determined by the reflection coefficient as explained in Equation 2.2.3.3-1.

$$Reflection\ coefficient\ (R) = \frac{\sqrt{\varepsilon_{r1}} - \sqrt{\varepsilon_{r2}}}{\sqrt{\varepsilon_{r1}} + \sqrt{\varepsilon_{r2}}} \quad (2.2.3.3\text{-}1)$$

Where, ε_{r1} = relative permittivity of the host material,

ε_{r2} = relative permittivity of the target object

The value of reflection coefficient ranges between -1<R<1 and can be either positive or negative. If the difference between ε_{r1} and ε_{r2} is small, i.e. ε_{r1} and ε_{r2} are close, the incident wave is transmitted through the interface of the materials. The sign of the reflection coefficient explains that the reflected wave experiences the change/reverse of polarity.

2.2.4 Resolution affected by the physical and geometrical constraint

2.2.4.1 Vertical Resolution

Vertical resolution emphasizes the minimum vertical separation distance between two closely spaced reflection events that can be differentiated by the GPR system as separate events and it is determined by the wavelength of the reflected waves. The minimum vertical separation distance is between one-quarter and one-eighth of the nominal wavelength of the reflected wave (Kearey et al., 2002). In reality, the minimum vertical distance is half of the nominal wavelength. The wavelength can be expressed in Equation 2.2.4.1-1 (Reynolds, 2011; Yilmaz, 2001).

$$\lambda = \frac{v}{f} = \frac{c}{f\sqrt{\varepsilon_r}} \quad (2.2.4.1\text{-}1)$$

Where, λ = wavelength of the transmitted GPR wave,

c = the speed of light in a vacuum,

f = the frequency of the GPR wave, and

ε_r = the relative permittivity of the host material.

Refer to Equation 2.2.4.1-1, the vertical separation distance is governed by the frequency of the transmitted GPR wave by the antenna and the relative permittivity of the host material.

2.2.4.2 Horizontal Resolution

The horizontal resolution emphasizes the minimum horizontal distance between two closely spaced reflection events at the same depth that can be differentiated by the GPR system as separate events (Daniels et al., 1998; Yilmaz, 1988). The GPR antenna emits the electromagnetic wave and spreads in a conical form footprint into the host material. The conical footprint can be referred to as the First Fresnel Zone and its radius of the conical footprint can be expressed by Equation 2.2.4.2-1 (Pérez-Gracia, González-Drigo, & Di Capua, 2008; Reynolds, 2011).

$$r = \sqrt{\left(\frac{\lambda^2}{16} + \frac{\lambda z}{2}\right)} = \sqrt{\left(\frac{v^2}{16f^2} + \frac{vz}{2f}\right)} \qquad (2.2.4.2\text{-}1)$$

Where, r = radius of the conical footprint,

λ = wavelength of the transmitted GPR wave,

z = the travel distance, i.e. penetration depth, of the GPR wave,

v = the GPR wave travelling velocity, and

f = the frequency of the GPR wave

The conical footprint can be expressed by another Equation 2.2.4.2-2 (Annan, 2009).

$$r = \frac{\lambda}{4} + \frac{z}{\sqrt{\varepsilon_r - 1}} \qquad (2.2.4.2\text{-}2)$$

Where, r = radius of the conical footprint,

λ = wavelength of the transmitted GPR wave,

z = the travel distance, i.e. penetration depth, of the GPR wave, and

ε_r = the relative permittivity of the host material.

According to Equation 2.2.4.2-1 and 2.2.4.2-2, the horizontal distance, i.e. 2r, is governed by the GPR antenna frequency, the relative permittivity of the host material and GPR wave travelling velocity in the host material.

2.2.5 Resolution affected by GPR system

2.2.5.1 A-scan, B-scan and C-scan

The X-axis or y-axis is the travel distance when the GPR antenna travels and the z-axis is the time axis in which the GPR wave propagates downward into the object and is reflected to the receiving antenna, i.e. the depth of the reflected can be determined. When the GPR antenna is stationed at a single point, i.e. O, and the GPR wave transmits and receives, an A-scan result with a single waveform will be obtained as shown in Figure 2.2.5.1-1a. When the GPR antenna travels in either the x or y direction, a series of A-scan for each point aligned on the travel will be obtained. Combining the series of A-scan for each point will provide the B-scan which shows the sectional view of the travel as shown in Figure 2.2.5.1-1b. For the C-scan, it provides a plan view formed by the x and y axis with information on the axis as shown in Figure 2.2.5.1-1c. C-scan can be generated by slicing and interpolating B-scan results in both x and y directions (Benedetto et al., 2017; Jol, 2009 and Luo et al., 2019).

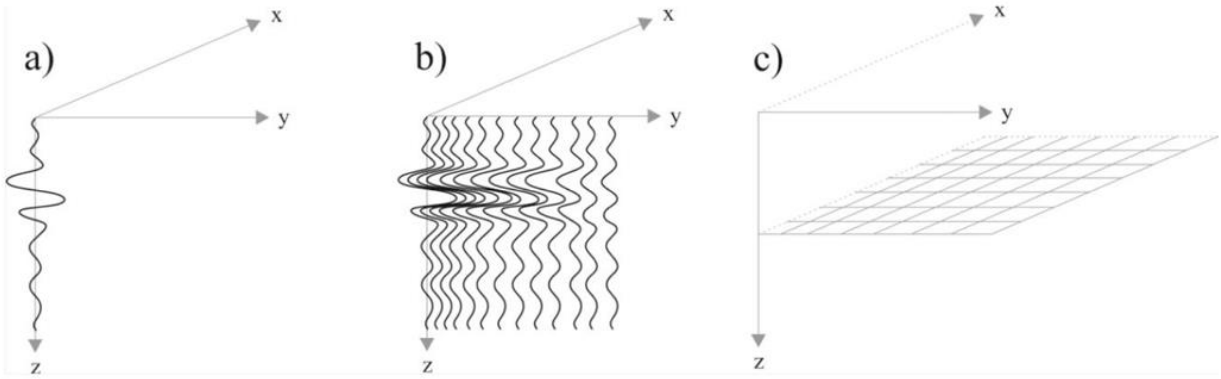

Figure 2.2.5.1-1 Diagrams of A-scan, B-scan and C-scan in GPR survey (Benedetto, et al., 2017)

2.2.5.2 Resolution of digitization in radargram

The function of the control unit of the GPR system is to convert an analogue-to-digital signal and the digitalization process resampling the signal to form an A-scan waveform. According to the Sampling Theorem, a continuous A-scan waveform can be formed via the digitization process if sufficient samples are collected along the z-axis, i.e. time axis. Stacking the series of A-scan can produce a B-scan radargram. The magnitude of the pixel is determined by the reflection amplitude can be diminished or magnified by the gain function.

Hence, the vertical resolution, i.e. sampling interval (Δt) of each sample, in the B-scan radargram is determined by $\Delta t = \frac{time\ window}{samples\ per\ A-scan}$ for each of the A-scan. The horizontal resolution, i.e. horizontal distance interval (Δx), between each A-scan is determined by $\Delta x = \frac{1}{scans\ per\ meter}$.

2.3. Common offset antenna

2.3.1. Choose of GPR antenna

The choose of a GPR antenna is associated with the selection of the centre signal frequency of the antenna to be emitted. A wide range of antenna with different centre frequencies ranging from 100MHz to 3GHz, or even higher frequencies of 4GHz and 6GHz as shown in Figure 2.3.1-1. For structural or building diagnosis, an antenna with a centre frequency ranging from 900MHz to 3GHz is applied since the higher the centre frequency antenna can provide more accurate measurement, more detailed information and higher clarity of radargram. However, the trade-off of using higher centre frequency antenna is the limited measuring depth, i.e. suitable for shallow depth measurement. For the underground utility survey, the range of centre frequency ranging from 100MHz to 1000MHz as the searching depth would be higher and good for measuring utilities below ground for a few metres.

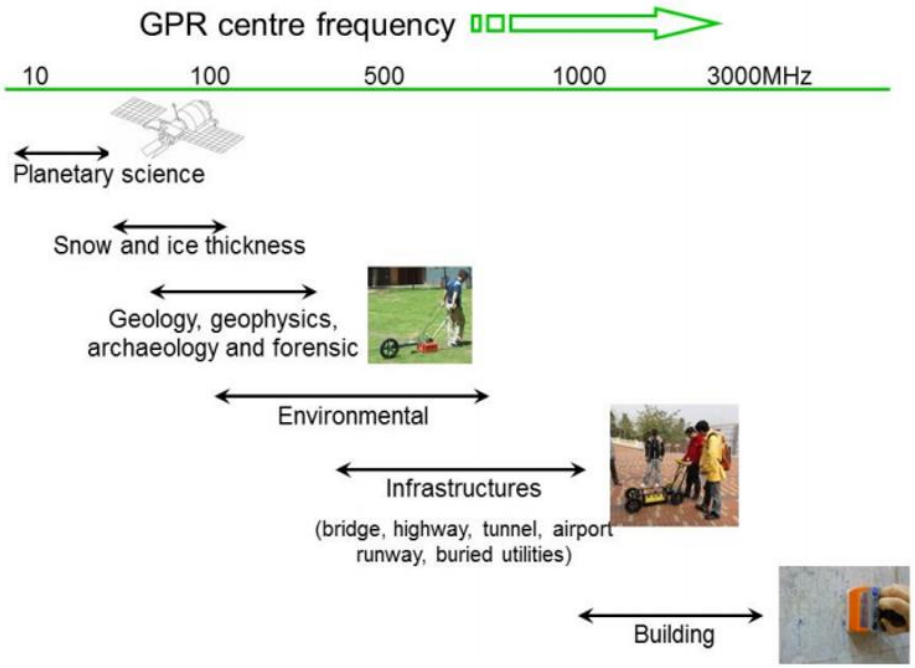

Figure 2.3.1-1 Antennas of different frequencies for various applications (lecture notes from Lai, W.L.W.)

2.3.2. Setting of time window

Time window calculation and setting of the time window in the GPR system is vital as it determines vertical resolution by system digitalized sampling rate along the A-scan waveform and it can be set under samples/scan in the setting of the GPR system. While, for horizontal resolution, it is controlled by scans/metre in the setting of the GPR system which determines the sampling rate or interval of signal transmit for every metre measured by the odometer. To compute the time window, the parameters of the relative permittivity ($\widetilde{\varepsilon_r}$) of host materials and the estimated maximum depth (D_{max}) of the target have to be made and the determination of it can be found in the following equations,

$$v = \frac{c}{\sqrt{\widetilde{\varepsilon_r}}} \tag{2.3-1}$$

$$t = \frac{2D_{max}}{v} = \frac{2D_{max} * \sqrt{\widetilde{\varepsilon_r}}}{c} \tag{2.3-2}$$

$$Time\ window = k * t\ (normally\ 1.3 \leq k \leq 2) \tag{2.3-3}$$

where, v = estimated GPR wave propagation velocity,

c = speed of electromagnetic wave in free space,

$\widetilde{\varepsilon_r}$ = approximated relative permittivity of the host materials,

t = estimated two-way travel time (TWTT, by theoretical),

D_{max} = estimated maximum depth of the target, and

k = safety factor to allow some unexpected uncertainty, e.g. object may be found at deeper location than expected.

2.3.3. Signal transmission and receiving of detected object

Common offset antenna, i.e. monostatic type with antenna common offset distance, located at a point. x_1, on the host material such as air, earth surface or concrete surface, transmits EM signal by the transmitter which spreads in the form of a conical footprint down to the host material. The signal propagates to the target object such as pipe or reinforcement with high dielectric contrast with the host material and signal reflection takes place. The receiver inside the antenna received the reflected signal and counted the time for the signal to and from the transmitter-object-receiver. This is called Two-way Travel Time (TWTT) as shown in Figure 2.3.3-1 and t_1 is recorded since the antenna is located at Position 1, i.e. x_1. When the antenna moves from Point 1 to 0, i.e. $x_{i|i=1\ldots0}$, the above signal transmit and receive keep happening until the antenna reaches on top of the object at Position 0, i.e. x_0, and the TWTT, t_0, recorded. Refer to Equation 2.2.2.1-5, the travelling velocity (v) of the GPR wave in the host material can be found if the relative permittivity constant for the corresponding host material is known with the assumption that the host material is homogeneous material or heterogeneous material with little or insignificant changes in real permittivity of the materials. With TWTT at different positions, and depths at different points plotted a spread of curve in the shape of a diffractive hyperbola. This hyperbolic shape of reflection shows the apex which is the closest point between the surface of the host material to the target object and the shortest TWTT recorded. The ray-path model shown in Figure 2.3.3-1 shared the basic concept GRP survey and became the fundamental model for the development of single, semi-, multi- and full ray-path models in a later chapter of this thesis.

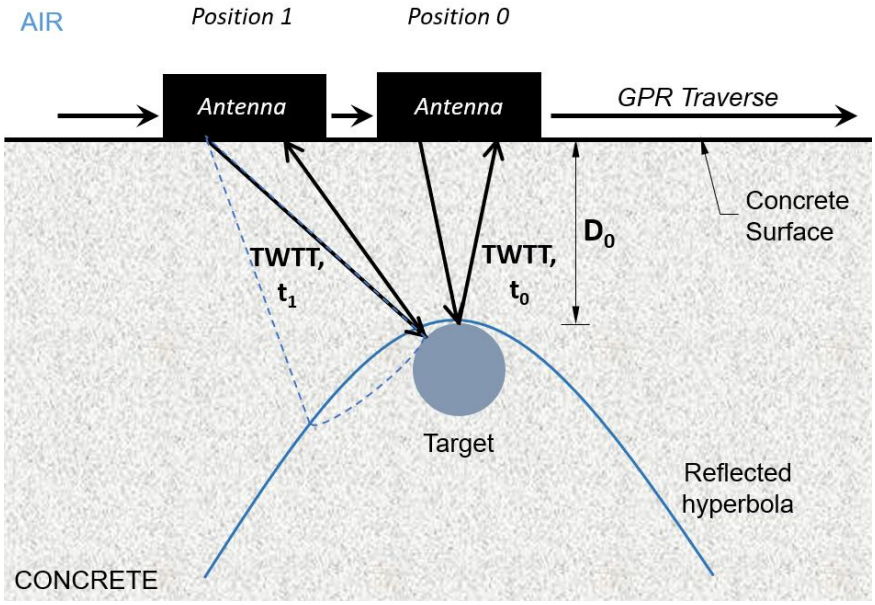

Figure 2.3.3-1 The construction of hyperbolic reflection in underground utility survey by GPR

Radargram shown in Figure 2.3.3-2 shows a typical B-scan result obtained in a GPR survey on reinforced concrete by using a common offset antenna with a nominal centre frequency of 2GHz. Each of the diffractive hyperbola represents the reflected signal by reinforcement and provides the necessary information to study the GPR wave propagation velocity (Hayakawa & Kawanaka, 1998; Lai et al., 2016; Sham & Lai, 2016; Tillard & Dubois, 1995), the estimation of depth of the object (Sham & Lai, 2016, Lau et al, 2021), orientation of the object (Lai et al. 2016), properties of the host materials (Boniger & Tronicke, 2011; Guy et al., 1999; Lai et al., 2006; Lai et al., 2009; Lai, 2006), water content of the host materials (Lai & Wiggenhauser, 2011, Lai et al., 2011) and condition assessment of the host materials (Cao & Al-Qadi, 2022).

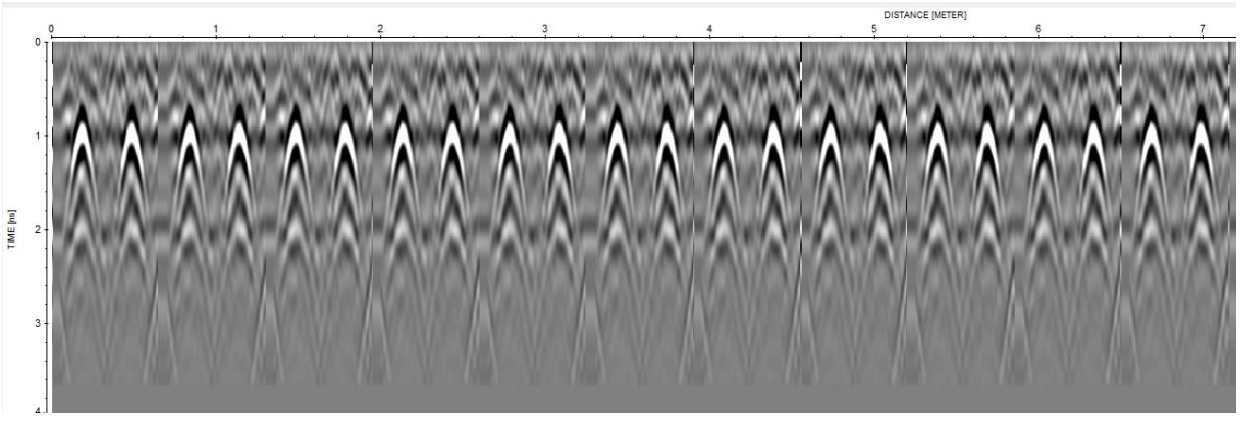

Figure 2.3.3-2 Radargram of reflected wave of reinforcement in concrete by 2GHz antenna

2.3.4. Data extraction and processing

Data obtained after the GPR survey will be processed according to LSGI (2019) by using an in-house developed LabVIEW program with the function of a graphical user interface (GUI) as shown in Figure 2.3.4-1 (Sham & Lai, 2016). For the region of interest, particular A- and B-scan show the corresponding reflected signal of each point in the radargram and diffractive hyperbolas of the reflected GPR signal respectively. Velocity analysis and Two-way Travel Time (TWTT) based on different ray-path models and related algorithms can be performed after proper setting including the type of antenna that affects antenna separation, size and depth of the target object, time zero position and accuracy.

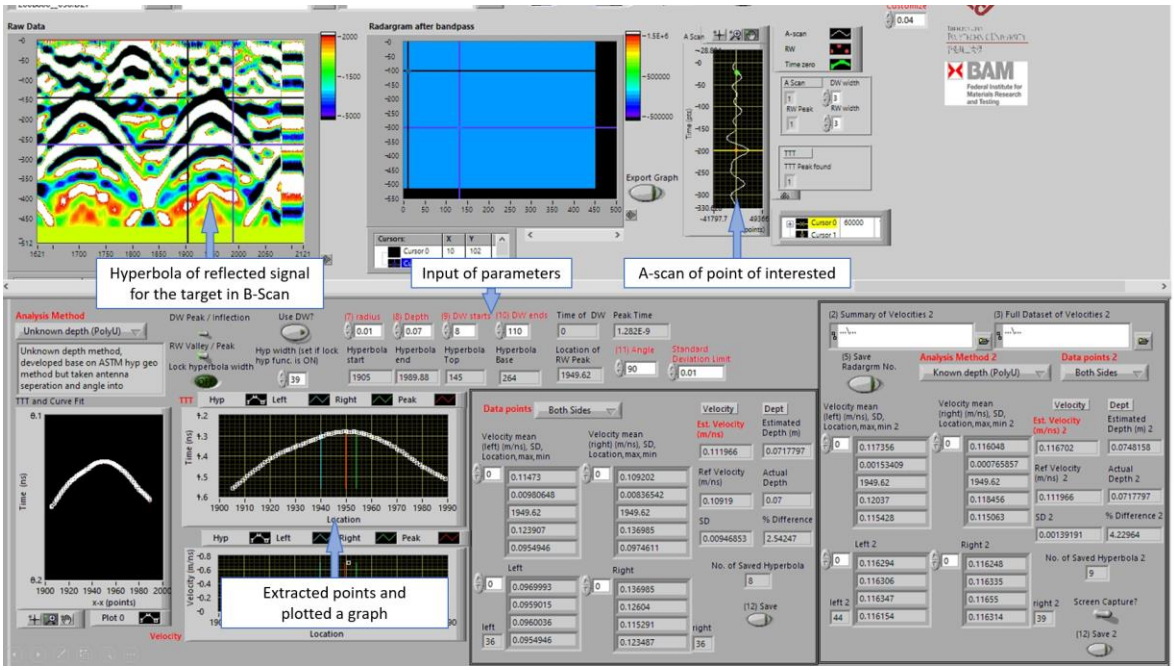

Figure 2.3.4-1 In-house program for data extraction and processing developed under the LabVIEW program

2.3.5. Time-zero

Time zero is the zero-time position in radargram when the GPR wave started propagating to the host material and it is a key parameter to accurately measure the Two-Way Travel Time (TWTT) of the zero-time position to the apex of the reflected hyperbola of the target object and velocity, and resulting in estimating the depth of the target object. The definition of zero-time position is critical for every GPR survey and data processing. In general, (1) the first peak of the first reflected signal, i.e. neither negative, i.e. Point B of Figure 2.3.5-1, or (2) positive, i.e. Point E, or (3) the

zero amplitude, Point C, between both peak in A-scan is identified as zero-time position in the signal, or (4) point with high frequency, i.e. Point A, or (5) point defined automatically between the positive and negative peak of the first reflected signal by using an algorithm, i.e. Point D.

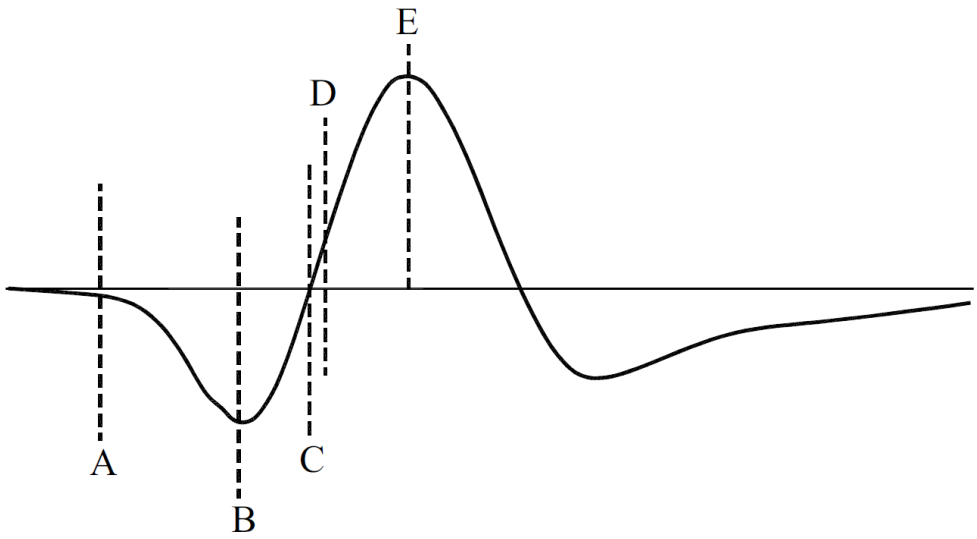

Figure 2.3.5-1 Zero-time position A-E on the reflected direct wave in A-scan radargram (Yelf, 2004)

As depicted, choosing a stable and identified point of the first reflected direct wave is the important key point to deciding the time-zero point (Yelf, 2004). In this thesis, having studied the A-scan result after the experiment, inflection point, i.e. Point C, where it is the transition turning point between position amplitude to negative amplitude, i.e. zero amplitude, is applied.

2.4. Models and algorithms of depth estimation

The calculation of a target's depth involves the two factors of GPR wave velocity and two-way travel time. In addition to its use of in-depth estimation, an accurately estimated GPR wave travel velocity can also help with the condition assessment of underground utilities (Costello et al., 2007; Hao et al., 2012), characterization of the host material (Lai et al., 2011b; Lai et al., 2009), and mapping the underground water content distribution (Lai et al., 2010; Lai et al., 2012; Lai et al., 2016 For a common offset mode antenna, the major algorithms for velocity estimation are 'Depth to known reflector', 'ASTM method', 'Hyperbolic fitting method', and 'Sham and Lai's algorithm'.

2.4.1. Velocity algorithm (Depth to known reflector)

The equation estimates the GPR wave velocity by measuring the total travelling time from the GPR to the object, and back, i.e. two-way travel time, and the depth of the object from a flat surface.

$$v = \frac{2D}{t} \tag{2.4-1}$$

where:

t = measured time for the GPR wave to travel in between the antenna and the object,

D = distance between the target object and the surface of the host material.

2.4.2. Velocity algorithm – method in ASTM D6432-2019 (circular object and single trilaterated method)

The equation is established based on the assumption that the target object and GPR antennas, i.e. transmitter and receiver, are point sources. In other words, the antenna separation distance between the transmitter and receiver, and object size are not considered.

$$v(x_i) = \left(\frac{2}{t_0}\right)\left[\frac{x_i}{\sqrt{\left(\frac{t_i}{t_0}\right)^2 - 1}}\right] \tag{2.4-2}$$

where:

x_i = distance between the transmitting antenna at an oblique position '*i*' and the receiving antenna at a position where the apex of a hyperbola is located. It is considered that the travel of the GPR antenna and the alignment of the object are at a right angle,

t_i = measured time for the GPR wave to travel in between the antenna and the object where the antenna is located at position '*i*',

t_0 = measured the time for the GPR wave to travel in between the antenna and the object where the antenna is located on top of the object, i.e. location of the apex of the hyperbola.

2.4.3. Velocity algorithm – point form target and measured by semi-trilaterated ray-path method

Velocity algorithm – point form target and measured by trilaterated ray-path method

$$v(x_i) = \sqrt{\frac{2(x_i \sin\theta)^2 t_i \pm 2x_i \sin\theta \left((x_i \sin\theta)^2 t_i^2 - 4B^2 t_i^2 + 4B^2 t_0^2\right)^{0.5}}{t_i^3 - t_0^2 t_i}} \quad (2.4\text{-}3)$$

where:

x_i = distance between antennas at position 'i' and antenna at a position where the apex of a hyperbola is located,

θ = angle between the travel of the GPR antenna and the alignment of rebar,

B = distance between the mid-point of the monostatic antenna and Tx and Rx antennas respectively,

t_i = measured time for GPR wave to travel in between the antenna and the object where the antenna is located at position 'i',

t_0 = measured time for the GPR wave to travel in between the antenna and the object where the antenna is located on top of the object, i.e. location of the apex of the hyperbola.

Comparing the ASTM Method and the Semi-Trilaterated Method, the Semi-Trilaterated Method has more advantages than the ASTM Method as the Semi-Trilaterated Method considers the antenna separation distance between transmitter and receiver in the wave path, the radius of the cylindrical target and uses a hyperbolic fitting method to conduct analysis. The effect of antenna separation would be crucial as the low-frequency antenna has a larger antenna separation and hence increases the length of the wave path.

2.4.4. Velocity algorithm – multi-trilaterated ray-path with known parameters/available information, size and depth of target object

The equation included prior-known parameters/available information from as-built record drawings of the target objects, including the size and depth of the object from the surface of the host material (Sham & Lai, (2016); Xie et al. (2018)) as shown in the programming platform in Figure 2.4.4-1 and Figure 2.4.4-2.

$$v_i = \frac{1}{t_i} * \{ \sqrt{\left[(D_o + r) - \frac{(D_o + r)r}{\sqrt{(D_o + r)^2 + x^2}}\right]^2 + \left[\left(x - \frac{r \times x}{\sqrt{(D_o + r)^2 + x^2}}\right) - \mathrm{B}\right]^2} \quad (2.4\text{-}4)$$

$$+\sqrt{\left[(D_o+r)-\frac{(D_o+r)r}{\sqrt{(D_o+r)^2+x^2}}\right]^2+\left[\left(x-\frac{r\times x}{\sqrt{(D_o+r)^2+x^2}}\right)+B\right]^2}\}$$

where:

x_i = distance between antennas at position 'i' and antenna at a position where the apex of a hyperbola is located,

θ = angle between the travel of the GPR antenna and the alignment of rebar,

D_0 = distance between the target object and the surface of host material based on equations (1) & (3),

r = size of round-shaped object, i.e. radius,

B = distance between the mid-point of the monostatic antenna and Tx and Rx antennas respectively,

t_{x_i} = measured time for GPR wave to travel in between the antenna and the object where the antenna is located at position 'i',

t_0 = measured time for the GPR wave to travel in between the antenna and the object where the antenna is located on top of the object, i.e. location of the apex of the hyperbola.

Angle ('θ') is measured from the grid of the GPR antenna traverse and alignment of rebar after image processing in 3D. The size of the object ('r') and the distance of antenna separation can be obtained from the as-built record drawing and the manufacturer's specification, respectively. However, the distance between the target object and the surface of the host material ('D_0') is unknown. It is a paradox for estimating velocity through known depth, with the fact that the depth of the rebar is the purpose of the cover-depth survey of reinforcement bars. This issue was solved by combining and iterating several algorithms of velocity measurement (Lau et al., 2021).

Comparing this Multi-Trilaterated Method with the ASTM Method and Semi-Trilaterated Method, this method is more advanced in that the wave path considered the size of the target utilities/objects and the antenna separation distance simultaneously. However, the deficiency of this method is the prerequisite of the cover depth of the target and input into the analysis. The cover depth should not be known for non-destructive evaluation unless the as-built record is available.

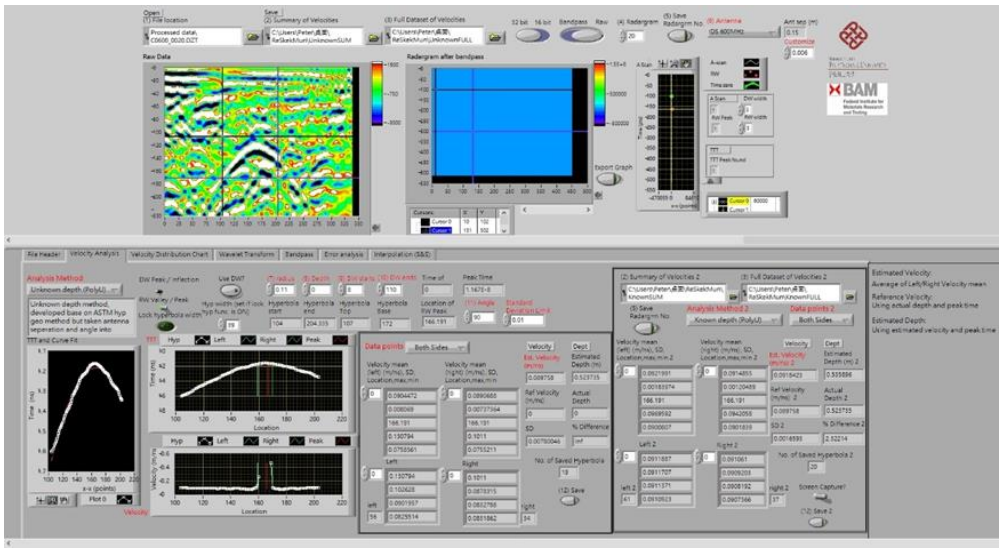

Figure 2.4.4-1 The Graphical User Interface of the LabVIEW velocity analysis program

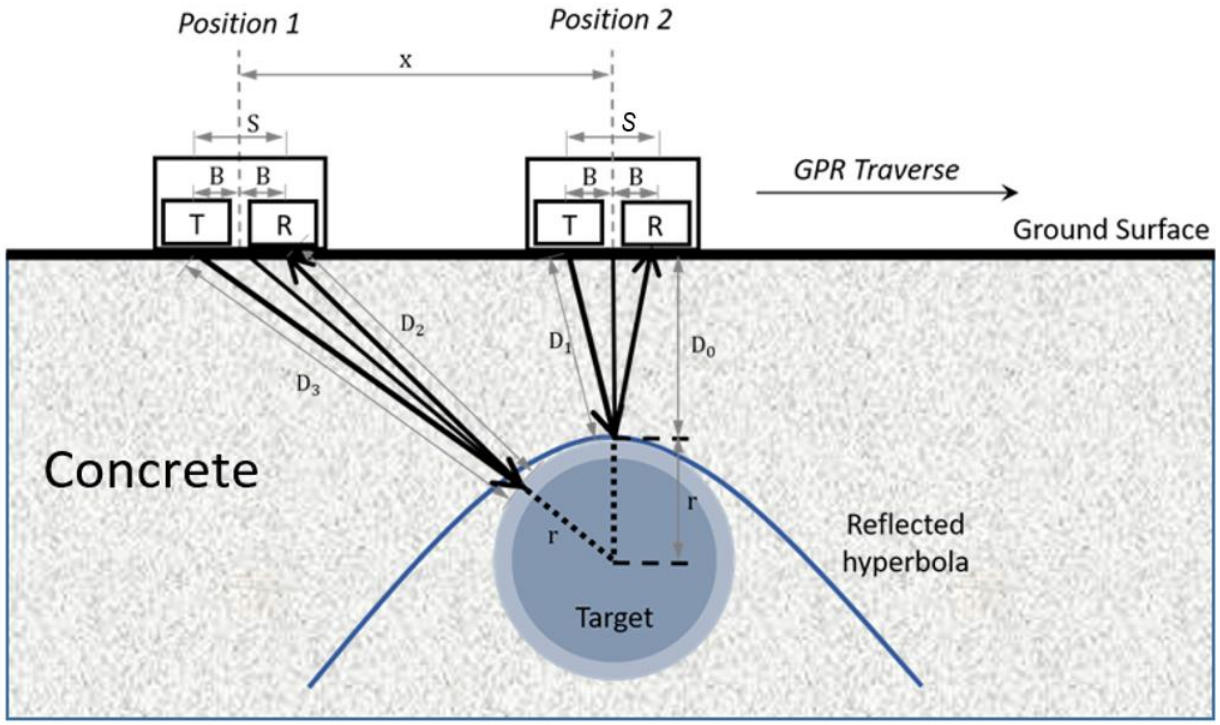

Figure 2.4.4-2 Schematic diagram of the multi-trilaterated ray-path geometry of the common-offset survey of shielded antenna

2.4.5. Combination of algorithms – full trilaterated ray-path with object size and estimated object depth (Lau et al., 2021)

This method considered the combination of algorithms to solve the problem in equation (2.4-4) as shown in figure 2.4.5-1. There are several steps. First, approximated GPR wave velocity 'v' with consideration of antenna separation and target object as a point source is obtained by equation (2.4-3). Second, by making use of an approximated velocity 'v', an 'approximated' 'D_0' is obtained by applying equation (2.4-1). Finally, the input of an 'approximated D_0' helps estimate 'v' and 'd' through equation (2.4-4) and equation (2.4-1) respectively, where estimated 'd' is the measurement of rebar cover depth. Compared to the previous methods, this method offers the advantage, that the velocity outlier can be filtered after setting a standard deviation limit to 0.01m/ns and any data points larger than 0.2998 m/ns (speed of light) at the diffractive hyperbolas.

2.5. Conclusion

The literature review in this chapter strengthened the basic knowledge related to the research in this thesis. It covered the basics theory of electromagnetic theory, factors affecting the research study, depth estimation methodology of objects inside reinforced concrete, and evaluation technique of survey results by Ground Penetrating Radar. It also exhibits the current research gap of cover-depth modelling and error correction of objects in reinforced concrete in near-field by GPR. The initial step of cover-depth modelling and error correction is always the identification and analysis of possible sources of errors during the survey and it is subject to the following chapters.

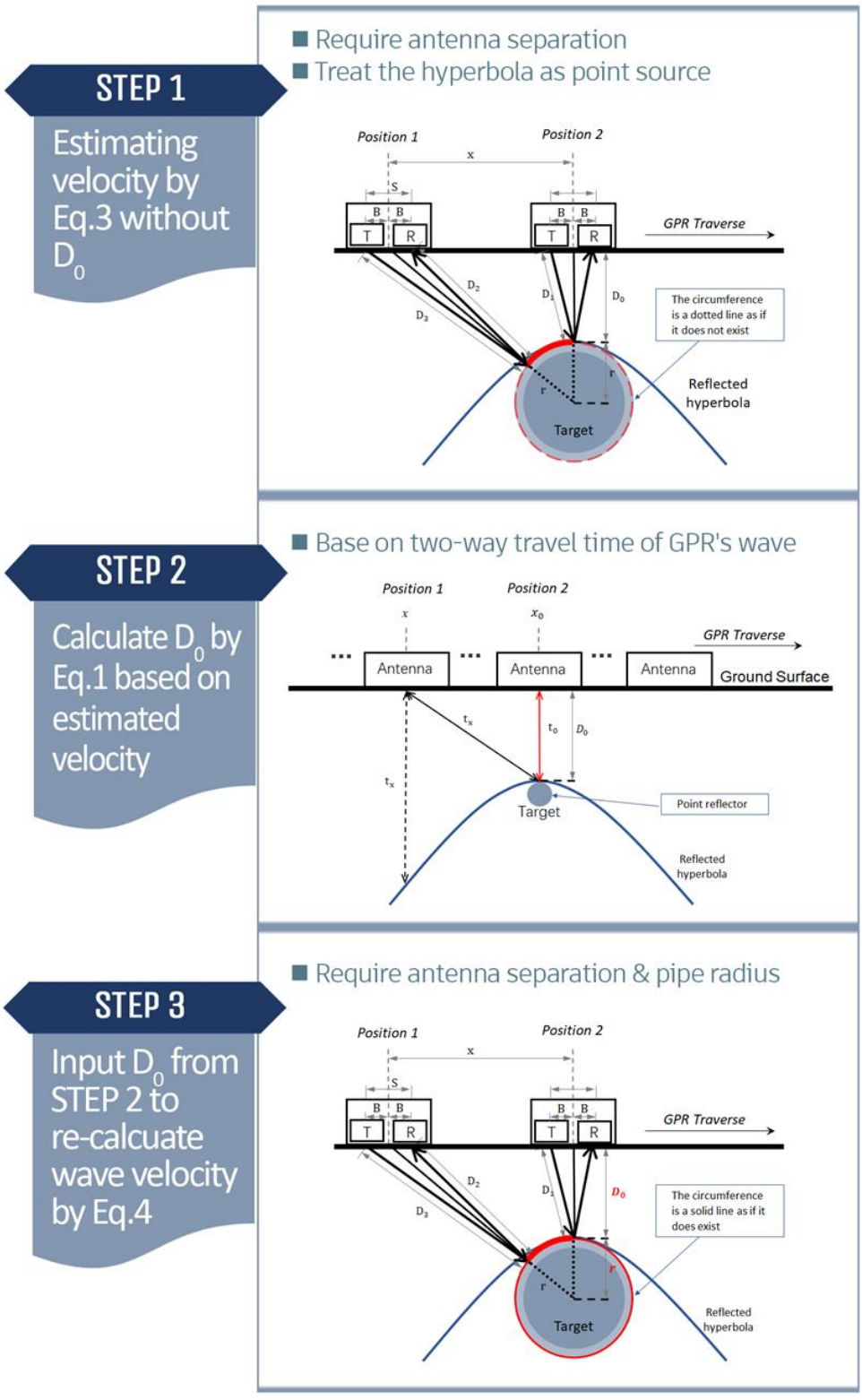

Figure 2.4.5-1 Workflow of the combined GPR wave velocity analytical method based on the geometry in Figure 2.4.4-2

3. Recognition of the possible sources of errors influencing depth estimation

3.1. Assumptions

Before the commencement of the research work, the following assumptions have been made,

(1) The dipole antenna, i.e. transmitter (Tx) and receiver (Rx), in common offset configuration with factory defaulted fixed separation distance between Tx and Rx, i.e. 39mm of GPR 2GHz palm antenna of Geophysical Survey System Inc, was used. Common offset GPR antenna traverse runs and cuts across the alignment of the rebar perpendicularly. GPR wave spread a conical form footprint penetrates the media and reaches a circular object, i.e. reinforcement. Diffractive hyperbola constructed in the radargram after receiving the reflected signal.

(2) All target objects inside the concrete element were buried in the near field region and the GPR wave in the form of a parabolic wavefront spreads and propagates in the medium and reaches the target objects in ray-path mode.

3.2. Potential sources of errors influencing depth estimation

Potential sources of errors are classified into three groups that affect the accurate measurement of cover depth, including (1) dielectric properties of the host materials, (2) geometry of the ray-path of the EM wave, and (3) equipment and signal processing, as tabulated in Table 3.2-1. The potential sources of errors are modelled, evaluated and corrected as explained in later chapters.

Sources of errors		Measured/ dependent variables in this thesis	Related chapters		
			4	5	6
1. Dielectric properties of the host materials	1.1 Water content	x_i, t_i		✓	
	1.2 Heterogeneous materials inside concrete with a size comparable to GPR wavelength, e.g. aggregate	x_i, t_i		✓	✓
2. Geometry of the ray-path	2.1 Common offset profiling (COP)/WARR/CMP	x_i, t_i	Data collection and ray-path model by COP method, and round-shaped rebar		
	2.2 Target types (round/flat/slanted)	x_i, t_i			
	2.3 Object size and antenna separation	x_i, t_i	✓	✓	✓
3. Equipment & signal processing	3.1 Definition of time zero	t_i	✓	✓	
	3.2 Antenna types (bowtie, horn, etc.)	t_i	Dipole antenna with fixed separation distance		
	3.3 Antenna frequency and component frequency of the hyperbolas	t_i			✓
	3.4 Digital sampling rate of the analogue signals	x_i, t_i			✓
4.Combined factor	4.1 Near-field/far-field	x_i, t_i	✓		

Table 3.2-1 Treatments of errors from various sources

Note: Chapter 4 semi- and full trilateration model with effect of near-field and far-field problems on accuracies of cover depth measurement; Chapter 5 semi- and full trilateration model with consideration of effect of ages of concrete and moisture content; Chapter 6 an accurate algorithm to estimate the cover depth based on semi-trilateration method and statistical root mean square errors with uncertainty evaluation

3.2.1 Dielectric properties of host material

Different materials have their dielectric properties which affect the propagation of GPR wave velocity (Chan & Knight, 2001; Lai et al., 2011; Lai et al., 2011a; Lai, 2006). Water is a homogeneous polar material with permanent electric dipole properties, polarization and relaxation behaviour exist when the EM field is applied by the GPR antenna and it significantly affects the propagation of the GPR wave. (Hugenschmidt & Loser, 2008; J. Huisman et al., 2003; Klysz &

Balayssac, 2007; Lai et al., 2012; Lai et al., 2006; Lai et al., 2010; Lai et al., 2014; Topp et al., 1980).

The effect of the presence of water filled in the pores of porous material includes, (1) changing the dielectric properties of that porous material and affecting the propagation of GPR wave because of the difference of the relative permittivity of water and the host material, (2) the quality of the reflected signal will be affected due to polarization of water under GPR wave, and attenuation and absorption of energy of GPR wave underwater, and (3) distortion of GPR wave ray-path due to refraction and diffraction, and resulting in a wrong estimation of travelling velocity and depth.

GPR receiver receive two kinds of signals including true reflection signals from the target object and clutter reflection signals caused by undefined mechanisms and paths that are mixed. Both useful information from the target object and noise due to material surface fluctuations, diffractions, and scattering reflections can be obtained in radargram and lead to misinterpretation of reflected GPR signal in the determination of the target object. Clutter effects are commonly found in radargram when using a GPR survey on heterogeneous material (Oliveira et al., 2021). In GPR, scattering occurs in three different regions including the Rayleigh region, Resonance or Mie region, and Optical region, and the type of scattering is a function of the wavelength of the incident GPR wave and the size of the molecule/particular encountered in the host materials. For Rayleigh scattering, it happens when the diameter of the molecules and particles are many times smaller than the GPR wavelength as shown in Figure 3.2.1-1, i.e. circumference$/wavelength\ in\ x-axis, \frac{2\pi a}{\lambda} \ll 1$, where, a = radius of the molecule/particle, and λ = wavelength. For Mie scattering, it occurs when the essential particles in the host materials with a diameter approximately equal to the GPR wavelength i.e. $\frac{2\pi a}{\lambda} \approx 1$. For the Optical region, it arises when the particles in the host material with a diameter greater than the GPR wave, i.e. $\frac{2\pi a}{\lambda} \gg 1$. In Figure 3.2.1-1, other than the parameter of $\frac{2\pi a}{\lambda}$ in x-axis, another parameter that governs the scattering is the ratio between the strength of the reflected signal from the target object and the reflected signal from a perfectly smooth sphere with a unit cross-sectional area and explained as normalized Radar Cross Section, i.e. RCS/πa^2, in the y-axis. Such a factor determines the type of scattering and affects the errors in depth estimation.

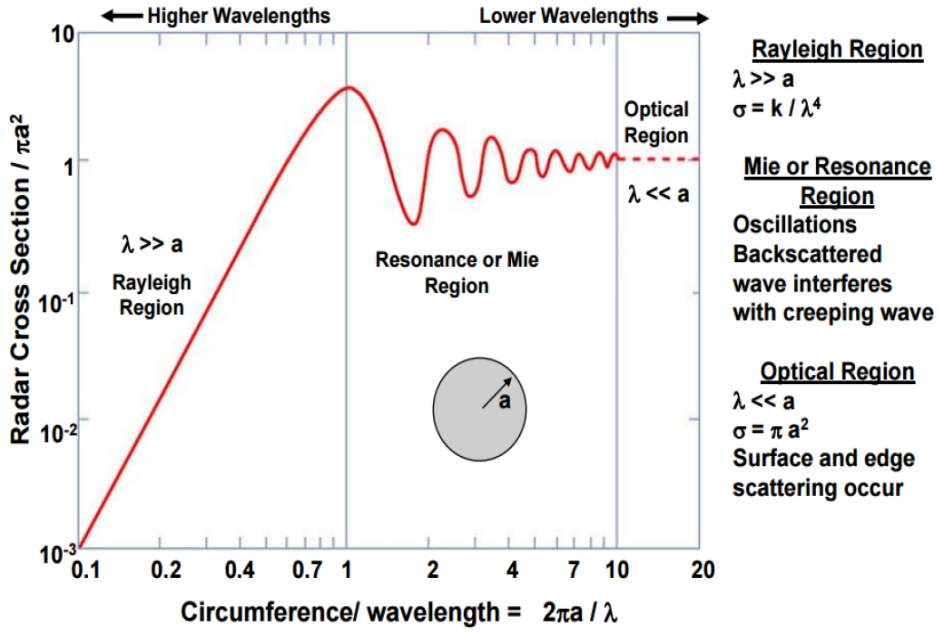

Figure 3.2.1-1 Scattering in Rayleigh region, Mie region and Optical region (A.M. Alzahed and S.M. Mikki (2018))

3.2.2 Measuring techniques and geometry of the ray-path

Three different GPR measuring techniques are widely adopted including, (1) fix-offset or common offset profiling (COP) - the separation of transmitter and receiver is fixed and are moving together simultaneously with the same traverse direction, (2) wide-angle reflection and refraction (WARR) – the transmitter is fixed in a designated position and the receiver is progressively stage-by-stage increasing the distance from the transmitter, and common-midpoint (CMP) – the transmitter and the receiver set a distance away from a common mid-point and both antenna move away from the mid-point with the same distance as shown in Figure 3.2.2-1 (Liu et al., 2017) . In this thesis, the COP measuring technique is adopted, and ray-path modelling is based on COP. Different ray-path models, including single trilateration, semi-trilateration and full-trilateration, were explained in Chapter 2.

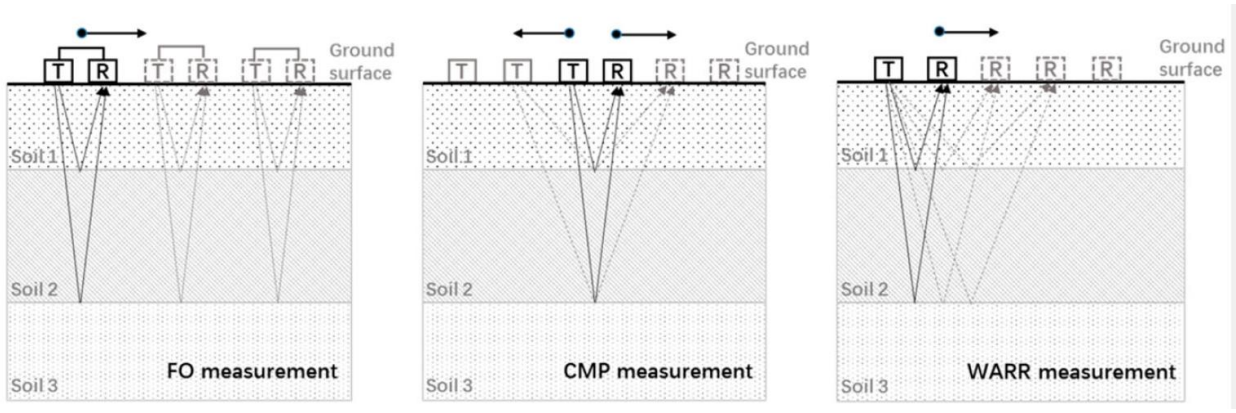

Figure 3.2.2-1 Different GPR measuring techniques (Liu et al. (2017))

3.2.3 Equipment and signal processing

As depicted in Chapter 2, the Two-Way Travel Time (TWTT), and related components of wavelength and frequency are critically impacted by the definition and location of time zero in the A scan radargram and thus it is obvious to know that the setting of time zero decided the uncertainty of all measurements (Ihamouten et al., 2010; Yelf, 2004; Klysz et al., 2004; Wong et al., 2016). In this connection, the higher the resolution of the data can be achieved, and it would be beneficial to the determination of time zero and thus the digitization setting of the GPR setting is crucial.

The configuration setting of the GPR system is the prime important key to the success of the data collection. The digitization setting of the GPR configuration includes the setting of the time-window, the number of samples per scan decided the sampling rate in the A-scan waveform, and the number of scans per meter governed the sampling rate of the odometer of the GPR system. As explained in Nyquist-Shannon (Shannon, 1949) sampling theorem about the sufficient sampling rate, the horizontal and vertical digitization resolution obtained in A/B/C scans are higher if the sampling rate in A-scan waveform and by the odometer is higher as well. As such, to minimize the measurement errors due to traverse run and Two-Way Travel Time (TWTT) in horizontal and vertical directions respectively, the digitization setting was set to the highest value of the GPR system which can be affordable, i.e. 800 scans/meter and 512 samples/scan over a 4.0ns time window, to conduct all tests to collect data.

3.2.4 Combined Factor

GPR signal transmits from the transmitter and propagated into the host material, i.e. air, concrete or soil, which the characteristic of GPR signal varies with respect to the distance from the antenna and the maximum linear dimension of a dipole antenna and is broadly classified into two regions including Near-field region and Far-field region. For the far-field region, it is the region located far away from the dipole antenna by the $\frac{2D^2}{\lambda}$. The near-field region is subdivided into reactive near field and radiative near field or called the Fresnel region. The boundary between reactive near field and radiative near field is $\frac{\lambda}{2\pi}$ for the electrically small antenna which the largest dimension of the antenna is not more than $\frac{\lambda}{10}$ and $0.62 \times \sqrt{\frac{D^3}{\lambda}}$ for the electrically large antenna which the largest dimension of the antenna is greater than $\frac{\lambda}{10}$ (Jol, 2009 & Breed, 2007). The relationship between reactive near field, radiative near field (or called Fresnel region) and Radiating Far Field (or called far field) is shown in Figure 3.2.4-1.

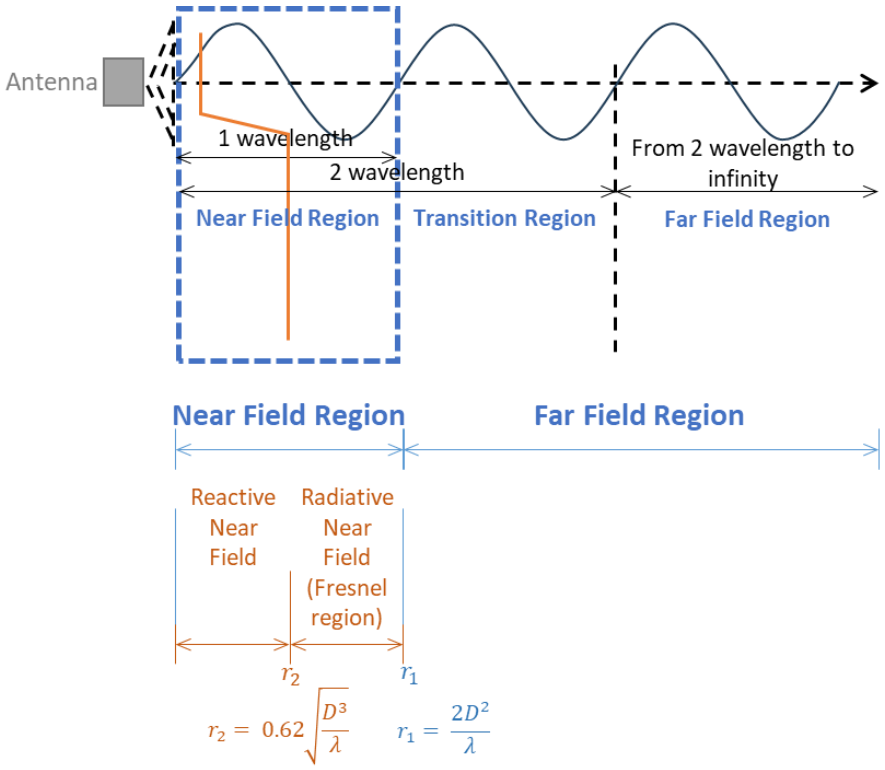

Figure 3.2.4-2 Relationship between reactive near field, radiative near field and radiating far field

3.3. Conclusion

This chapter identified the potential sources of errors and laid the foundation for the study and discussion of using various trilateration models of ray path in common offset profiling (COP) configuration to conduct trajectory error correction (Chapters 4-6) and error minimization (Chapter 7).

4 Effects of near/far-field problems on accuracies of cover depth measurements by semi- and full- trilateration of ray-path

To maintain the structural safety and reliability of a structure during its whole lifespan, it is essential to conduct structural inspections on the quality of building elements in the construction phase and regular structural health monitoring of existing buildings. These inspections and monitoring help verify the quality and integrity of materials and detect any defects or damages that may compromise the structure's performance. Different frequencies of GPR are applied in different areas of non-destructive testing, or near-surface geophysics in construction. One important application is to map utilities below ground, locate rebar and estimate the cover thickness of reinforced concrete elements (Sham and Lai, 2016, Lai et al., 2016 and Pongsak et al., 2017). GPR wave penetrates through layers and mixtures of construction materials or layers of soil and is reflected to the receiving antenna when objects like steel and PVC are interfaced with contrasting dielectric properties within the transmission medium. Reflected signals can be reconstructed to build radargrams after off-site signal processing. The result provides orientations, positions and depths of targeted objects. However, the limitation and error of detecting ranging, i.e. depth of the target object, by GPR is a doubt.

In this study, the often-neglected ranging (or cover depth) error of an object located within the Fresnel Region (or called radiating near-field) and reactive near-field region in GPR is evaluated. Experiments were conducted on concrete specimens with different rebar cover depths ranging from 10 to 80mm to simulate various objects that GPR detects from near-field, Fresnel region and far-field regions. The study aimed to evaluate the effects of rebar cover depth on GPR imaging quality and accuracy. A standard measurement method of cover depth for steel reinforcement within concrete is applied and comparing two developed velocity algorithms (Sham and Lai 2016; Lau et al. 2021) which considered semi-trilaterated and full-trilaterated ray-paths. These algorithms considered common offset antenna and use multiple trilaterated ray-paths to perform the calculations. Velocities of the collected hyperbolic reflection data point of the embedded round reinforcement are computed by developed algorithms with consideration of common offset antenna and multiple trilaterated ray-paths. The method was validated in a laboratory-based control experiment with air as a homogeneous medium of wave velocity equivalent to the speed

of light. Then characteristics of near- and far-field can be better understood before testing the methodology in concrete.

The result of the study shows that the distance estimation is unreliable in the reactive near-field and Fresnel zone but is significantly enhanced when the target is in the far-field zone where GPR waves become planar. The experiments, based on precise modelling of ray-path's trilateration methods, demonstrate that the conventional linear scale of GPR depth conversion ignores the effects of near-field/Fresnel zone. To avoid errors in time-to-depth conversion and depth estimation of objects by GPR, it is recommended that the GPR near-field/Fresnel region and far-field boundary should be considered.

4.1 Near Field and Far Field region

The GPR antenna emits energy to the substrate surface through different methods, including quasi-stationary, induction and radiation fields. The energy exchange occurs in the reactive near field. When the target interacts with the source fields, it produces a signal that is received by the antenna in the far field, also known as the radiated field (Jol, 2009). One of the key concepts in antenna theory is the distinction between near-field and far-field regions. These regions depend on two factors: the size of the source (D), which is the largest dimension of the antenna, and the wavelength of the radiation (λ). The boundary between the near and far fields of a dipole antenna can be determined by the formula $r = \frac{2D^2}{\lambda}$, where r is the distance from the dipole element of the antenna to the point of interest, D is the length of the dipole, and λ is the wavelength of the signal (Jol, 2009; Bienkowski and Trzaska, 2012). The near field region can be divided into two subregions: the reactive near field and the Fresnel region (or radiating near field). The boundary between these sub-regions is given by $r = 0.62\sqrt{\frac{D^3}{\lambda}}$. This equation shows the relationship between the antenna dipole design (D) and the material characteristics (λ). The near-field region is often overlooked in near-surface geophysical and engineering applications of GPR, but it is essential for accurate depth ranging. For the former, i.e. the mathematical derivation of a physical phenomenon, is clearly a non-linear problem. But for the latter, i.e. depth ranging of an object, is usually regarded as a linear problem where depth = two-way travel time x velocity divided by 2.

The linear solution of the latter is far from adequate to fully represent the non-linear nature of the former physical phenomenon. The over-simplified linear solution for ground-penetrating radar (GPR) applications is only valid in the far-field zone and constrained in the reactive near-field and Fresnel zone. However, this solution is commonly used in two important domains of GPR, namely structural inspections and underground utility surveys, where the near-field effects are significant.

4.2 Experimental Setup and Collection of Data

4.2.1 Experimental setup in air and collection of Data

A thin plastic board and two Y10 steel rebars were used in the experiment. The rebars were positioned on a foam box with a height of 860mm, and the gap between the rebars and the GPR antenna was set to 185mm, as illustrated in Figures 4.2.1-1a and 4.2.1-1b. A 2GHz palm antenna from Geophysical Survey System Inc. was employed to scan the two Y10 steel rebars and collect data. The radar measurements were repeated 12 times. Velocity analysis using semi-trilateration equation (2.4-3) (Sham and Lai, 2016) and combined equation/full-trilateration (2.4-3), (2.4-1) and (2.4-4) (Lau et al., 2021) as mentioned in Chapter 2.4 were used to measure the velocity of the reflected wave. The computed velocity in the air was verified.

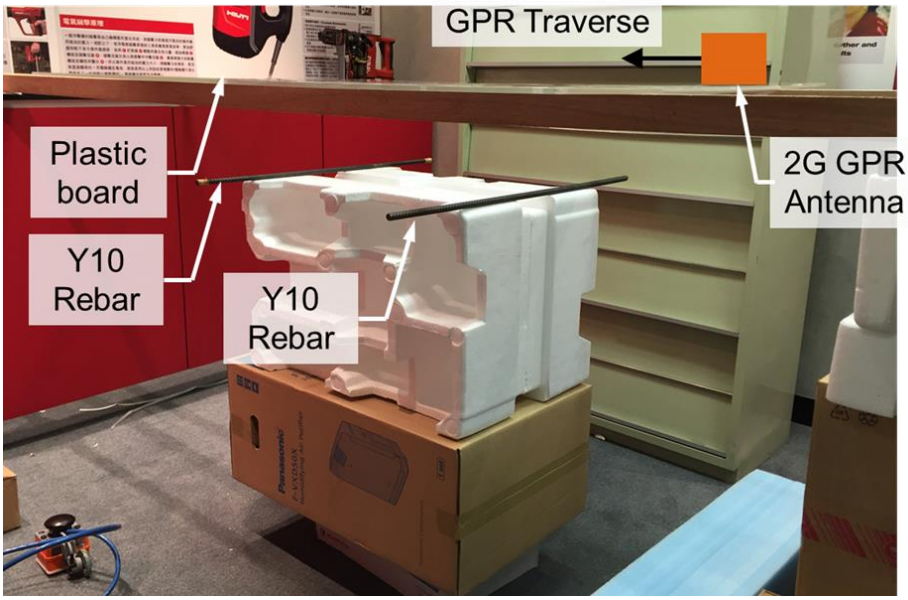

Figure 4.2.1-1a Experimental setup of the stimulated beams

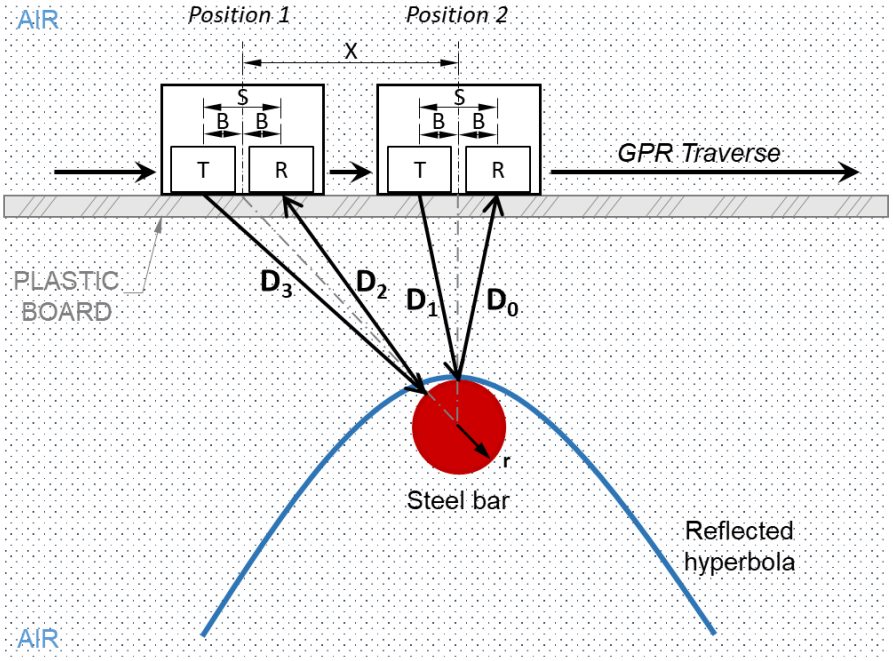

Figure 4.2.1-1b Schematic drawing of the calibration process in air

4.2.2 Experimental setup in concrete and collection of Data

The reinforced concrete elements were beams with dimensions 200mm (Width) x 800mm (Long) x 110 (Depth), as shown in Figure 4.2.2-1. Two diameter 20mm rebars with fixed 300mm centre-to-centre spacing were placed at each end of the concrete beams to the centre of the rebar by 250mm. A similar configuration and number of rebars but with different cover depths were cast into three other concrete beams. Altogether, four cast concrete beams with eight different cover depths of rebars from the concrete face ranging from 10mm to 80mm were cast. This imitates the actual cover depths in all civil engineering applications. The only difference in each beam setup was the cover depth of two rebars, where the cover depth for the pairs of rebars was the same.

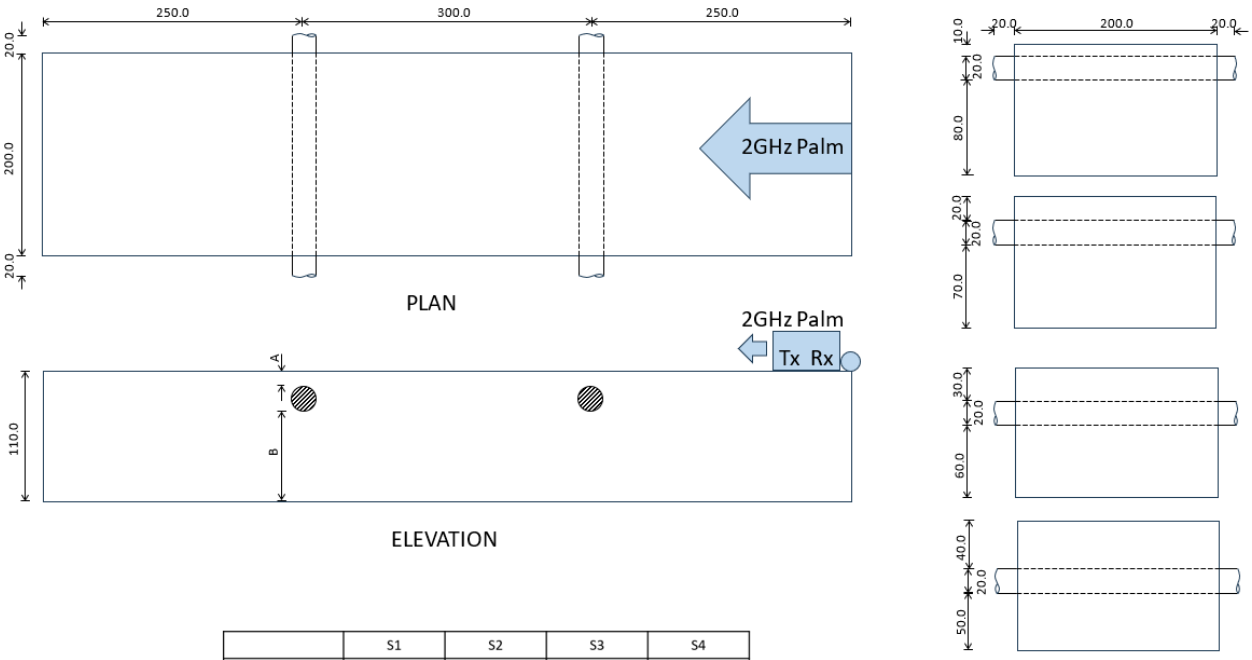

	S1	S2	S3	S4
Cover 1 (A)	10	20	30	40
Cover 2 (B)	80	70	60	50
	S5	S6	S7	S8
Cover 1 (A)	80	70	60	50
Cover 2 (B)	10	20	30	40

NOTE: ALL REBARS ARE DIAMETER 20mm HIGH YIELD BARS.

Cement	335 kg/m^3
Water	190 kg/m^3
Sand	680 kg/m^3
10 mm	381.7 kg/m^3
20 mm	763.3 kg/m^3
w/c ratio	0.57
Average concrete compressive strength (Air cued at 28 days after casting)	44MPa

Figure 4.2.2-1 Experimental setup of the stimulated beams

4.2.3 GPR data acquisition

GPR measurements were done after the concrete was cast and cured at 120 and 180 days. GPR 2GHz palm antenna of Geophysical Survey System Inc was used to scan the concrete beams as it provides a high-resolution measurement of time and distance for shallow cover depth reinforcement. Also, the wavelength of the propagated wave matches the measurement of the

diameter of reinforcement, i.e. 20mm diameter, to produce significant reflections. 12 scans of each cover depth on different days were conducted and, altogether, 384 scans were processed for 2D signal processing and radargram display by commercial software, i.e. ReflexW. Velocity computation based on the trilateration models with hyperbolic fitting as shown in Figure 4.2.3-1, was conducted by an in-house program developed in LabVIEW environment (Sham and Lai, 2016),. The waveform's travelled path was calculated using Pythagoras theorem, since the receiver and transmitter had a common offset distance and were shielded inside a container.

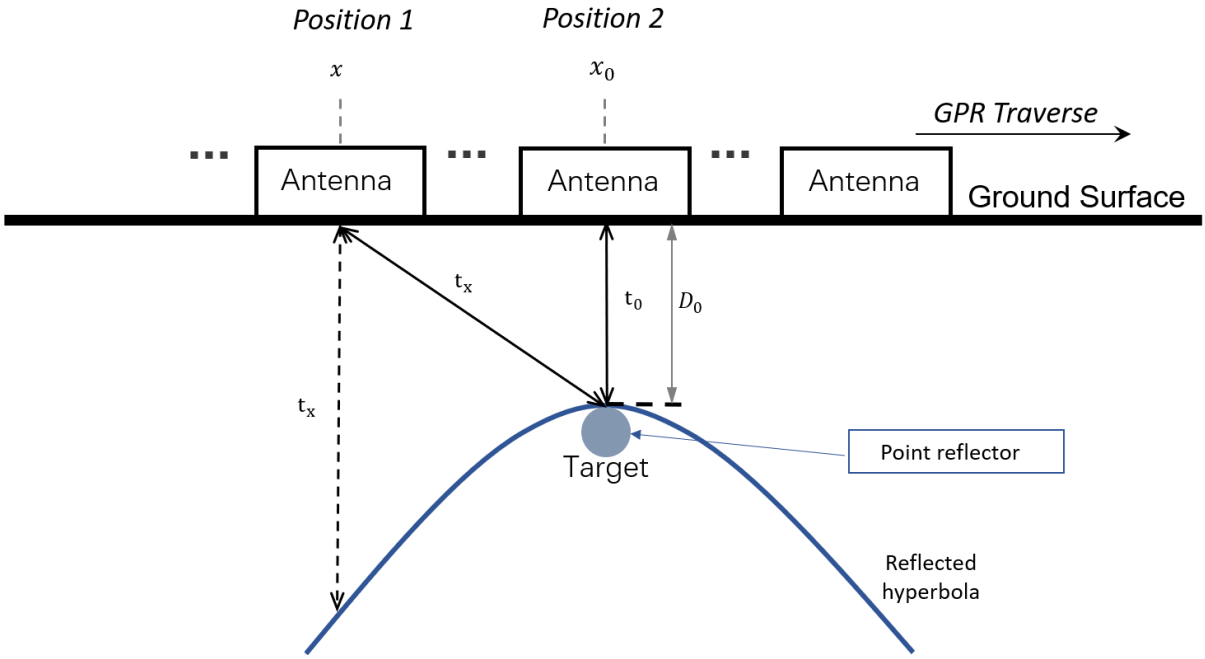

Figure 4.2.3- 1 The reflection model for GPR wave propagation and reflection

4.3 Experimental results and discussion

4.3.1 Data processing

In 2D signal processing, the adjustment of the waveform using direct current shift and standard dewow was conducted before making use of the point of reflection at the direct wave as the time zero. The background and equipment gain of the signal were removed to ensure the authenticity of the signal. After signal processing, data from the radargrams were extracted for velocity analysis of the diffractive hyperbolas by the developed in-house LabVIEW program with developed

algorithms. With measured time of flight at the apex of hyperbolas, cover depths of the rebars were measured and compared with the actual values.

The data processing steps for the 2D signal included applying a DC shift and a standard dewow filter, as well as correcting the time zero which references to the ground. The background noise and the equipment gain were also eliminated from the signal. The radargram data were extracted and the velocities of the diffracted hyperbolas were analyzed using the algorithms developed in the LabVIEW program. The inflection points of each reflected A-scan and formed hyperbolas were configured in the programme and measured to the location of the rebar. Velocities were calculated and the cover depth of the rebars was then measured and compared with the actual values using the time of flight at the hyperbola apexes.

4.4 Experimental results and discussion

4.4.1 Experimental result in air

In a homogeneous medium like air, the GPR wave travels at the speed of light, i.e. 0.2998m/ns without velocity dispersion as a function of frequencies. The GPR wave in the air can be compared with the estimated velocity by Semi-Trilateration equation, i.e. equation (2.4-3), and Full-Trilateration equation, i.e. combining equation (2.4-3), (2.4-1) and (2.4-4) with the input of object depth. This experimental test can verify the constituency of the velocity analytical methods.

The calculated discrete velocities using Semi-Trilateration equation (3) and Full-Trilateration equation (2.4-3), (2.4-1), and (2.4-4) agree with each other, as shown in Figure 4.4.1-1. Comparing the result with the speed of light, results from the Semi-Trilateration equation slightly underestimate the GPR wave velocity by 1.06% to the speed of light and results from the Full-Trilateration equation slightly overestimate by 0.17% to the speed of light. The standard deviations using Semi-Trilateration and Full-Trilateration algorithms are 0.0018m/ns and 0.0016m/ns respectively. The models produced highly accurate estimates of the GPR wave velocity. The errors were very small and acceptable for the methodology. The methodology can be applied to concrete specimens.

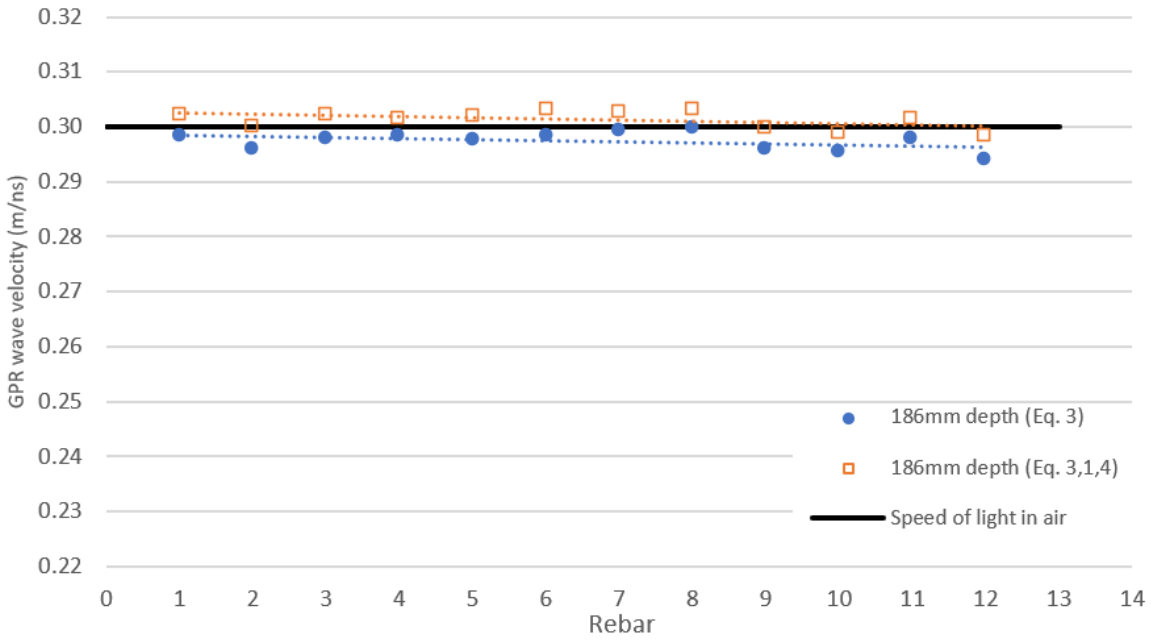

Figure 4.4.1-1 Velocity analysis by different methods with same object depths

4.4.2 Experimental result in controlled experiments

The standard data processing steps for velocity analysis are processed. First, the raw data were processed using the standard method described by LSGI (2019). Second, the velocity analysis was carried out using two methods: Semi-Trilateration method based on equation (2.4-3) (Sham and Lai, 2016), and Full-Trilateration method based on equations (2.4-3), (2.4-1) and (2.4-4) (Lau et al., 2021). Both methods used the LabVIEW program developed (Sham and Lai, 2016), as shown in Figure 4.4.2-1. Third, the 2D velocity profiles were obtained by applying a moving average filter to smooth the data.

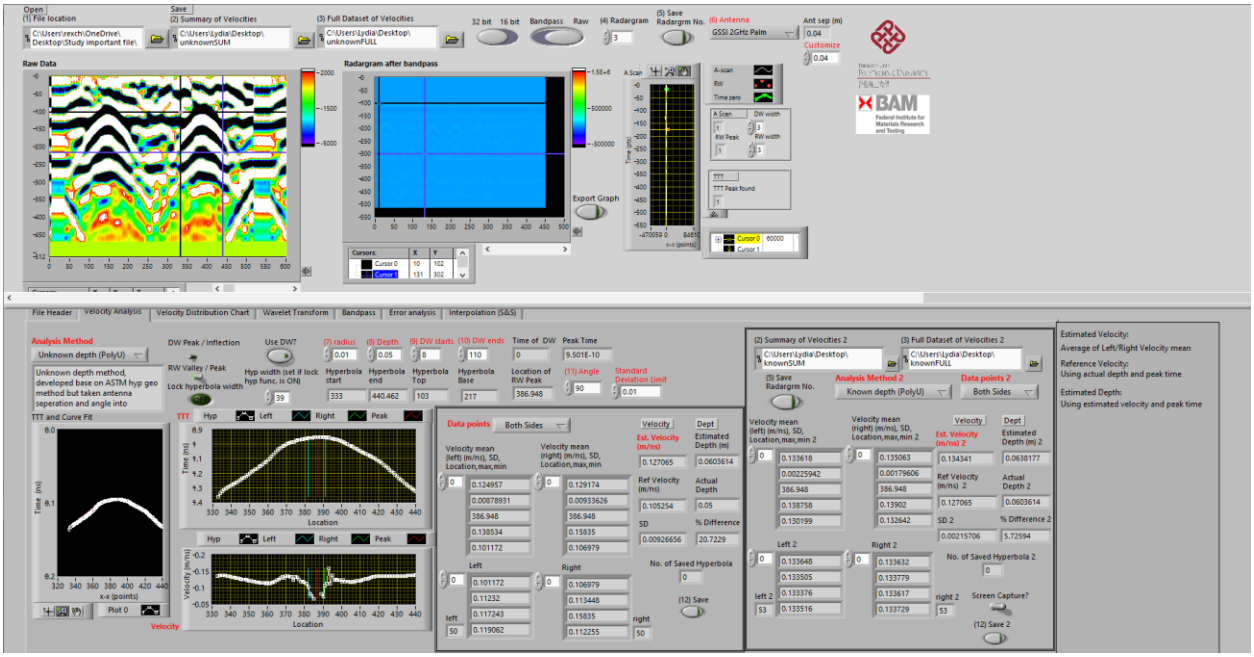

Figure 4.4.2-1 The Graphical User Interface of the LabVIEW velocity analysis program

The effects of GPR near-field on the accuracy of the measured depth of the object are important to obtain accurate results of depth estimation of buried objects, such as rebars in concrete. According to the estimated cover depths for the cover depths from 10mm to 30mm illustrated in Figure 4.4.2-2 comparing the estimated cover depth with actual cover depth, the Semi-Trilateration and the Full-Trilateration models over-estimate by 12.2-9.7mm (136.1-34.5%) and 17.5-14.1mm (153.6-46.1%) respectively. For cover depth of 40mm to 80mm, the estimation was greatly improved and the result of Semi-Trilateration and the Full-Trilateration models over-estimates by 10.6-0.5mm (28.2-1.2%) and 14.3-3.5mm (35.2-5.0%) respectively. The study found that the reactive near-field boundary for GSSI 2GHz palm antennae is about 40mm. This figure matches the calculated near-field reactive boundary based on the equation of $r = 0.62\sqrt{\frac{D^3}{\lambda}}$, where r is the distance between the antenna and target object and D is the aperture's maximum dimension which is 58.5mm for the GPR used in this work. λ ranges from 49.5 to 75.1 mm according to the wavelet transform discussed in Section 2.4.5. The computed r by using Semi-Trilateration and Full-Trilateration models is 36.7mm and 35.1mm, respectively. This analysis justifies the trend that more accurate results can only be obtained along with the larger cover depth of the rebar, as shown in Figure 4.4.2-2. It also suggests that the measurement of the cover depth of rebar is reliable only when an object is located in the Fresnel region, at which the GPR wave propagates as a plane wave.

This chapter shows that the depth estimation of buried objects by GPR is affected by a near-field effect that is often ignored. Many GPR users assume that the depth measurement is accurate without considering the findings of this work. The same effect can also apply to deeper objects with lower GPR frequency, by adjusting the parameters ‘D’ and ‘λ'. Therefore, GPR users should be aware that the depth estimation is not reliable if the objects are in the reactive near-field zone. Only when the objects are in the Fresnel region, the depth estimation can be more reliable.

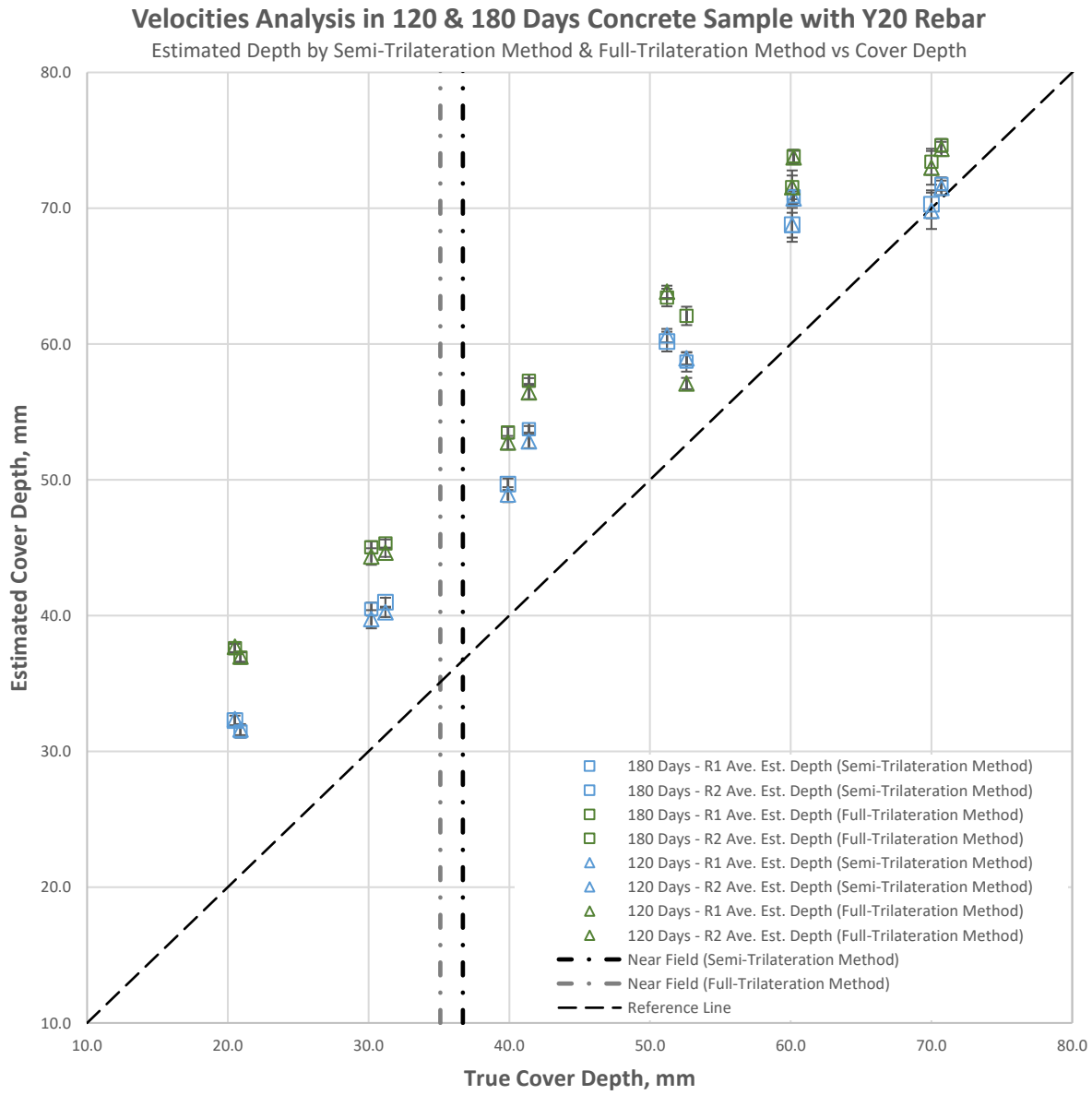

Figure 4.4.2-2 The Graphical User Interface of the LabVIEW velocity analysis program

4.5 Summary and contribution

The high frequency 2GHz antenna was tested to verify the travelling speed of radar waves in air is equal to the speed of light in air, which validates the experimental setup and algorithms before the second experimental validation was done on concrete beams. The full-scale studies of different cover depths of rebars by making use of two different velocity algorithms substantiate the validity of measurement and accuracy. The result revealed that the measurement of concrete cover depth by using a high-frequency 2Ghz antenna is highly doubtful in the reactive near-field region due to a large error ranging from 34.5-136.1%, in comparison to the 1.2-28.2% error in the Fresnel region.

To summarize:

1. this chapter suggests a standard measurement method for rebar cover depth estimation in lossless materials by using Semi-Trilateration and Full-Trilaterated algorithms applied on the GPR diffractive hyperbolas. It considered the actual trilaterated ray-path due to antenna separation and object alignment. Also, the depth of the object can be found by several combined algorithms without prior-known information about the concrete structures and geometries. Both proposed algorithms are much more accurate in estimating the cover depth than the traditional commercial software.
2. this chapter explains the effects of reactive near field and Fresnel region on the accuracy of cover depth measurement of objects. It also reveals the limitation of shallow depth measurement, i.e. <40mm which falls inside the reactive near field zone, by using a 2GHz high frequency antenna. The accurate measurement is only obtainable at cover depth over 40mm which is outside the reactive near field as the smaller deviation from the actual depth and as explained by the far-field theory.
3. this chapter supplements the understanding of depth measurement errors with a simple hyperbolic diffraction model (ASTM method) used by most commercial GPR processing software. It also follows that the findings conclude that the methods can also be used to map other deeper objects with lower GPR frequency.

5 Effects of ages on accuracies of cover depth measurements by semi-trilateration of ray-path: uncertainty evaluation of depth measured by GPR

Electromagnetic characteristics of concrete from fresh mixing concrete to the growth of hardened concrete can be obtained by Ground Penetrating Radar (GPR) measurement on the hyperbolic reflections of embedded rebars. Relative permittivity (or dielectric properties) and peak frequency response behaviour were evaluated via experiment by measuring the variation of GPR A-scan waveforms over a reinforced concrete with six different specified cover depths, 20-70mm, throughout a range of periods at 4, 7, 14, 28, 56, 90, 120 and 180 days. Data analysis was conducted using semi-trilateration velocity models applied on the rebar hyperbolas and wavelet transform. The changes in Two-Way Travel Time and peak frequency in wavelet transform over the age of concrete with eight different cover depths were monitored. The result revealed that the average variation of estimated cover depth for covers 20 to 70 between Day 4 and Day 180 was 0.44mm with a maximum of 1.9mm and the variation of average estimated depth was 0.13mm and 0.02mm at early Day 56 and Day 90 and afterwards respectively. The dielectric constants and Two-Way Travel Time were found to be decreasing steadily and consequently, the peak frequencies were found to be increasing for different cover depths with increasing age of hydrated concrete. The findings were found to be closely related to the cement hydration process which the consumption of free water to react with cement to form bound water and a hydrated product.

5.1 Experimental setup

As explained in Chapter 4, four concrete beams with dimensions 200mm (Width) x 800mm (Long) x 110 (Depth) were cast. For each beam, two diameter 20 mm rebars were cast with eight cover depths ranging from 10mm to 80mm which are widely specified in various types of concrete structures. Radar measurements by using the GPR 2GHz palm antenna of Geophysical Survey System Inc. were carried out after casting concrete at 4, 7, 14, 28, 56, 90, 120 and 180 days. For the measurement of shallow cover depth, a GPR antenna with high centre frequency was adopted to obtain a high resolution of wave travel time measurement. As the velocity of EM wave is directly related to frequency, a 2GHz high centre frequency antenna provides a high-resolution measurement of wave travel time for shallow cover's depth reinforcement in radargram. Its shorter wavelength of propagated wave ensures a smaller near-field zone compared to other low-frequency GPR in longer wavelength. On the specified day, each cover depth conducted 12 scans

resulting in a total of 1152 scans. 2D signal processing by commercial software, i.e. ReflexW, was processed.

5.2 Data processing and analysis

Standard signal processing, including direct current shift, standard dewow low-frequency filter, time-zero correction which reference to the ground and removal of signal gain of the background and equipment, were conducted to adjust the waveform. There are two major parameters to estimate the cover depth of rebars in concrete by GPR. The first is GPR wave velocity as a function of dielectric permittivity at high frequency (e.g. GHz) where dispersion is relatively significant. Trilateration models with hyperbolic fitting (changed during hydration) were performed by an in-house program in LabVIEW to measure the velocity (Sham and Lai, 2016), as discussed in section 2.4. Ray-path modelling of the semi-trilateration method based on Pythagoras theorem with a common offset distance of transmitter and receiver which is shielded in the container as depicted in Chapter 4 was adopted. Frequency measurement based on the Wavelet Transform for time and frequency analysis was conducted in an in-house LabVIEW program (Lai et al., 2014) to estimate the GPR wavelength at which the reflection of rebar is detected, which affected the changes of near-/far-field phenomena as described in section 2.1.7.

The second is the Two-Way Travel Time (TWTT) and velocities were measured and calculated by using a point of inflection from each reflected A-scan for each corresponding hyperbola of rebars. TWTT at the apex of hyperbolas (changed during hydration) were extracted from the radargrams and conducted by the developed program in the in-house LabVIEW program. With the two measured parameters (wave velocity and TWTT), cover depths (20 - 70mm) of the rebars can be measured and compared with the actual values, so that the effects of hydration on cover depth estimation can be evaluated.

5.2.1 Algorithms for velocity estimation

Semi-trilateration equation and full-trilateration with known object depth were applied which are the ones explained in Chapter 2.

5.2.2 Wavelet transforms

The final WT 2D spectrogram was plotted by stacking all frequency spectrum with respect to time and was developed in-house LabVIEW program as shown in Figure 5.2.2-1. The frequency of the area of interest at a specified time (ns) can be obtained in this 2D spectrogram (W. W. L. Lai et al., 2014).

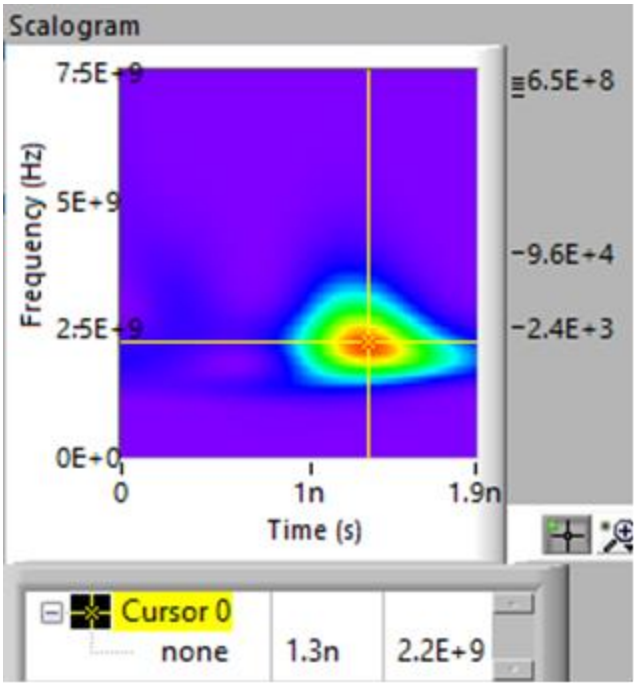

Figure 5.2.2-1 Wavelet Transform (WT) in in-house LabVIEW program

5.3 Findings

5.3.1 Changes of permittivity over increasing age of concrete

According to the estimated velocity and time calculated by the semi-trilaterated algorithm, two phenomena are noticed with the increasing age of concrete (i.e. hydration) as the following. First, the estimated velocity of the reflected GPR wave of the rebar is higher due to the flatter diffractive hyperbolas as indicated by the arrow in Figure 5.3.1-1. Then with the velocity, relative permittivity (dielectric constant) can be obtained by using equation (2.1.6.4-1) and plotted in the graph as illustrated in the left axis of Figure 5.3.1-1. On the other hand, TWTT of the hyperbolic apex is reduced as shown in the second axis of Figure 5.3.1-2.

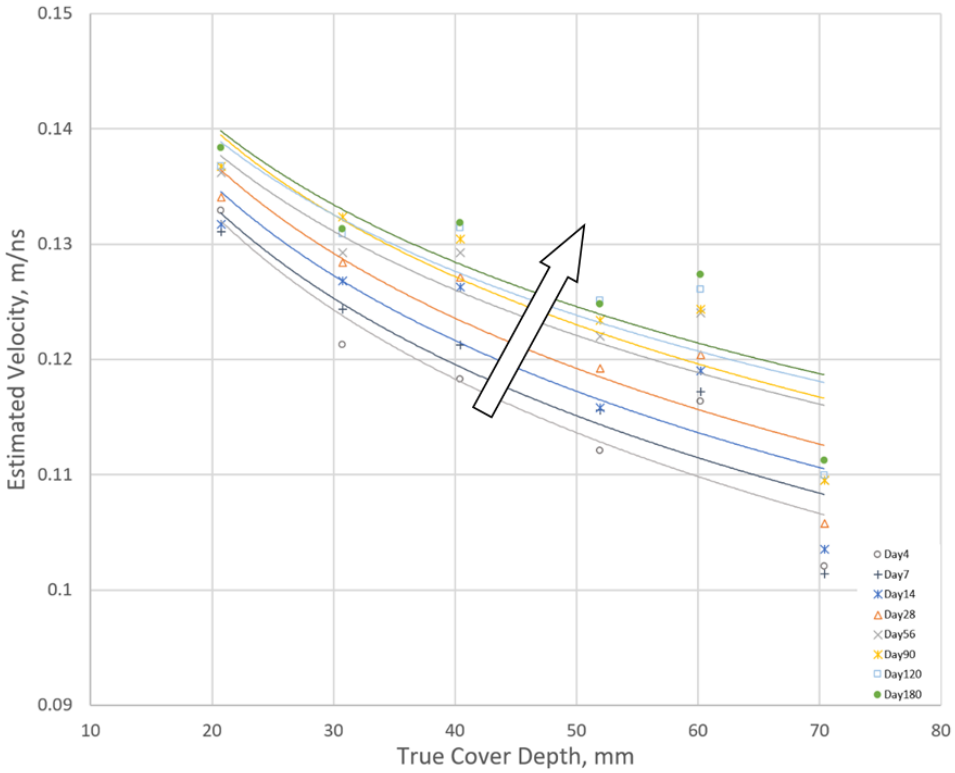

Figure 5.3.1-1 Change of estimated velocity of different cover depth at different ages of concrete

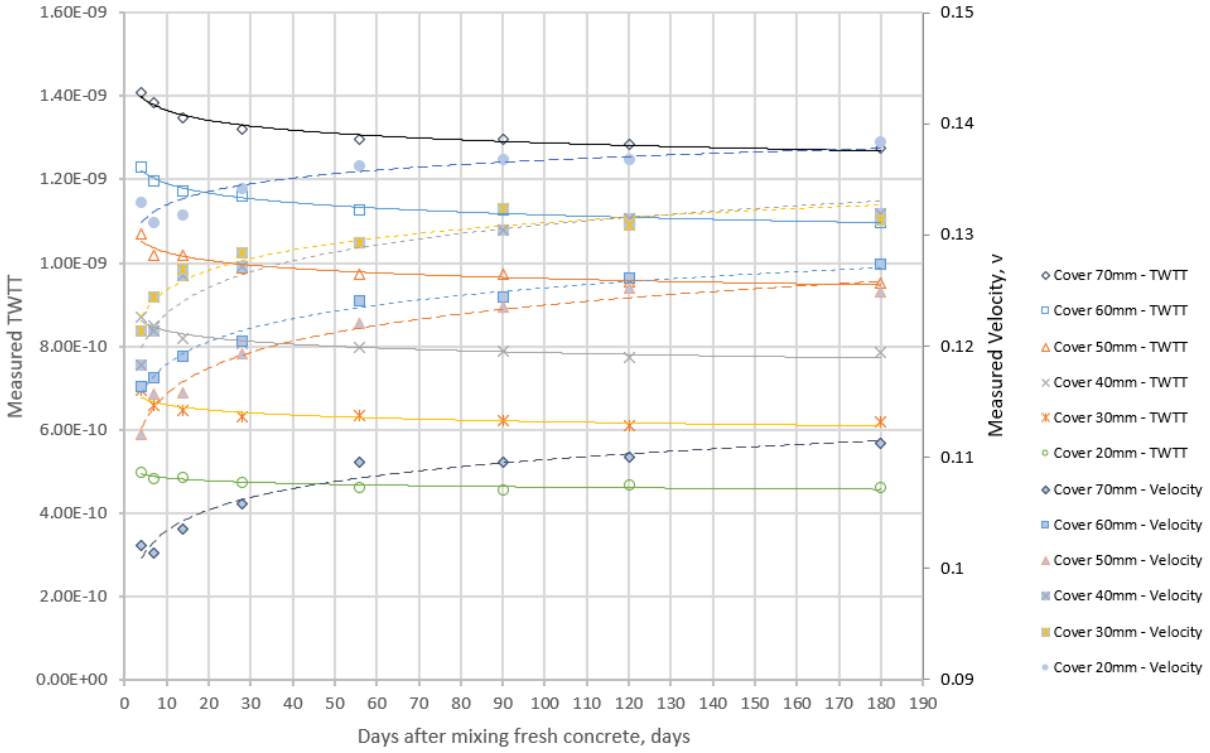

Figure 5.3.1-2 Change of measured time and calculated real permittivity of different cover depth at different ages of concrete

The result shows that the initial trend of marginal decrease of calculated relative permittivity was large at the early age of concrete and the decrease became steady at 90 days of aged concrete for all cover depths. The changes in the relative permittivity over different periods are associated with the hydration process since the free water is chemically bound and physically absorbed by the hydrated product, i.e. C-S-H. The result matches the understanding of the changes in the states of pore water from physically bounded to chemically bounded water during hydration. According to the estimated velocity shown in Figure 5.3.1-1, the corresponding relative estimated relative permittivity and estimated depth between different days for different cover depths over the ages of concrete is summarized in table 5.3.1-1. The result showed that after 56 days for cover depth of 20-70mm, the average percentage of changes of the relative permittivity is 1.3% with the maximum value of 4.6% and the associated variation of average estimated depth is 0.02mm with the maximum value of 1.1mm. While at an early age of 56 days for a cover depth of 20-70, the average percentage of changes of the relative permittivity is 3.2% with a maximum value of 7.8% and the associated variation of average estimated depth is 0.13mm with the maximum value of 7.8mm.

The result revealed that the variation of estimated cover depth because of the change of relative permittivity during Portland cement hydration at an early age to 56 days is more significant than that after 90 days.

% change of relative permittivity, $\Delta\varepsilon$							**Change of estimated depth, Δd (mm)**						
Day	True Cover Depth, mm						Day	True Cover Depth, mm					
$\Delta\varepsilon$	70.35	60.15	51.9	40.35	30.7	20.7	Δd	70.35	60.15	51.9	40.35	30.7	20.7
$(\varepsilon_7-\varepsilon_4)/\varepsilon_4$	1.3%	-1.4%	-6.0%	-4.7%	-4.8%	2.9%	d_7-d_4	-1.8	-1.4	-1.0	-0.1	2.4	-1.4
$(\varepsilon_{14}-\varepsilon_7)/\varepsilon_7$	-4.1%	-3.1%	-0.3%	-7.8%	-4.0%	-1.0%	$d_{14}-d_7$	-0.4	-0.4	0.1	0.3	-0.1	0.1
$(\varepsilon_{28}-\varepsilon_{14})/\varepsilon_{14}$	-4.2%	-2.2%	-5.6%	-1.3%	-2.5%	-3.5%	$d_{28}-d_{14}$	0.0	-3.8	0.1	-0.3	-0.5	-0.5
$(\varepsilon_{56}-\varepsilon_{28})/\varepsilon_{28}$	-6.7%	-5.8%	-4.5%	-3.2%	-1.4%	-3.1%	$d_{56}-d_{28}$	1.2	3.9	0.4	0.1	0.3	-0.3
$(\varepsilon_{90}-\varepsilon_{56})/\varepsilon_{56}$	0.0%	-0.5%	-2.3%	-1.9%	-4.6%	-0.8%	$d_{90}-d_{56}$	0.0	0.2	0.7	-0.1	0.2	-0.2
$(\varepsilon_{120}-\varepsilon_{90})/\varepsilon_{90}$	-0.8%	-2.8%	-2.7%	-1.4%	2.2%	0.1%	$d_{120}-d_{90}$	-0.4	-0.4	-0.3	-0.5	-1.1	0.7
$(\varepsilon_{180}-\varepsilon_{120})/\varepsilon_{5120}$	-2.3%	-2.0%	0.5%	-0.7%	-0.7%	-2.3%	$d_{180}-d_{120}$	0.4	0.1	-0.3	0.8	0.7	-0.1

Table 5.3.1-1 % Change of relative permittivity and corresponding change of estimated depth for different cover depths at different ages of concrete

5.3.2 Estimated cover depths over age of concrete

According to the estimated depths calculated by the semi-trilateration algorithm, the estimated cover depths of the rebars by the reflected GPR wave fluctuated at the early age of concrete and became steady at and after 90 days of the age of concrete as shown in Figure 5.3.2-1. At the early age of the concrete, i.e. Day 4 and 7, the estimated cover depths for cover depth 20-70mm were unstable and inconsistent in order. Between Day 14 to 28, almost all results showed a tendency for

a decrease in estimated depths. The variation of estimated cover depths tends to be steady at Day 90 and afterwards, and as mentioned in section 5.3.1, the variation of average estimated cover depths is 0.02mm which is insignificant.

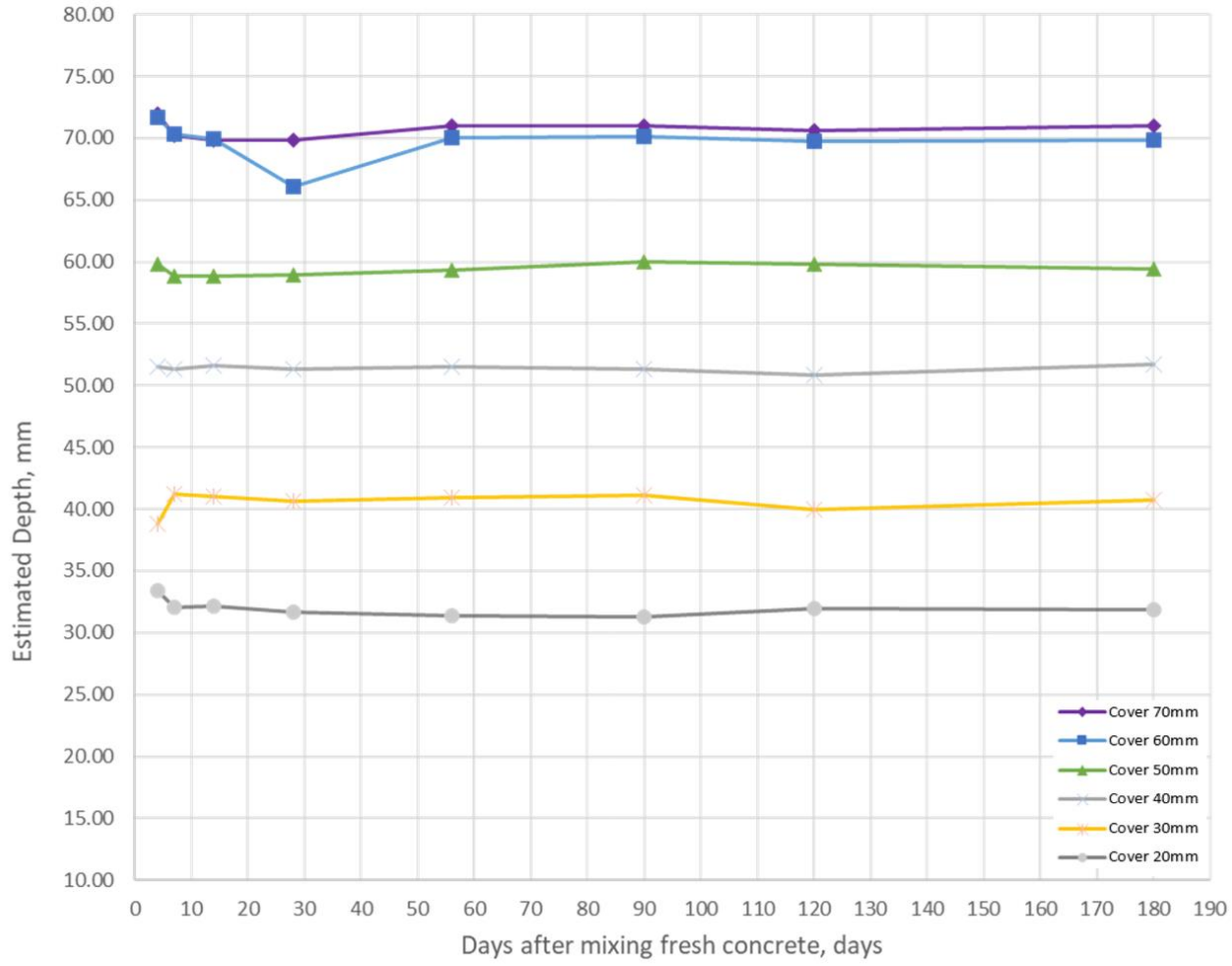

Figure 5.3.2-1 Estimated depths change due to changes in free water during hydration over different age of concrete

The result revealed that the higher estimated depths at Day 4 are because of much of the free water freely formed which is not hydrated with Portland cement and the amount of free water varies for each cover depth. This result matched with the frequency response and relative permittivity that the low-frequency response obtained in WT and the high value of relative permittivity calculated respectively due to much content of free water inside concrete. Between 14 to 28 days, as depicted in section 5.3.3 about frequency response due to free water consumed during the hydration process, the relative permittivity and the estimated depths decreased. At Day 90 and beyond, the estimated depths for all cover depths of rebar remained steady which is associated with the frequency response and change in relative permittivity as much of the free water turned to bound water and

remained free water in capillary will continue to react with Portland cement during hydration process.

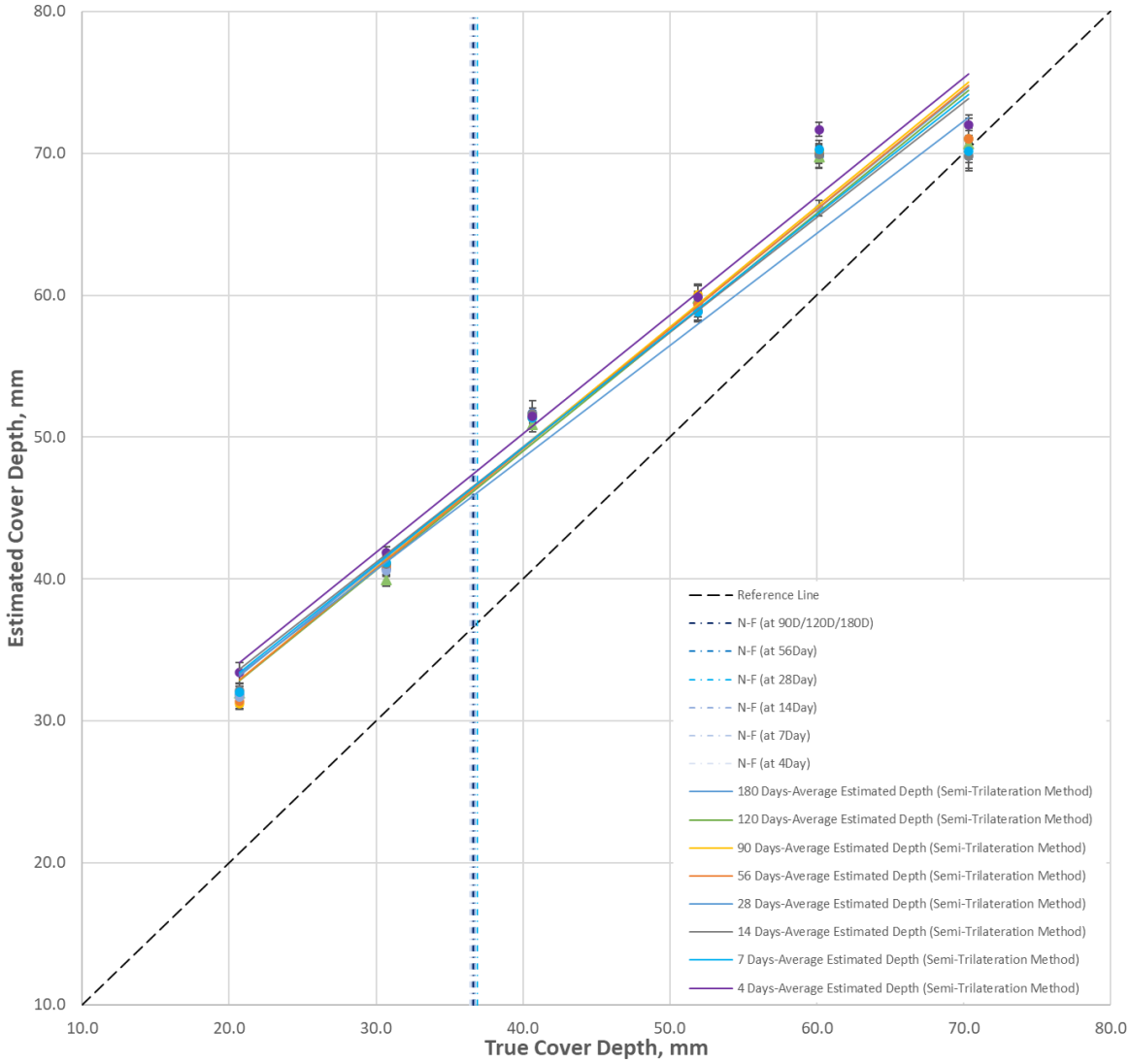

Figure 5.3.2-2 Estimated cover depths change due to changes of free water during hydration over different age of concrete vs true cover depths

According to the result shown in Figure 5.3.2-2, the results showed that all cover depths were overestimated compared to the true cover depths indicated as reference line (dotted) and all estimated cover depths at the early age of concrete were highly overestimated, i.e. cover depths estimated at Day 4 were the highest overestimated. The over-estimation of cover depths for different days gradually decreased from Day 4 and further improved at Day 180, and the gradients were in order. The average variation of estimated cover depth for covers 20 to 70 between Day 4 and Day 180 was 0.44mm with a maximum of 1.9mm and the variation is insignificant. This result

revealed that much free water converted to bound water during hydration and little amount of free water trapped will continue to turn to bound water. Still, the effect on the travelling velocity and TWTT may not be significant. This result supplements the results of relative permittivity, frequency response and TWTT. As the cover thickness of cover depths of 50-70mm is thicker, the amount of free water trapped can continue to turn to bound water and hence the changes of estimated cover depth at 180 days are more compared with estimated cover depth of 120 days. Hence the near-field effect is much more significant at a cover depth of 20-40mm and less significant by the effect of hydration. While the hydration effect is much more significant than the near-field effect at a cover depth of 50-70mm.

5.3.3 Changes of frequency over the age of concrete

According to the measured peak frequency for different cover depths, i.e. 20-70mm cover depth, by WT, shown in Figure 5.3.3-1a, the peak frequency of the reflected GPR wave from the target object, i.e. rebar, was gradually increasing for the first 28 days after Portland cement mixing and tend to be steady at and after 56 days. The depth measurement also affected by the change of the frequency and velocity, as shown in 5.3.2-1.

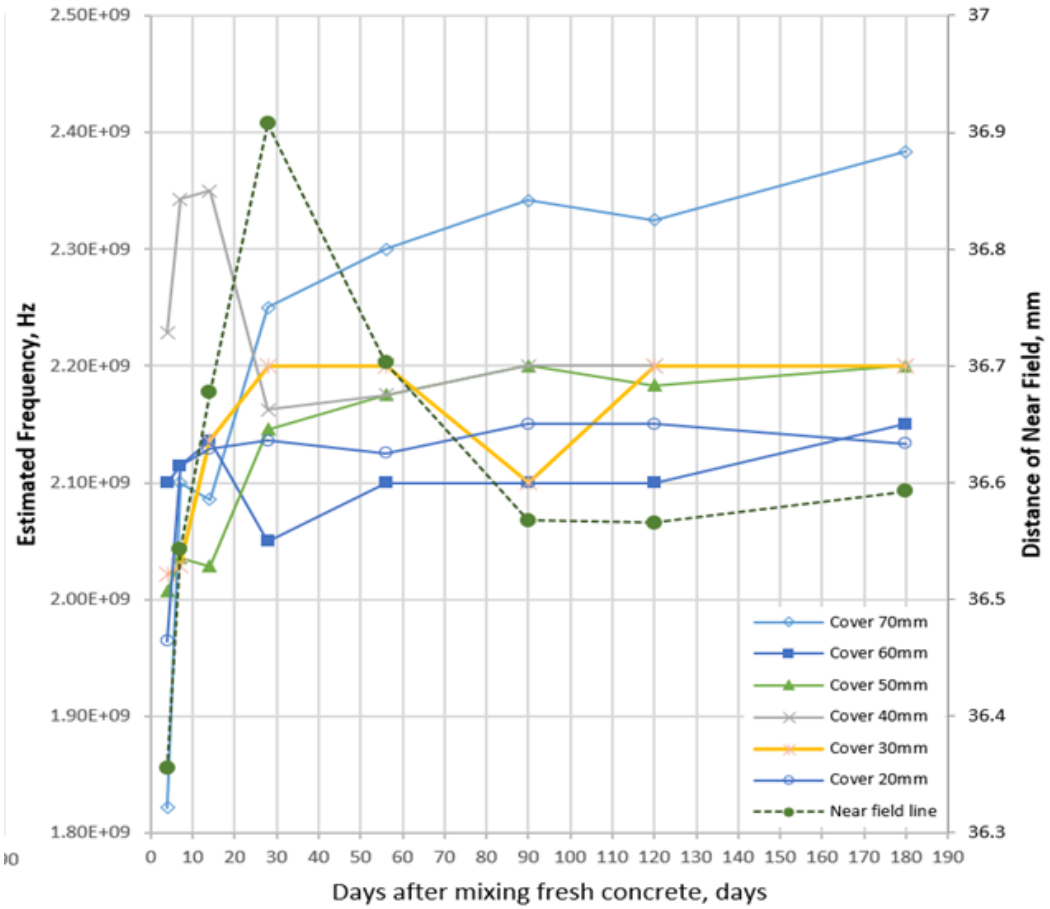

Figure 5.3.3-1a Change of peak frequency of different cover depths and change of distance of Near Field for different ages of concrete

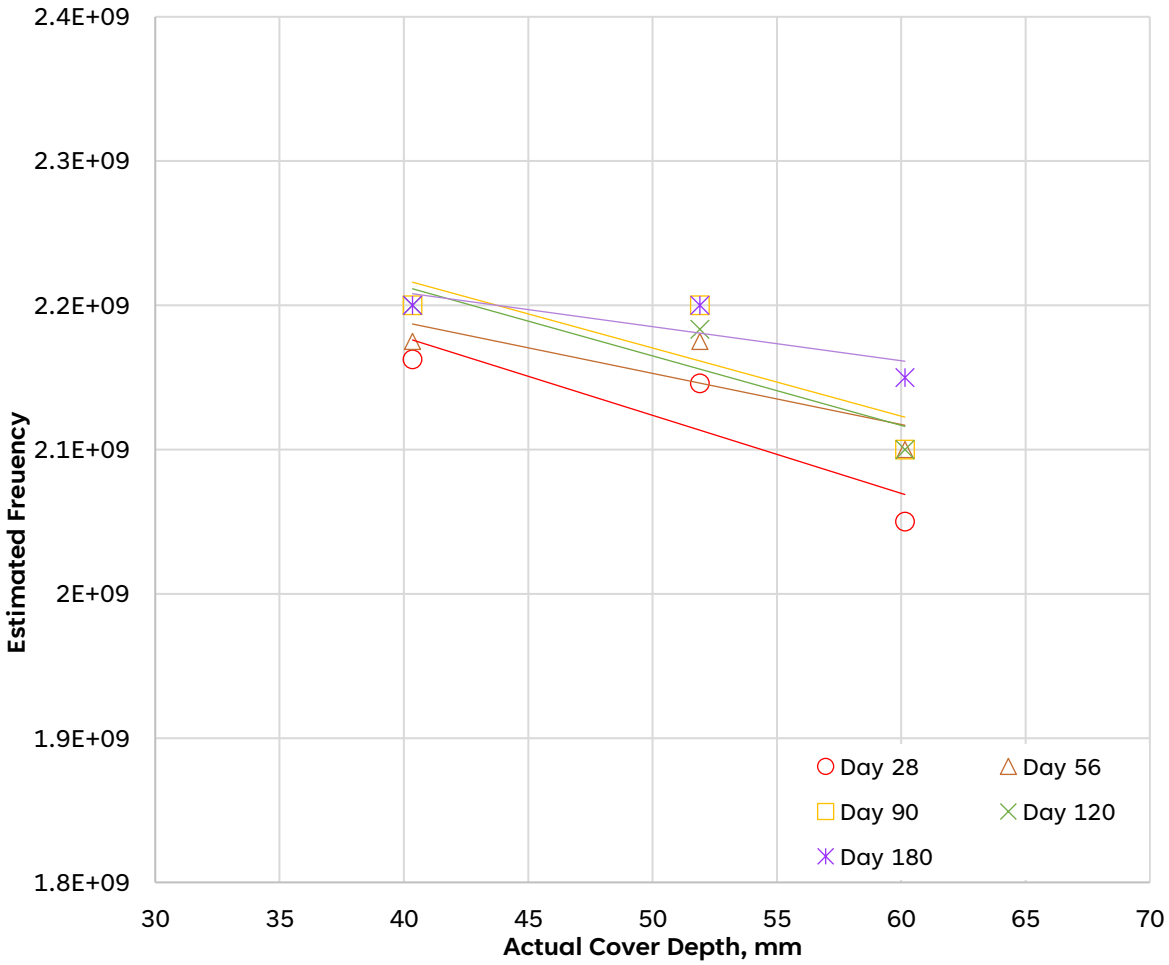

Figure 5.3.3-2b Change of peak frequency of different cover depths for different concrete ages

According to the estimated frequency for cover depth from 40mm to 60mm illustrated in Figure 5.3.3-1b, the frequency responses gradually increased with an increase in concrete age. The variation of frequency responses occurred at the cover depth of 60mm and became steady at the cover depth of 40mm.

The increase in peak frequency over the ages is due to the absorption and relaxation of different frequencies. The result matches the understanding of the Portland cement hydration process and relaxation of molecules explained by Debye's model and Cole and Cole's model as mentioned in the previous section. At the early age of concrete, the majority of the free-form water molecules are not hydrated with Portland cement. The free form of water contributed significantly to the imaginary part of the relative permittivity which absorbs the energy of a high-frequency portion of the GPR wave and results in obtaining low-frequency response, i.e. case 1 of Figure 5.3.3-2. On Day 7 of concrete, free water was consumed during the hydration process and converted as bound

water with the hydrated product which also restricted polarization. This causes the shifting of the imagery part to a lower frequency at the middle range of the frequency spectrum and results in higher peak frequency and wider bandwidth in frequency response, i.e. case 2. Age of concrete at 90 days, the hydration process will continue to turn the remaining free water in the capillary to bound water and further shift the imagery part to the low frequency that yields a steady increase in peak frequency in the frequency spectrum, i.e. case 3. According to Figure 5.3.3-3, the result showed the frequency spectrum with respect to time over the ages of concrete for a concrete cover depth of 50mm. The peak frequencies at the early age of concrete were lower and gradually increased, and the TWTTs were larger in value and gradually decreased over the ages of concrete. This result matches the above model, explaining the changes in peak frequency due to the shift of the imaginary part of real permittivity, which results in shorter TWTT due to less water content. Hence, the shallower the cover depth, i.e. cover depth of 40mm, the less the free water remained as it turned to bound water and the response frequency would be steady. While much free water remained for cover depth over 40mm and the response frequency varies with the ages of concrete.

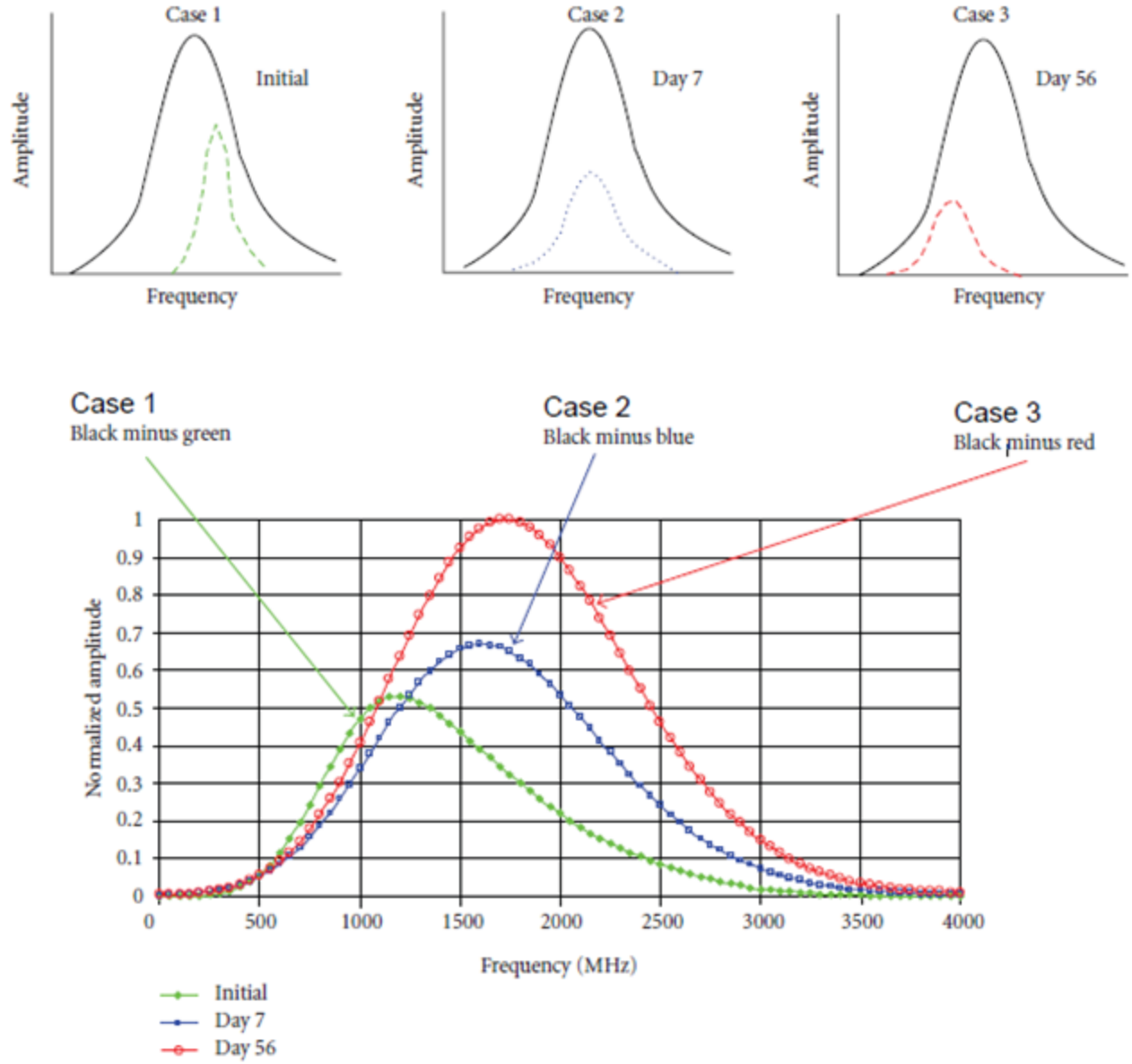

Figure 5.3.3-3 The frequency spectrum changes due to the change of free water during hydration (Lai and Wiggenhauser, 2010). Case 1: All water is in free form. Case 2: Water is hydrated and bounded; free water remains and absorbed in capillary. Case 3: More water is hydrated and bounded, but smaller amount of free water still exists in the capillary.

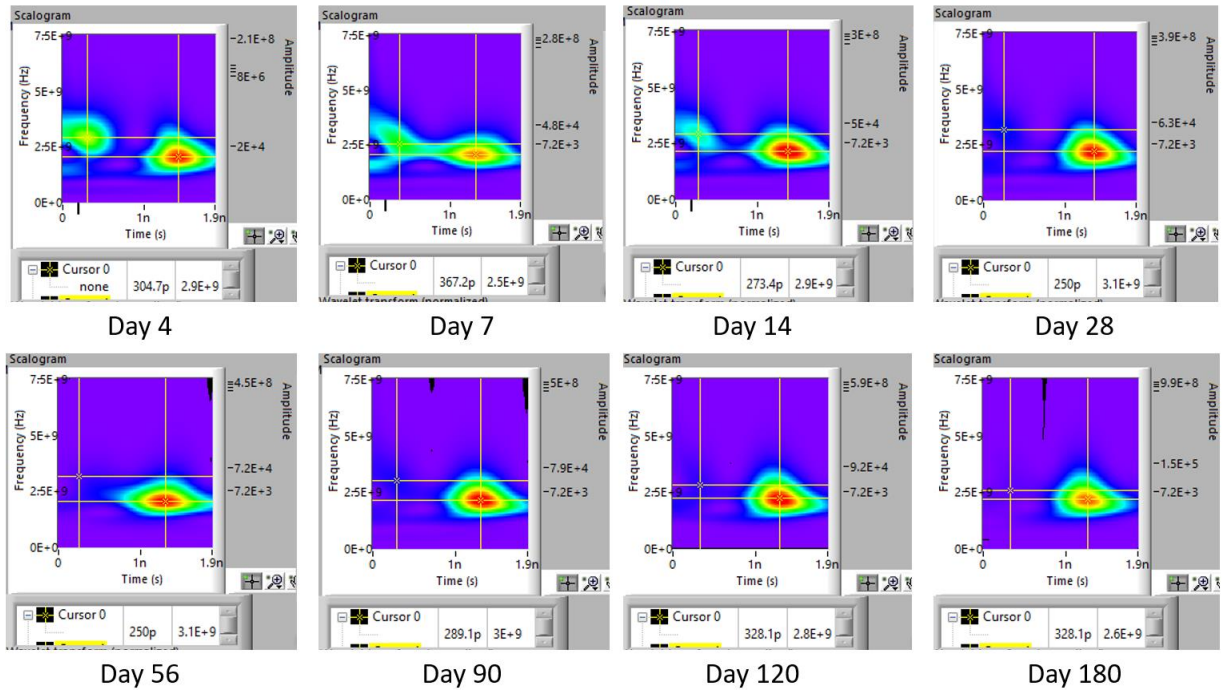

Figure 5.3.3-4 Changes of f*requency spectrum* with respect to time over the ages of concrete of cover depth 50mm

5.4 Summary

To summarize:

This chapter provides explanation and recommendations in three aspects as below,

1. this chapter illustrates the relationship between the change in the water system and the formation of the macro and microstructure pores of the hydrated product during the hydration process of Portland cement. The mechanism of converting free water to physically absorbed water and chemically bounded water has been explained through the study of the changes in velocities and relative permittivity for different cover depths at different ages of concrete,
2. this chapter studies the signal received and analysed by using the Wavelet Transform (WT) method and explains the frequency responses due to the conversion of free water to bound water, absorption and relaxation of remaining free water during the hydration process, and
3. this chapter supplements the accuracies of cover depth measurements with the effect of ages of concrete in Chapter 5. The result of the abovementioned studies on the changes of relative permittivity and frequency responses matches the well-known Portland cement hydration process and co-relating the two attributes which provides a good

recommendation on the accuracies of depth measurement for different cover depths and at different ages of concrete.

The method can be further extended to study hydration mechanisms of different concretes with different compositions of concrete mix nondestructively such as changes of W/C and adding of admixtures.

6 Corrected Trilateration Ray-path model using a linear regression algorithm

6.1 The Semi-Trilateration and Full-Trilateration ray-path model

The semi-trilateration model and full-trilateration model reviewed in section 2.4.3 and 2.4.4 considered the separation distance between the antenna transmitter and receiver, and the radius of the cylindrical objects which are the often-ignored factors in depth estimation. However, the accuracy of the semi-trilateration and full-trilateration models to estimate objects of shallow cover depth and in near-field zones is questionable. In section 4.4.2, Semi-Trilateration and Full-Trilateration models overestimated the actual cover by 12.2-9.7mm (136.1-34.5%) and 17.5-14.1mm (153.6-46.1%), respectively. This over-estimation was greatly improved for cover depths from 40mm to 80mm by 10.6-0.5mm (28.2-1.2%) (semi-trilateration model) and 14.3-3.5mm (35.2-5.0%) (full trilateration model) because the object locates in the far-field zone. For engineering applications on shallow object mapping like rebar correction is required.

The purpose of this chapter is to develop a new correction algorithm based on a linear regression model and the use of root mean square error to measure the accuracy. The developed algorithm was applied to correct the estimated depth and, hence, to address the simultaneous errors due to GPR wave travel velocity and the two-way travel time. Secondly, three sets of validation experiments in a laboratory and in a real physical environment in Hong Kong are performed. Finally, the results of these experiments are analysed and discussed, and followed by a summary.

6.2 Linear regression correction with accuracy for depth estimation

As depicted in Chapter 4, the result of estimated average cover depth by using the Semi-Trilaterated Method and Full-Trilaterated Method was found, and the dataset was plotted as a graph of estimated average cover depth against true cover depth by the Semi-Trilaterated Method and Full-Trilaterated Method. Based on the experimental results and the rather linear behaviour of the plots, two linear regression equations can be formed and written as below to correct the estimated cover depth,

In general,

$$d_{corrected} = \frac{d_{estimated} - C_1}{m_1} \tag{6.2-1}$$

For Semi-Trilaterated Method,

$$d_{corrected} = \frac{d_{estimated} - 22.265}{0.7278} \tag{6.2-2}$$

For Full-Trilaterated Method,

$$d_{corrected} = \frac{d_{estimated} - 20.601}{0.8079} \tag{6.2-3}$$

where, $d_{estimated}$ is the estimated cover depth, and $d_{corrected}$ is the corrected cover depth.

For second iteration, the equation can be rewritten as below,

In general,

$$d_{corrected} = \frac{1}{m_1 m_2} d_{estimated} - \frac{1}{m_1 m_2} C_1 - \frac{1}{m_2} C_2 \tag{6.2-4}$$

For Semi-Trilaterated Method,

$$d_{corrected} = \frac{1}{0.7278 \times 0.9526} d_{estimated} - \frac{1}{0.7278 \times 0.9526}(22.265) - \frac{1}{0.9526}(2.24256) \tag{6.2-5}$$

For Full-Trilaterated Method,

$$d_{corrected} = \frac{1}{0.8079 \times 0.8394} d_{estimated} - \frac{1}{0.8079 \times 0.8394}(20.601) - \frac{1}{0.8394}(9.3522) \tag{6.2-6}$$

where, $d_{estimated}$ is the estimated cover depth, and $d_{corrected}$ is the corrected cover depth. The accuracy is determined by R-squared or called the coefficient of determination. It is calculated by using the following equation 6.2-7,

$$R^2 = 1 - \frac{SS_{residual}}{SS_{total}}$$

, where

$$SS_{residual} = \sum_i (y_i - f_i)^2 \tag{6.2-7}$$

$$SS_{total} = \sum_i (y_i - \bar{y})^2$$

y_i = Estimated value by ray-path model, i.e. semi-trilaterated model and full-trilaterated model

f_i = Predicted value, i.e. linear regression equation by semi-trilaterated model and full-trilaterated model

a) Predicted value by Linear regression equation of semi-trilateration model,

$$f_i = 0.7278x + 22.265$$

b) Predicted value by Linear regression equation of semi-trilateration model,

$$f_i = 0.8079x + 20.601$$

The R-squared values calculated by the Semi-trilateration Model and Full-trilaterated Model are 0.93 and 0.88 respectively. Both linear regression equations fit the data and the linear regression equation by the Semi-trilateration model is better compared with Full-trilateration Model.

6.3 Validation experiments in three sites

To evaluate the validity of the proposed algorithms by linear regression, experiments on three specimens were conducted.

6.3.1 Validation experiment 1 in LSGI concrete beams

Four reinforced concrete beams with dimensions 200mm (Width) x 800mm (Long) x 100 (Depth) were cast, as shown in Figures 6.3.1-1 to 6.3.1-3. Each of the concrete beams consisted of two 10mm rebars with a fixed separation of 300mm centre to centre between each rebar and rebars were placed from the end of the concrete beams to the centre of the rebar by 250mm. Both rebars were cast with the same cover depth. A similar rebar arrangement was applied to three other concrete beams. The only difference in each beam setup was the cover depth of two rebars, where the cover depth for the pairs of rebars was the same. Hence, each beam has two different cover depths and eight different cover depths of rebars from the concrete surface ranging from 10mm to 80mm were provided by four beams. A 2 GHz GPR GSSI palm antenna was used to conduct the GPR survey on the beams on six different days after the casting of the concrete beams, including day 28, 56, 90, 120, 180 and 420. 12 scans were carried out on each cover depth which consisted of two 10mm diameter rebars. Hence, a total of 1152 samples about the scanning on the rebars are collected. The typical radargrams of a 2GHz antenna are presented in Figure 6.3.1-4 with clear and strong reflections from the rebar. The cover depth estimation is based on the estimation of velocity which makes use of 20 to 50 points of the reflected hyperbolic footprint in the radargram.

By using the equation 2.1.6.4-1 and 2.4-3 as mentioned in Chapter 2, measured Two-way Travel time (TWTT) and estimated velocity, the estimated cover depth can be determined. Therefore, the estimated cover depth is based on the 40,320 data points from the reflected hyperbolic footprint in radargrams. The results of estimated depths by the ray-path model of the Semi-trilateration model, Full-trilaterated model, corrected Semi-trilaterated model and corrected Full-trilaterated model algorithm are listed in Table 6.3.1-1 and Table 6.3.1-2. The results of 10mm and 80mm cover depth are excluded in the table due to the interference of direct wave and the reflected wave of rebar, and that of the reflected wave of rebar and the underneath concrete beam surface respectively. In Table 6.3.1-1, the analysis is based on a Semi-trilateration model and the estimated travel time is measured between the positive peak of the direct wave and the reflected wave. While, in table 6.3.1-2, the analysis included the Semi-trilateration model and Full-trilateration model, and the estimated travel time is measured between the inflection point of the direct wave and the peak of the reflected wave.

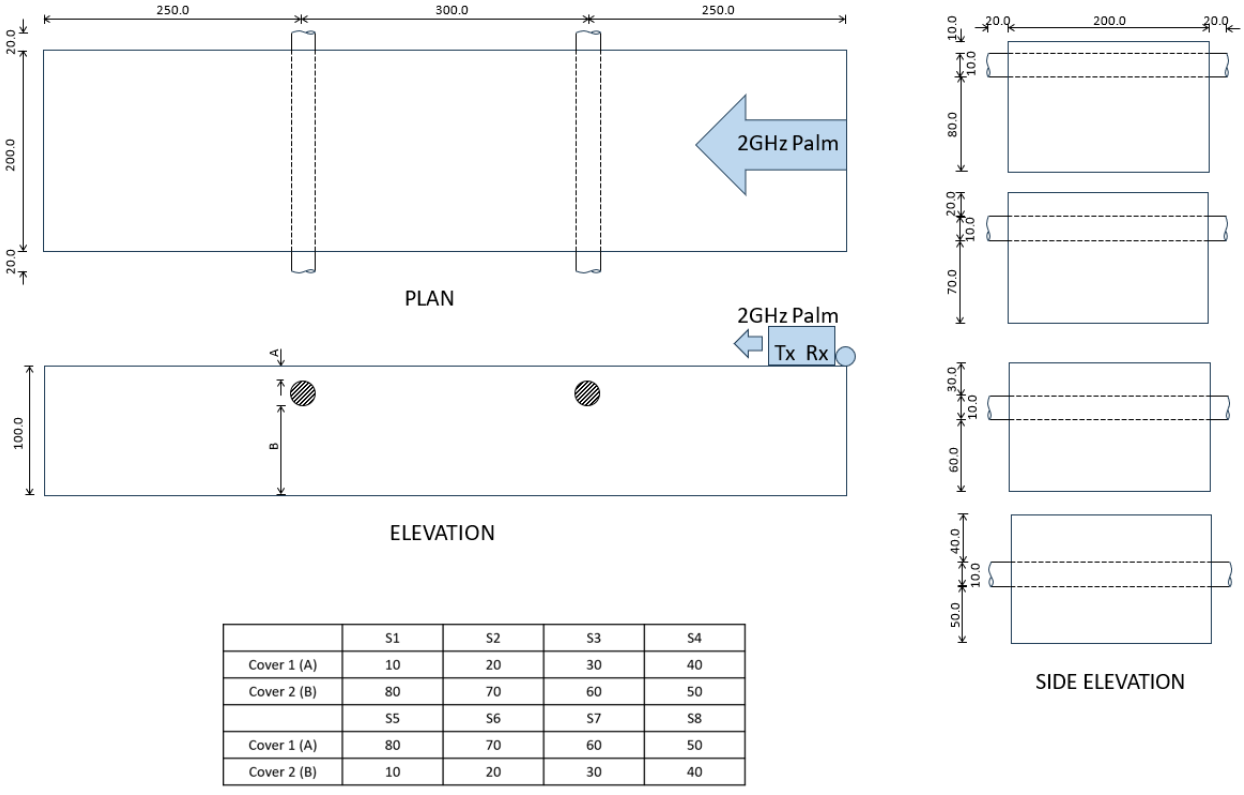

	S1	S2	S3	S4
Cover 1 (A)	10	20	30	40
Cover 2 (B)	80	70	60	50
	S5	S6	S7	S8
Cover 1 (A)	80	70	60	50
Cover 2 (B)	10	20	30	40

Figure 6.3.1-1 LGSI concrete beams for validation

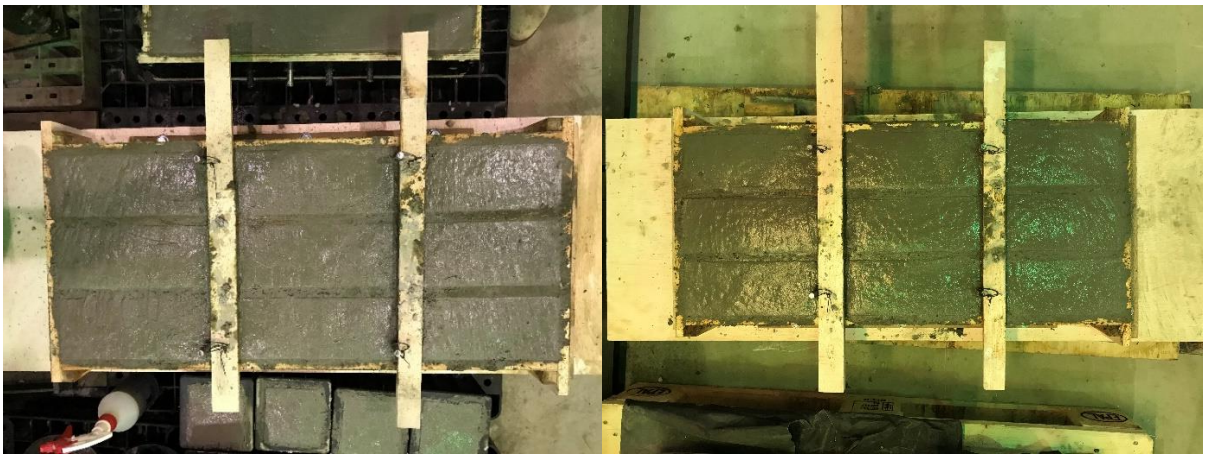

Figure 6.3.1-2 Casting of LGSI concrete beams

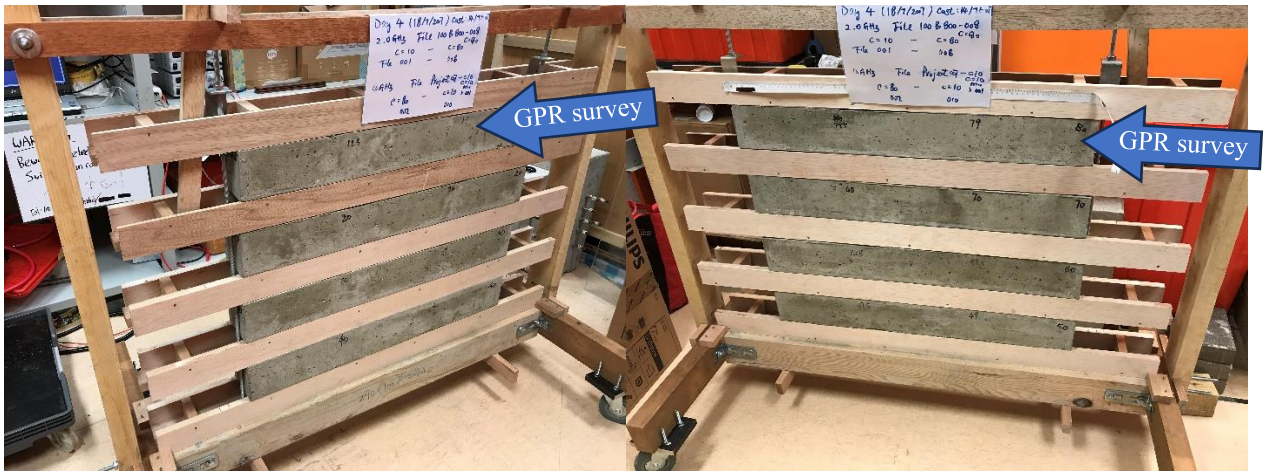

Figure 6.3.1-3 GPR test survey on the casted LGSI concrete beams with 10mm diameter rebars

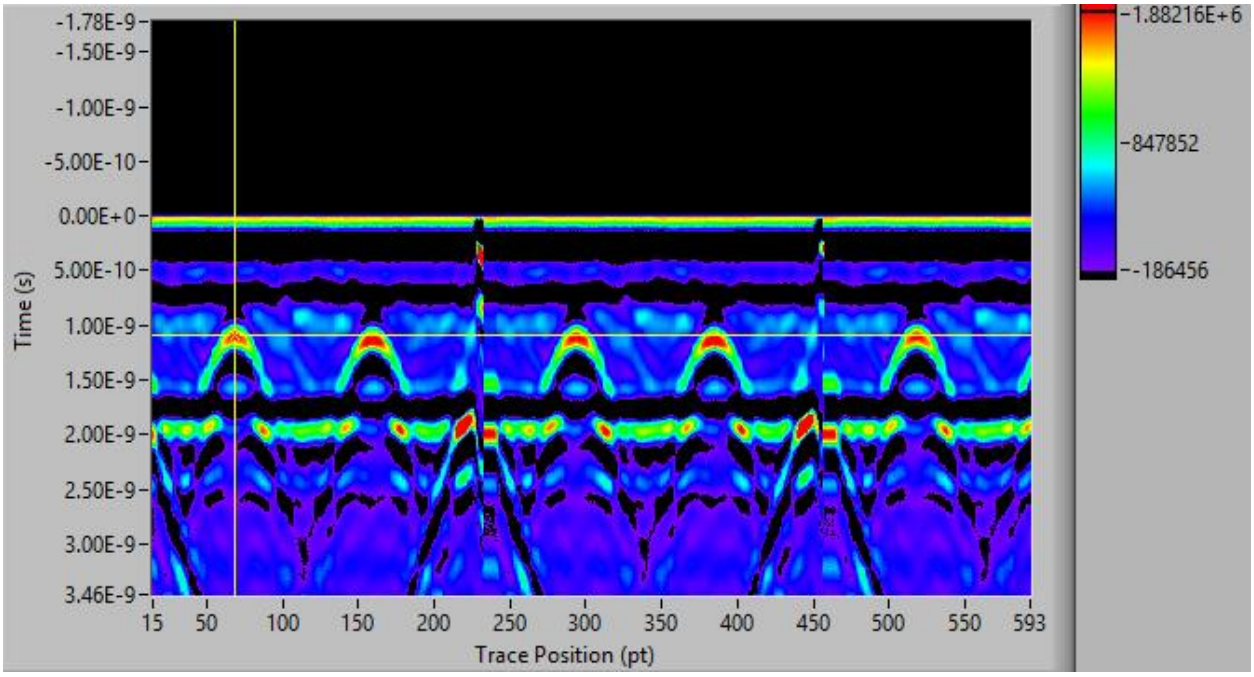

Figure 6.3.1-4 Radargram of 2GHz GPR test survey on the casted LGSI concrete beams with diameter 10mm rebars (60mm cover depth)

		Before Correction						After Correction					
Case No	Actual cover depth (mm)	Semi-trilateration method (m)	Error	Error (%)	Full-trilateration method (m)	Error	Error (%)	Corrected Semi-trilateration Model	Error	Error (%)	Corrected Full-trilateration Model	Error	Error (%)
1	69.0	78.5	9.4	13.7				78.7	9.7	14.0			
2	61.0	75.6	14.6	23.9				74.6	13.6	22.3			
3	49.3	63.2	14.0	28.3				56.7	7.4	15.1			
4	40.5	49.9	9.4	23.2				37.5	-3.0	-7.4			
5	29.5	41.6	12.1	41.0				25.5	-4.0	-13.4			
6	20.0	36.0	16.0	79.8				17.4	-2.6	-13.1			

Table 6.3.1-1 Estimated depth by Semi-trilateration model and corrected Semi-trilateration model (based on the reference of Peak of Direct Wave (PK-DW) to Peak of Reflected Wave (PK-RW)

		Before Correction						After Correction					
Case No	Actual cover depth (mm)	Semi-trilateration method (m)	Error	Error (%)	Full-trilateration method (m)	Error	Error (%)	Corrected Semi-trilateration Model	Error	Error (%)	Corrected Full-trilateration Model	Error	Error (%)
7	69.0	77.6	8.6	12.5	80.0	11.0	15.9	77.5	8.5	12.3	76.4	7.4	10.7
8	61.0	74.8	13.8	22.6	77.1	16.1	26.4	73.3	12.3	20.2	72.1	11.1	18.2
9	49.3	64.3	15.1	30.6	67.0	17.7	35.9	58.3	9.0	18.3	57.2	8.0	16.2
10	40.5	50.2	9.7	23.8	53.5	13.0	32.1	37.9	-2.6	-6.5	37.4	-3.1	-7.7
11	29.5	41.4	11.9	40.2	44.9	15.4	52.3	25.2	-4.3	-14.7	24.7	-4.8	-16.3
12	20.0	35.7	15.7	78.3	39.9	19.9	99.5	17.0	-3.0	-15.2	17.3	-2.7	-13.4

Table 6.3.1-2 Estimated depth by Semi-trilateration model, Full-trilateration model, corrected Semi-trilateration model and corrected Full-trilateration model algorithm (based on the reference of Inflection Point of Direct Wave (IP-DW) to Peak of Reflected Wave (PK-RW)

6.3.2 Validation experiment 2 in CEE concrete wall

A concrete wall with dimensions 2000mm (Height) x 1800mm (Long) x 200 (Thick) was cast, as shown in Figure 6.3.2-1. Two different layers of rebar formed by 20 mm diameter rebars and arranged vertically and horizontally to form mesh were cast into the wall. The centre-to-centre spacing of each rebar was 200mm. The concrete cover depth of the horizontal measured from the near face and the vertical rebar measured from the far face of the wall consisted of 50 & 60mm and 110 & 150mm respectively. Similarly, a 2 GHz GPR GSSI palm antenna was used to perform the GPR survey on the wall. 29 scans are carried out on the far face and near face of the wall which is composed of 14 scans in a horizontal traverse to scan 6 vertical rebars and 15 scans in a vertical traverse to scan 6 horizontal rebars. The typical radargrams of a 2GHz antenna are presented in Figure 6.3.2-2 with clear and strong reflections from the rebar. The results of estimated depths by the ray-path model of the Semi-trilateration model, Full-trilaterated model, corrected Semi-trilaterated model and corrected Full-trilaterated model algorithm are listed in Table 6.3.2-1. The analysis is measured between the inflection point of the direct wave and the peak of the reflected wave.

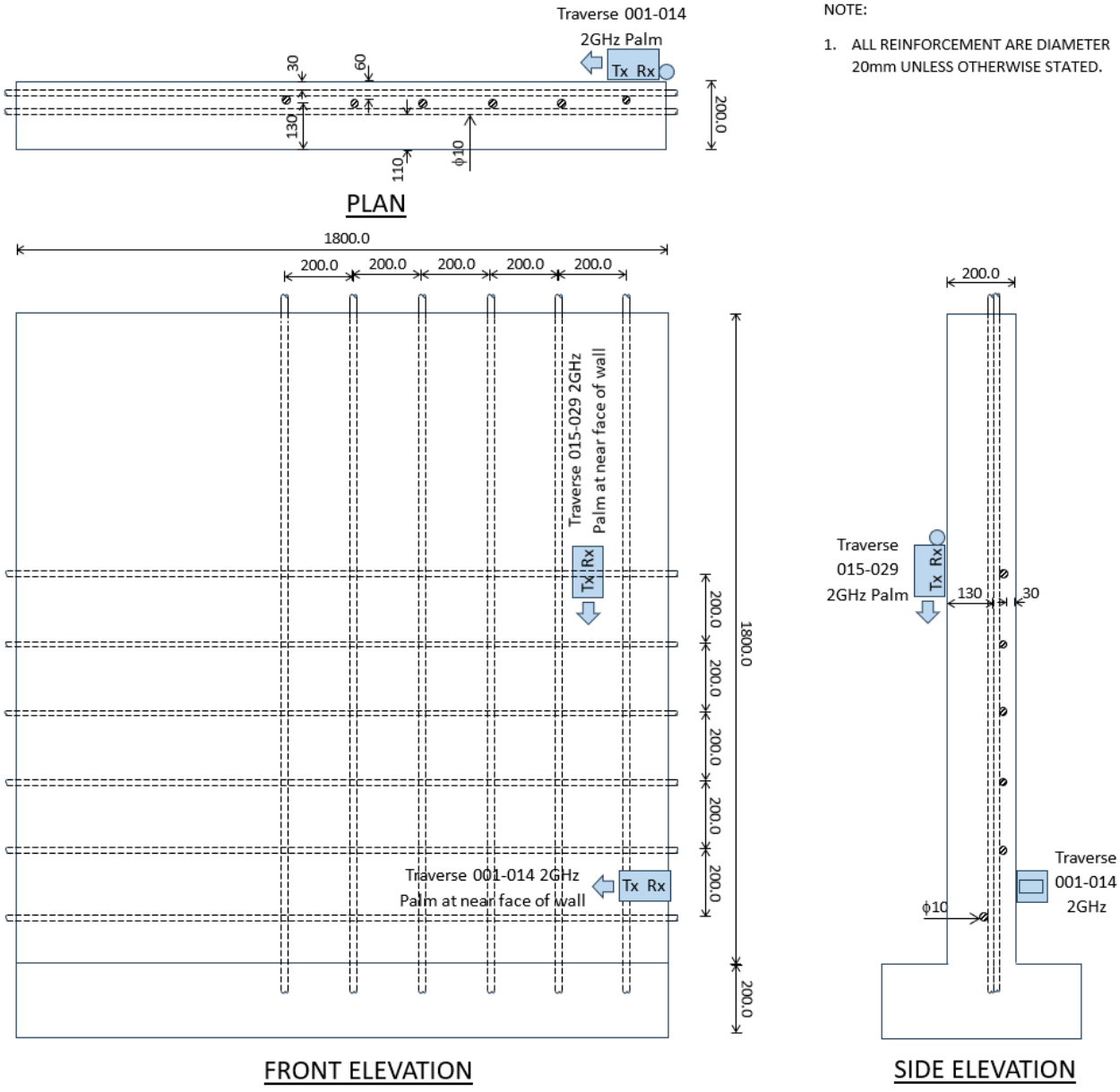

Figure 6.3.2-1 CEE concrete wall for validation

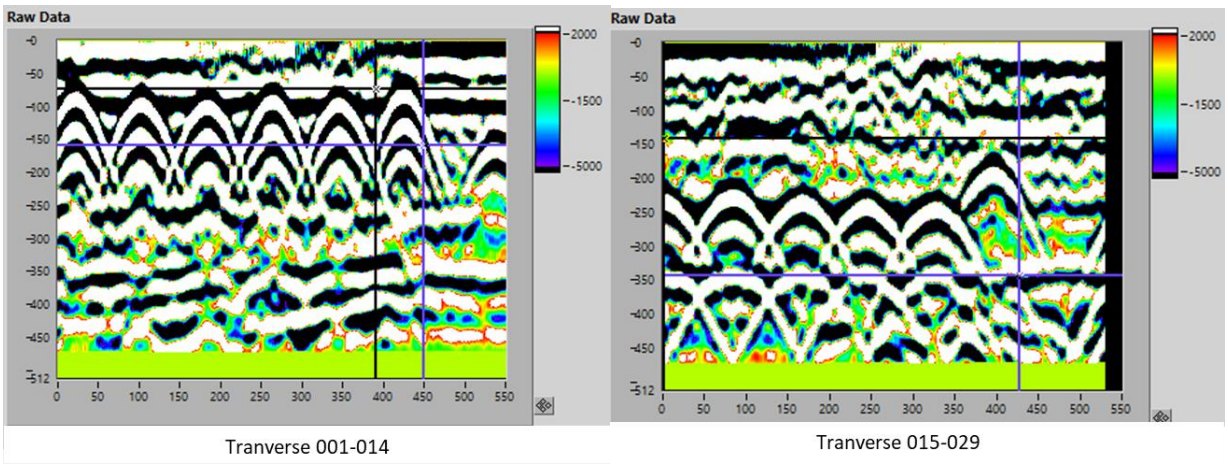

Figure 6.3.2-2 Radargram of 2GHz GPR test survey on the casted CEE concrete wall with diameter 20mm rebars

		Before Correction						After Correction					
Case No	Actual cover depth (mm)	Semi-trilateration method (mm)	Error	Error (%)	Full-trilateration method (mm)	Error	Error (%)	Corrected Semi-trilateration Model	Error	Error (%)	Corrected Full-trilateration Model	Error	Error (%)
13	50.0	60.9	10.9	21.7	64.4	14.4	28.8	53.3	3.3	6.7	53.4	3.4	6.9
14	60.0	69.0	9.0	15.0	72.3	12.3	20.5	65.1	5.1	8.4	65.1	5.1	8.4
15	110.0	105.4	-4.6	-4.2	107.4	-2.6	-2.4	117.6	7.6	6.9	116.9	6.9	6.2
16	150.0	138.8	-11.2	-7.5	140.8	-9.2	-6.1	165.7	15.7	10.4	166.1	16.1	10.7

Table 6.3.2-1 Estimated depth by Semi-trilaterated model, Full-trilaterated model, corrected Semi-trilateration model and corrected Full-trilateration model algorithm

6.3.3 Validation experiment 3 in BRE concrete beam

A test concrete beam was cast with 11 number of diameters 16mm rebars and the spacing of each rebar is fixed at 100mm. Each rebar has different cover depths, and the depths vary from 40, 60, 80, 100, 120, 140, 160, 180, 200, 220 and 240mm, as shown in Figure 6.3.3-1. The blue arrow indicates the 2GHz GPR palm antenna traverse direction in which the survey is travelled perpendicular to the alignment of the rebars. As the rebar cover depth increases, the hyperbolic reflection acquired also increases with depth. However, as shown in Figure 6.3.3-2, due to the resolution of the antenna and the fixed spacing between the rebars, the acquired hyperbolic reflections overlapped each other and the case became much worse at a cover depth of 180mm or more. The hyperbolic reflection of cover depth 180mm or more cannot be extracted. Also, as the GPR antenna travel distance at each end of the beam is insufficient, thus, there is only half of the

hyperbolic reflection obtained for cover depth of 40mm. The typical radargrams of 2GHz antenna is presented in Figure 6.3.3-3 with clear and strong reflections from the rebar.

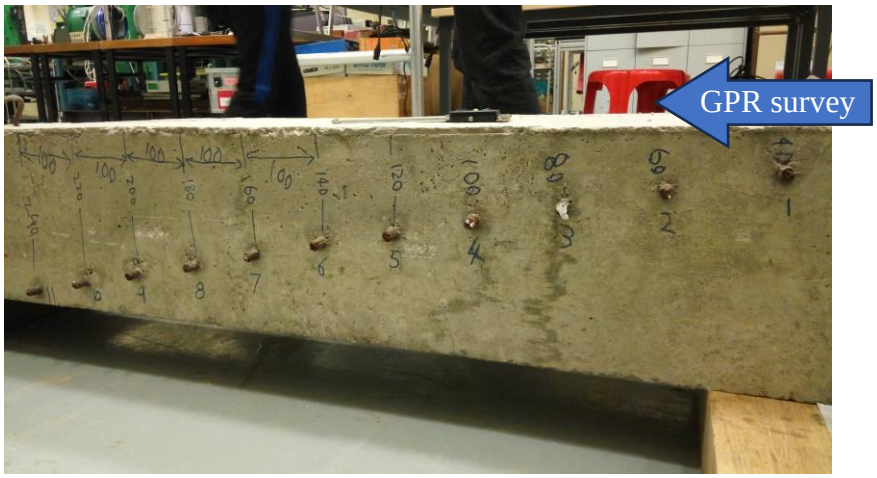

Figure 6.3.3-1 BRE concrete beam

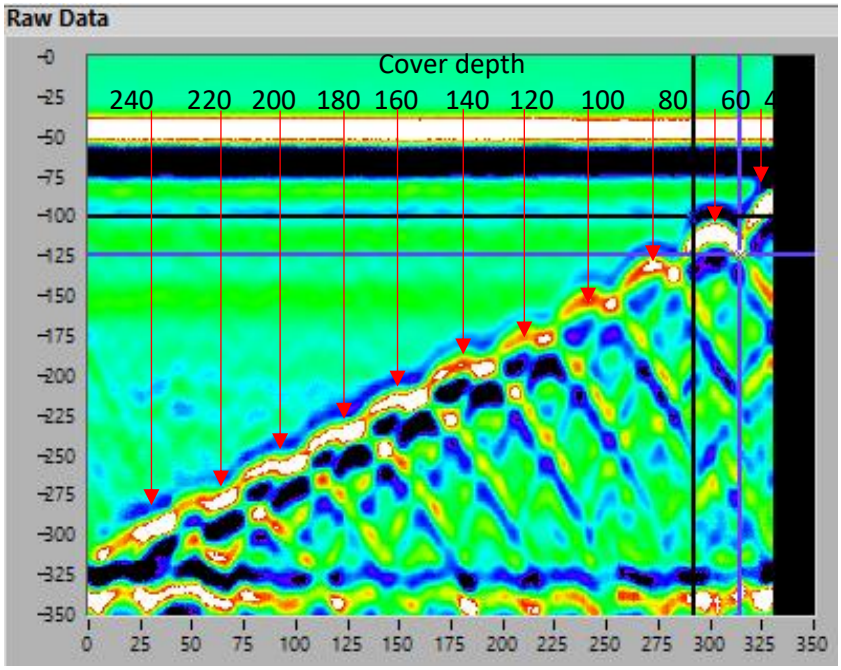

Figure 6.3.3-2 Radargram of BRE concrete beam

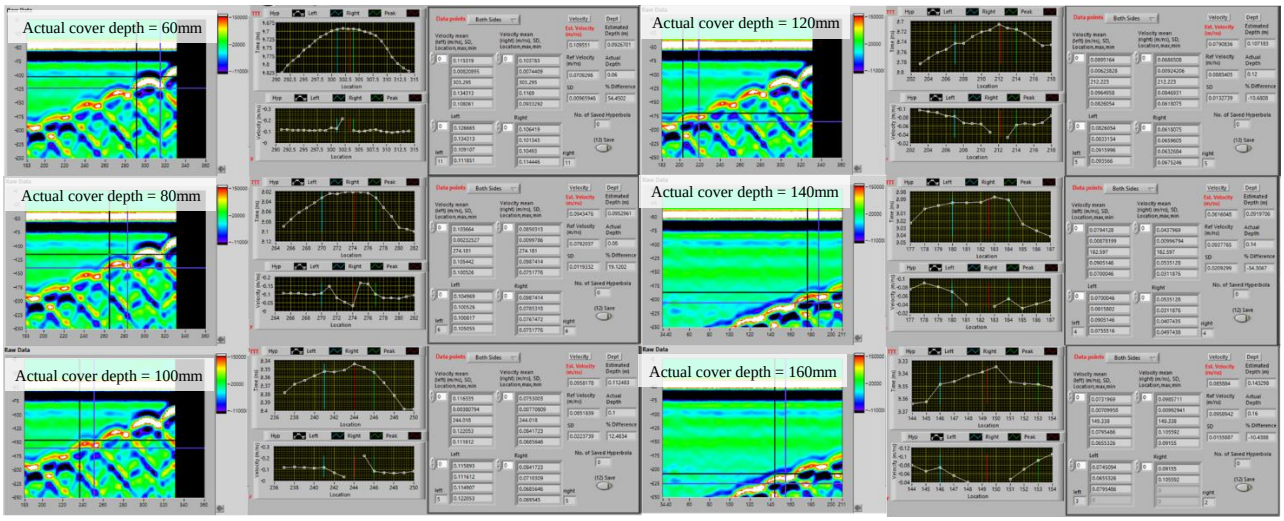

Figure 6.3.3-3 Radargram of 2GHz GPR test survey on the casted BRE concrete beams with diameter 16mm rebars

The results of estimated depths by the ray-path model of the Semi-trilateration model, Full-trilaterated model, corrected Semi-trilaterated model and corrected Full-trilaterated model algorithm are listed in Table 6.3.3-1.

		Before Correction						After Correction					
Case No	Actual cover depth (mm)	Semi-trilateration method (m)	Error	Error (%)	Full-trilateration method (m)	Error	Error (%)	Corrected Semi-trilateration Model	Error	Error (%)	Corrected Full-trilateration Model	Error	Error (%)
17	60.0	92.7	32.7	54.5	94.7	34.7	57.9	99.2	39.2	65.3	98.2	38.2	63.6
18	80.0	95.3	15.3	19.1	97.4	17.4	21.7	103.0	23.0	28.7	102.1	22.1	27.6
19	100.0	112.5	12.5	12.5	114.2	14.2	14.2	127.8	27.8	27.8	126.8	26.8	26.8
20	120.0	107.2	-12.8	-10.7	109.1	-10.9	-9.1	120.1	0.1	0.1	119.4	-0.6	-0.5
21	140.0	92.0	-48.0	-34.3	94.0	-46.0	-32.9	98.2	-41.8	-29.9	97.0	-43.0	-30.7
22	160.0	143.3	-16.7	-10.4	144.6	-15.4	-9.6	172.2	12.2	7.6	171.7	11.7	7.3

Table 6.3.3-1 Estimated depth by Semi-trilateration model, Full-trilateration model, corrected Semi-trilateration model and corrected Full-trilateration model algorithm

6.4 Findings and discussion

6.4.1 Findings and discussion – Estimated depths by of validation experiment 1 in LSGI concrete beams

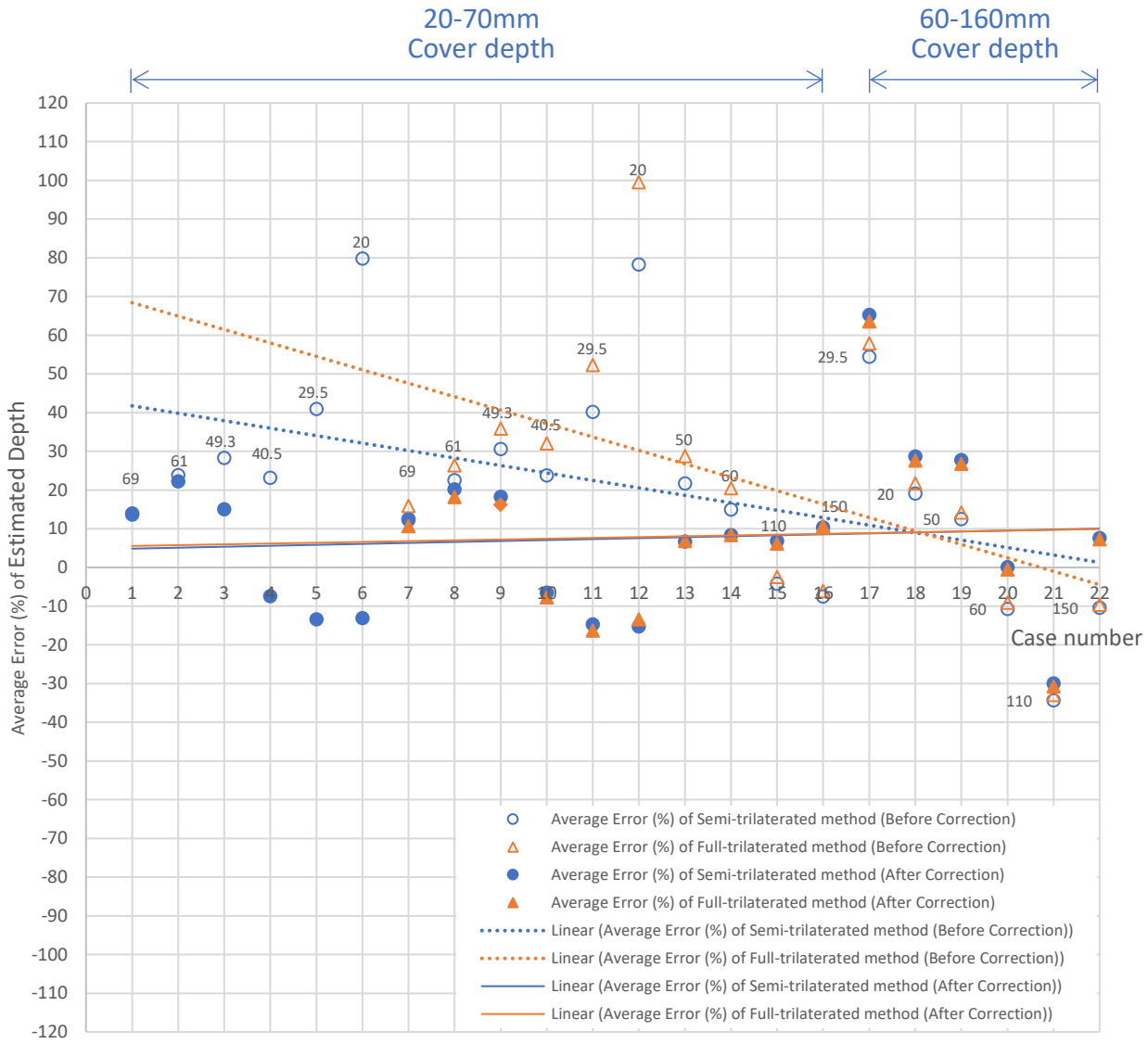

Figure 6.4.1-1 Comparison of error of cover depth estimation by Semi-trilaterated method, Full-trilaterated method, Corrected Semi-trilaterated method and Correct Full-trilaterated method (Note: the value above the data point in the graph is the actual cover depth)

For Case 1-6, the cover depth estimation is based on the Semi-trilateration method only and the measurement of two-way travel time ranges from the Positive Peak of the Direct Wave (PK-DW) and the Reflected Wave (PK-RW) of the target object. The result shows that the average percentage error of estimated cover depth 69mm to 20mm varies from 13.7% to 79.8%. After correction by linear regression, the average percentage error of estimated cover depth greatly improved from 14.0% to -13.1%. Referring to Figure 6.4.1-1, the significant improvement of the estimated result occurs at a cover depth ranging from 49.3mm to 20mm, i.e. Case 3-6.

For Case 7-12, the cover depth estimation is based on the Semi-trilateration method and Full-trilateration method. The measurement of two-way travel time ranges from the inflection point of the Direct Wave (IP-DW) and the peak of the Reflected Wave (PK-RW) of the target object. The result shows that the average percentage error of estimated cover depth 69mm to 20mm varies from 12.5% to 78.3% and 15.9% to 99.5% for the Semi-trilateration method and Full-trilateration method respectively. After correction by linear regression, the average percentage error of estimated cover depth significantly improved to 12.3% to -15.2% and 10.7% and -13.4%. Similarly, refer to Figure 6.4.1-1, the significant improvement of estimated result occurs at a cover depth ranging from 49.3mm to 20mm, i.e. Case 9-12. Refer to Case 10-12 about the cover depth of 40.5mm to 20mm, comparing the actual cover depth and estimated cover depth by the Corrected Semi-trilateration method, the error is ranging from 2.6mm to 4.3mm. The cover depth estimation by the Semi-trilateration method is slightly better than Full-trilateration method.

While refer to Table 6.3.1-1 and 6.3.1-2, comparing the estimated cover depth result based on reference point between PK-DW and IP-DW to the PK-RW by using the same method, i.e. Semi-trilateration method, the average percentage error of the estimated cover depth is 35.0 and 34.7 respectively. After correction, the average percentage error of the estimated cover depth is 2.9 and 2.4 respectively. By using the same method, i.e. Semi-trilateration method, the cover depth estimation by IP-DW as the reference point is slightly better than PK-DW as the reference point.

6.4.2 Findings and discussion of validation experiment 2 in CEE concrete wall

For Case 13-16, the cover depth estimation is based on the Semi-trilateration method and Full-trilateration method. The measurement of two-way travel time ranges from the inflection point of the Direct Wave (IP-DW) and the peak of the Reflected Wave (PK-RW) of the target object. The actual cover depth of the CEE concrete wall varies from 50 – 150mm. According to Table 6.3.2-1, the result shows that the average percentage error varies from 21.7% to -7.5% and from 28.8% to -6.1% for the Semi-trilateration method and the Full-trilateration method respectively. After correction by linear regression, the average percentage error is significantly improved ranging from 6.7% to 10.4% and 6.9% to 10.7% for the Semi-trilateration method and Full-trilateration method respectively.

6.4.3 Findings and discussion of validation experiment 3 in BRE concrete beam

For Case 17-22, the actual cover depth of the BRE concrete beam varies from 60 – 160mm. According to Table 6.3.3-1, the average percentage error ranges from 54.5% to -10.4% and from 57.9% to -9.6% for the Semi-trilateration method and Full-trilateration method respectively. After correction by linear regression, the average percentage error varies from 65.3% to 7.6% and 63.6% to 7.3% for the Semi-trilateration method and Full-trilateration method respectively. In view of the depth estimation for Case 17-19 and excluding Case 20-22, the result shows that the average percentage error of estimated depth by the Semi-trilateration method and Full-trilateration method before and after correction by linear regression method as mentioned in section 6.2 are not improved.

Refer to Figure 6.4.1-1, for Case 17-22 with an actual cover depth of 60-160mm, the average percentage error fluctuates and the errors are significant at cover depths of 60mm and 140mm. The reason behind of the fluctuated average percentage error is in twofold: 1) the obtained radargrams for the rebars are partially overlapping each other. According to the radargram result, one-third to half of the reflected hyperbolic footprint of one rebar at the deeper location is being overlapped by another reflected hyperbolic footprint of other rebars at the shallow location. This situation becomes worse at deeper rebar, especially in cover depths of 120-160mm as shown in Figure 6.3.3-3. Hence, the data analysis cannot be performed for an actual cover depth of 180-240mm. The reason behind this is the separation spacing between each rebar is insufficient. With the cover depth increase, the overlapping of the hyperbolic footprint will be more and more. In real-life construction projects, the rebar arrangement always happens at different cover depths and multiple layers of longitudinal and transverse direction in congested environments which cannot be avoided during a GPR survey. 2) The spatial resolution setting in the configuration of the GPR survey is low, i.e. the scan per meter, and the scant scattered data is not adequate to form a complete and smooth hyperbolic footprint from the reflected data in radargram. This interfered with the analysis of the reflected hyperbolic footprint and caused the error of velocity estimation. The effect is significant in Case 21 and 22, i.e. cover depths 140mm and 160mm, as shown in Figure 6.3.3-3. Also, the reason behind this is that the GPR survey is targeted at tiny objects size of a diameter of 16mm rebar which is located far away from the concrete surface. As a result, the combination of the aforementioned effects lead to a significant error in the estimated cover depth.

6.4.4 Findings and discussion of estimated depth by Semi-Trilaterated method and Full-Trilateration method before and after correction

The estimated depth by the Semi-Trilateration method and Full-Trilateration method before and after correction by linear regression are plotted against the actual cover depth in Figure 6.4.4-1 and 6.4.4-2 with a diagonal reference line (presented in red dash line) where the estimated cover depth equals to the actual cover depths. The accuracy of the estimated cover depth can be represented by the degree of dispersion of the scattering data points relative to the reference line as shown in Figure 6.4.4-1 and 6.4.4-2.

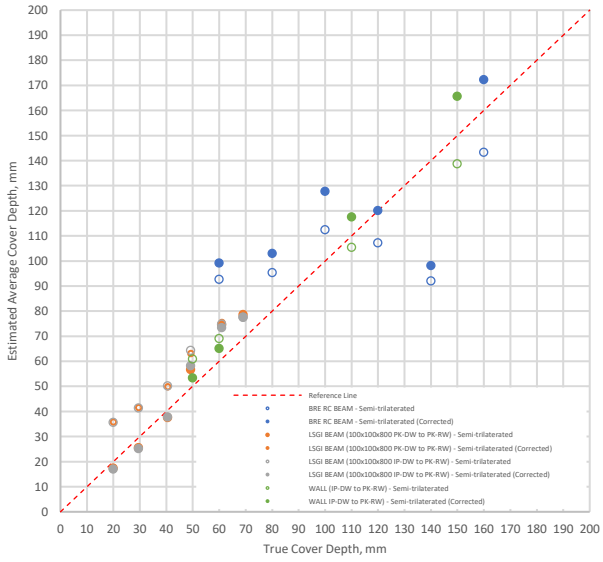

Figure 6.4.4-1 Estimated depth by Semi-Trilaterated method before and after correction by linear regression versus actual cover depth

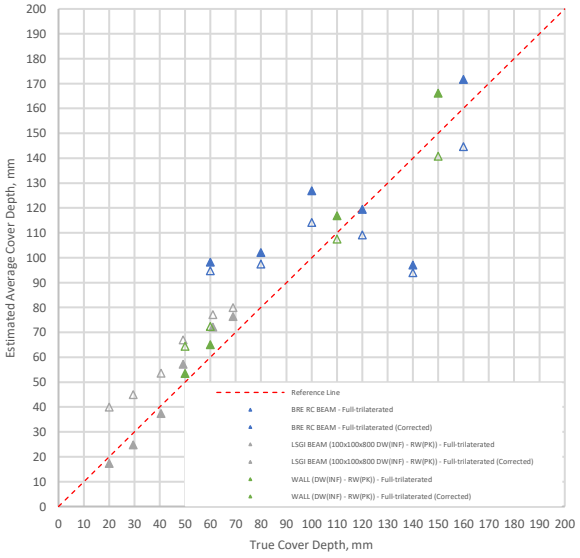

Figure 6.4.4-2 Estimated depth by Full-Trilaterated method before and after correction by linear regression versus actual cover depth

Comparing the plots shown in Figure 6.4.4-1 and 6.4.4-2, both the Semi-Trilateration method and Full-Trilaterated method can acquire high accuracy in estimating cover depth especially cover depth of over 70mm. The accuracy of the estimated cover depth by the Semi-Trilateration method is slightly higher than the Full-Trilateration method. However, both methods highly over-estimated the cover depth when the cover depth is 70mm or less. Full-trilateration method is slightly higher over-estimated the cover depth than the Semi-trilateration method. After correction, it is obvious that both proposed linear regression corrections can significantly improve the estimation of cover

depth and with high accuracy to the actual cover depth. The considerable improvement was achieved at shallow cover depth, i.e. 70mm or less.

Based on the findings, discussions are listed below:

1) According to the accuracy of cover depth estimation of all verification cases, i.e. Case 1-22, as shown in Figure 6.4.4-1 and 6.4.4-2, the average percentage of error between estimated cover depth and actual cover depth by Semi-Trilaterated method and Full-Trilaterated method can be separated into two different depth ranges including cover depth of 70mm or less, and over 70mm.
2) The average percentage of error between estimated cover depth and actual cover depth by the Semi-Trilaterated method and Full-Trilaterated method of cover depth 70mm or below is 33.9% and 41.0% respectively. After correction by the linear regression model, the average percentage of error between estimated cover depth and actual cover depth by Semi-Trilaterated method and Full-Trilaterated method is improved to 7.5% and 9.6% respectively. The high accuracy result between the estimated cover depth and actual cover depth by the linear regression algorithm is obtained.
3) While, for cover depth over 70mm, the average percentage of error between estimated cover depth and actual cover depth by the Semi-Trilateration method and Full-Trilaterated method is -5.1% and -3.5% respectively. After correction by the linear regression model, the average percentage of error between estimated cover depth and actual cover depth by Semi-Trilaterated method and Full-Trilaterated method is improved to 7.4% and 6.8% respectively. Thus, the linear regression algorithm is well performed in a cover depth of 70mm or below. For cover depth over 70mm, the linear regression algorithm is not applicable as the correction is developed based on a dataset of cover depth 20mm to 70mm.
4) The success of the correction by the linear regression algorithm is highly dependent on the initial value of the estimated velocity, time and estimated depth with consideration of antenna separation and radius of the target round object. If the accuracy of the initial value estimated by the Semi-Trilateration method and Full-trilateration method is unsatisfactory, the correction by the linear regression algorithm is no longer applicable to improve the estimated cover depth.

6.4.5 Analysis of the Corrected Semi-Trilaterated and Corrected Full-Trilateration algorithm

Regression analysis to study the fitting quality of the data after correction by Semi-Trilaterated and Corrected Full-Trilateration algorithm is conducted. For a confidence level of 95%, the average residual of the estimated depth and $\pm 1.96 * SD$, which SD represent the standard deviations of the residuals in estimated depth, are calculated. The result is listed in table 6.4.5-1.

	Case No	Actual cover	Estimation Method	Before Correction	After Correction				
				Average Estimated Depth	Average Estimated Depth (Corrected)	Residual	S.D.	95% Confidence Interval (Lower limit)	95% Confidence Interval (Upper limit)
		(mm)		(mm)	(mm)			(mm)	(mm)
LSGI Concrete Beam	1	69	STM	78.5	78.7	9.7	0.6	77.5	79.9
	2	61	STM	75.6	74.6	13.6	0.9	72.9	76.3
	3	49.3	STM	63.2	56.7	7.4	0.5	55.8	57.6
	4	40.5	STM	49.9	37.5	-3	0.2	37.1	37.9
	5	29.5	STM	41.6	25.5	-4	0.3	25	26
	6	20	STM	36	17.4	-2.6	0.2	17.1	17.7
	7	69	STM	77.6	77.5	8.5	0.6	76.4	78.6
	8	61	STM	74.8	73.3	12.3	0.8	71.7	74.9
	9	49.3	STM	64.3	58.3	9	0.6	57.2	59.4
	10	40.5	STM	50.2	37.9	-2.6	0.2	37.6	38.2
	11	29.5	STM	41.4	25.2	-4.3	0.3	24.7	25.7
	12	20	STM	35.7	17	-3	0.2	16.6	17.4
CEE Concrete Wall	13	50	STM	60.9	53.3	3.3	1	51.3	55.3
	14	60	STM	69	65.1	5.1	1.6	61.9	68.3
	15	110	STM	105.4	117.6	7.6	2.4	112.9	122.3
	16	150	STM	138.8	165.7	15.7	5	156	175.4
BRE Concrete Beam	17	60	STM	92.7	99.2	39.2	12.4	74.9	123.5
	18	80	STM	95.3	103	23	7.3	88.7	117.3
	19	100	STM	112.5	127.8	27.8	8.8	110.6	145
	20	120	STM	107.2	120.1	0.1	0	120	120.2
	21	140	STM	92	98.2	-41.8	13.2	72.3	124.1
	22	160	STM	143.3	172.2	12.2	3.9	164.6	179.8
LSGI Concrete Beam	7a	69	FTM	80	76.4	7.4	0.5	75.5	77.3
	8a	61	FTM	77.1	72.1	11.1	0.7	70.7	73.5
	9a	49.3	FTM	67	57.2	8	0.5	56.2	58.2
	10a	40.5	FTM	53.5	37.4	-3.1	0.2	37	37.8
	11a	29.5	FTM	44.9	24.7	-4.8	0.3	24.1	25.3

	12a	20	FTM	39.9	17.3	-2.7	0.2	17	17.6
CEE Concrete Wall	13a	50	FTM	64.4	53.4	3.4	1.1	51.3	55.5
	14a	60	FTM	72.3	65.1	5.1	1.6	61.9	68.3
	15a	110	FTM	107.4	116.9	6.9	2.2	112.6	121.2
	16a	150	FTM	140.8	166.1	16.1	5.1	156.1	176.1
BRE Concrete Beam	17a	60	FTM	94.7	98.2	38.2	12.1	74.5	121.9
	18a	80	FTM	97.4	102.1	22.1	7	88.4	115.8
	19a	100	FTM	114.2	126.8	26.8	8.5	110.2	143.4
	20a	120	FTM	109.1	119.4	-0.6	0.2	119	119.8
	21a	140	FTM	94	97	-43	13.6	70.3	123.7
	22a	160	FTM	144.6	171.7	11.7	3.7	164.4	179

Table 6.4.5-1 Estimated depth by Full-Trilaterated method before and after correction by linear regression versus actual cover depth (Note: STM and FTM represent Semi-Trilaterated Method and Full-Trilaterated Method)

For Case 1-16 and Case 7a-16a estimated cover depth by the Semi-Trilateration Method and Full-Trilateration method respectively, the average standard deviation (S.D.) of the estimated cover depth is around 0.4 which is close to zero. For satisfactory quality of the fitting data with a 95% confidence level, the confidence intervals are computed as shown in Table 6.4.5-1. It means that 95% of the collected samples should fall within the confidence interval, i.e. mean $\pm$ 1.96*S.D.

6.5 Summary

Observations and limitations are summarized below:

Observations:

1. To verify the Semi-Trilaterated method, Full-Trilaterated method, Corrected Semi-Trilaterated method and Corrected Full-Trilaterated method, a total of A-scans of 2337 round rebar with reflected hyperbolic footprint were obtained. For each footprint, the cover depth estimation is based on the estimation of velocity which makes use of 20 to 50 points, i.e. average 35 points of x,t. Therefore, by multiplying the number of experiments by several rebars and data points in radargram, the evaluation of the estimated cover depth was based on the large number of 87,795 data points, i.e. (x_i, t_i) from the reflected hyperbolic footprint in radargrams.

2. The average percentage of error between estimated cover depth and actual cover depth by the Semi-Trilateration method and Full-Trilateration method is 21.5% and 21.6% respectively. After correction by the linear regression model, the average percentage of error between estimated cover depth and actual cover depth by Semi-Trilaterated method and Full-Trilaterated method is improved to 7.5% and 8.4% respectively.
3. For cover depth 70mm or below, the discrepancy between the actual cover depth and estimated cover depth estimated by the Semi-Trilateration method and Full-Trilateration method is significantly reduced from an average of 13.5mm and 17.2mm respectively to 5.9mm and 7.0mm.
4. The accuracy of cover depth estimation by using Semi-trilateration method is slightly better than using the Full-Trilaterated method.
5. The accuracy of cover depth estimation by using the Inflection Point (IP) of Direct Wave (DW) as the reference point is slightly better than using the Peak (PK) of DW to the PK of Reflected Wave (RW).

Limitations:

1. The linear regression correction algorithm is developed based on homogeneous material and lossless medium, i.e. air-cured concrete.
2. It is crucial to obtain the well-determined initial value of the estimated velocity, time and estimated depth with consideration of antenna separation and radius of the target round object as the correction by the linear regression algorithm is highly dependent on the well-determined initial value.
3. It is crucial to consider the vertical spatial resolution between the target object and surrounding interface/deeper object(s) to avoid overlapping of DW and RW from the target object with RW from the surrounding interface/deeper object(s). As explained in Section 2.2.4, the recommended minimum vertical distance is half of the nominal wavelength, i.e. the ratio between the depth of the target object and surrounding interface/deeper object(s) and the nominal wavelength (d/λ) is approximately 2. While the ratio of d/λ for cover depth of 10 and 80 is approximately 0.72.
4. It is worth taking note that in the correction models and for cover depth over 70mm (i.e. wavelength 49.1mm or less), the correction by linear regression algorithm is not applicable

as the correction is developed based on the dataset of cover depth 20mm to 70mm. This ratio of the wavelength can be extended to the estimation of deeper objects making use of lower frequency antenna and longer wavelength.

5. However, there are shortcomings in the linear regression models. Firstly, Equation 6.2-2 and 6.2-3 only correct the estimated depth. However, both the velocity and the two-way travel time are independent observations with random error, which the corrections should be conducted. Secondly, the correction of the linear regression model normally requires iterative calculation. Thirdly, convergency analysis is required for each iterative calculation to ensure a convergent solution for the minimization. Finally, the linear regression model is a simplified model for the near field problem, i.e. 20 and 30mm cover, that may be better solved by a non-linear model.

7 Conclusions

This study aimed to recognize the potential sources of error, minimize and correct the error and evaluate the uncertainty in the GPR measurement of concrete reinforcement cover by developing a standard model. A summary was systematically reported as below and tabulated in Table 7.1-1.

7.1 Summary of main findings

As depicted in Chapter 3, the potential sources of errors were classified into three different areas including the host material, the ray-path geometry, and equipment & signal processing.

The first identified sources of error of host material are water content inside concrete and heterogeneous material, i.e. 10mm and 20 aggregates. For the presence of water content inside the concrete, as described and explained in Chapter 5, it governed the TWTT, GPR wave velocity and relative permittivity, i.e. (x_i, t_i), and resulted in variation of depth measurement. This effect of water on depth estimation of rebar was proved minimal with an increase in the age of concrete and the ray-path model by semi- and full trilateration method remains valid and reliable. While the presence of aggregates inside the concrete, it causes two types of scattering including Rayleigh and Mie and is dependent on the object to wavelength ratio. The scattering effect will affect the measurement of TWTT and depth, i.e. (x_i, t_i), which increases the standard errors or deviations in the measurement. However, the error induced by the scattering effect was relatively insignificant due to the similar dielectric properties and thus small contrast of hydrated Portland cement product bonded with aggregate in comparison with the high contrast of relative permittivity of metallic reinforcement.

The second identified source of error in the geometry of the ray path is measuring techniques - common offset profiling, target types, and object size and antenna separation. For the measuring technique which influences the measurement of TWTT and depth, i.e. (x_i, t_i), the common offset profiling (COP) method with common antenna offset applied for known size round object was considered. Semi- and full-trilateration ray-path models with associated errors were evaluated and minimized for the semi-trilateration model in Chapter 4 and 6. Comparing the accuracy of the

measured depth between the semi- and full trilateration method in the validated experiment, the semi-trilateration method provided a closer and better estimation. The new algorithm developed based on the semi-trilaterated algorithm and root mean square error was used in uncertainty evaluation, and confidence level and interval for the correction and estimation on-site test.

The third identified source of error is equipment and signal processing. The definition of time zero, antenna types, antenna frequency and component frequency of the hyperbolas dictated the time (t_i), and a digital sampling rate of the analogue signals govern the measurement of TWTT and depth, i.e. (x_i, t_i). The time zero is defined at the first of the point of inflection of the direct wave but its associated error and uncertainty cannot be minimized as it is an unknown. For antenna frequency and component frequency of the hyperbolas, they were realized in wavelet transform but errors cannot be minimized as they are related to time zero. Finally, for the digital sampling range of the analogue signals, no correction or minimization was required as an insignificant effect was found to influence the uncertainty measurement.

The fourth identified source of error is the combined factors effect of reactive near field and Fresnel region. The effect significantly influences the accuracy of measurement depth of buried objects. It is important to consider this effect when using GPR antenna as measuring tools with different frequency spectrum as the measuring limits and the range of the reactive near zone are also different. The reliable measurement is only available in the far-field region.

Sources of errors		Measured/ dependent variables in this thesis	Related chapters			**Treatments**
			4	5	6	
1. Dielectric properties of the host materials	1.1 Water content	x_i, t_i		✓		**Modelled and minimized**
	1.2 Heterogeneous materials inside concrete with size comparable to GPR wavelength, e.g. aggregate	x_i, t_i		✓	✓	**Modelled and minimized**
2. Geometry of the ray-path	2.1 Common offset profiling (COP)/WARR/CMP	x_i, t_i	Data collection and ray-path model by COP method, and round-shaped rebar			**Recognized and modelling/ correction/ minimization was not taken**
	2.2 Target types (round/flat/slanted)	x_i, t_i				
	2.3 Object size and antenna separation	x_i, t_i	✓	✓	✓	**Modelled and minimized**
3. Equipment & signal processing	3.1 Definition of time zero	t_i	✓	✓		**Modelled but cannot be minimized**
	3.2 Antenna types (bowtie, horn, etc.)	x_i, t_i	Dipole antenna with fixed separation distance			**Recognized but cannot be minimized**
	3.3 Antenna frequency and component frequency of the hyperbolas	t_i			✓	**Recognized but cannot be minimized**
	3.4 Digital sampling rate of the analogue signals	x_i, t_i			✓	**Recognized and found not to cause significant effect**
4 Combined factors	4.1 Near-field and far-field	x_i, t_i	✓			**Recognized and modelling/ correction/ minimization was not taken**

Table 7.1-1 Treatments of errors from various sources (modified from Table 3.2-1)

Note: Chapter 4 semi- and full trilateration model with effect of near-field and far-field problems on accuracies of cover depth measurement; Chapter 5 semi- and full trilateration model with consideration of effect of ages of concrete and moisture content; Chapter 6 an accurate algorithm to estimate the cover depth based on semi-trilateration method and statistical root mean square errors with uncertainty evaluation

7.2 Limitations and future recommendation

Limitations as listed below:

1. Scattering effect in Rayleigh and Mie type does not significantly affect the measurement of TWTT and depth, i.e. (x_i, t_i), in hyperbolic reflections of radargram due to high contrast of relative permittivity of metallic reinforcement.
2. Time zero is the key source of uncertainties and not concluded in this thesis because the uncertainty of time zero is interrelated with host material, scattering effect, antenna frequency and depth which the degree of uncertainty due to combined effect is difficult to be generalized.
3. The monostatic antenna used in this study is a dipole antenna with a fixed separation distance and specified frequency. Different types and frequency antenna are available in the market, but the ray-path model mentioned in this thesis may not be applicable.
4. According to the result of estimated depth in Chapter 4 and summary of main findings in Chapter 7, the results showed that the Semi-trilateration Method (STM) provided a closer and better estimation of cover depth. Compared with STM, the Full-trilateration Method (FTM) overestimated the cover depth. The possible reasons causing overestimation are listed below,
    a) As explained in Section 2.4, the FTM considered the combination of algorithms, i.e. equations (2.4-3), (2.4-1) and (2.4-4). Firstly, the approximated GPR wave velocity 'v' is obtained by STM, i.e. equation (2.4-3). The method considered the antenna separation and the target object a point source as shown in Figure 7.2-1. Secondly, by making use of an approximated velocity 'v' and by equation (2.4-1), an 'approximated D0' is obtained. Finally, the 'approximated' 'D_0' inputs in Multi-trilateration method (MTM), i.e. equation (2.4-4), as shown in Figure 7.2-2 and (2.4-1) which helps to estimate 'v' and 'd' respectively. The estimated cover depth 'd' is the approximation of rebar cover depth, "D_0". It is the trilaterated ray-path which is longer than the estimated depth, i.e. D_0.

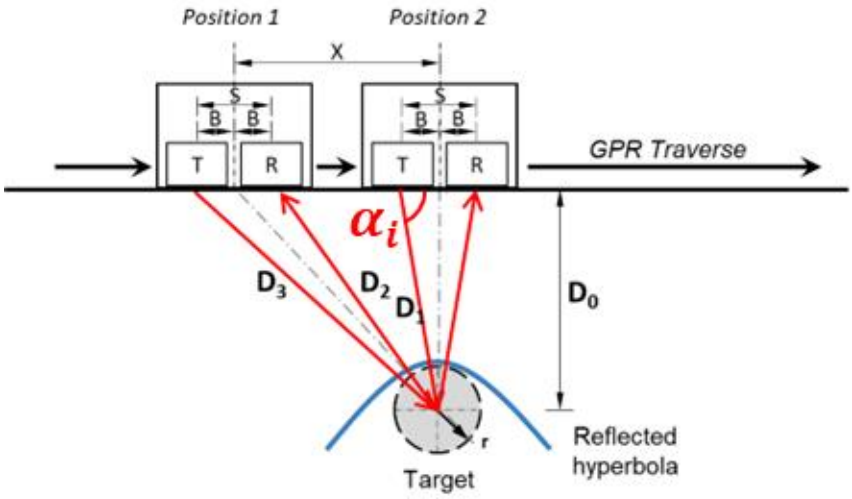

Figure 7.2-1 Schematic diagram of Semi-trilateration ray-path model (STM) (Sham & Lai, 2016)

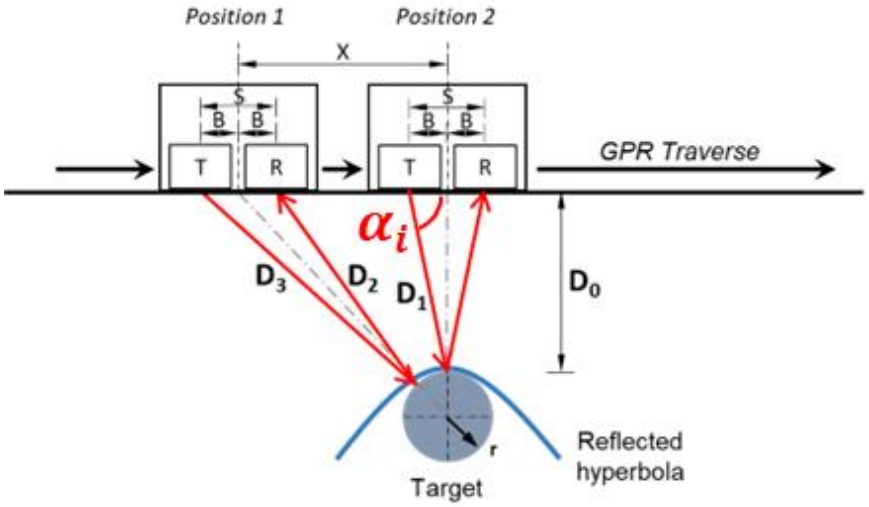

Figure 7.2-2 Schematic diagram of Multi-trilateration ray-path model (MTM) (Xie et al., 2018)

b) The 'approximated D_0' by STM is overestimated because (i) the target object is taken as a point, (ii) near-field effect and (iii) hydration effect as explained in Chapter 4.

c) As the 'approximated D_0' by STM inputs into the MTM, i.e. Equation (2.4.4), this led to 2nd time ray-path trilaterated effect which further lengthens the ray-path. Also, the estimated depth, i.e. D_0, by Equation (2.4-1) is based on t_0 obtained in STM.

d) Again, the obtained estimated depth by MTM should be corrected by applying sine θ_i and expressed in Equation (7.2-1).

For future works, it is recommended to develop:

1. A standard method of measurement with the explanation of validity and limitation of measurement, accuracy of measurement, and a specification on the quality level of measurement for reinforced concrete can be published as a code or standard to the stakeholders including client, engineer, surveyor and contractor.
2. A refinement on the algorithms of depth estimation. The obtained estimated depth by STM, MTM and FTM should be corrected by applying sine θ_i to the approximated depth in order to determine the vertical cover depth, i.e. D_0, as expressed in Equation (7.2-1).

$$D_0 = D_1 \times \sin\theta_i \tag{7.2-1}$$

3. For FTM, the 'approximated D_0' by STM to be inputted in MTM should conduct ray-path transformation as the ray-path of STM is longer than FTM.

   The equation of ray-path length AOB by STM and AO'B by MTM as shown Figures 7.2.3 and 7.2.4 and the equation can be expressed below respectively,

$$\frac{AOB}{2} = \frac{(AO + OB)}{2} = \frac{D_3 + D_2}{2} = \frac{1}{2} * \{\sqrt{[D_o{}^2 + [x + B]^2]} + \sqrt{[D_o{}^2 + [x - B]^2]}\} \tag{7.2-2}$$

$$\frac{AO'B}{2} = \frac{(AO' + O'B)}{2} = \frac{D_3 + D_2}{2}$$

$$= \frac{1}{2} * \{\sqrt{\left[(D_o + r) - \frac{(D_o + r)r}{\sqrt{(D_o + r)^2 + x^2}}\right]^2 + \left[\left(x - \frac{r \times x}{\sqrt{(D_o + r)^2 + x^2}}\right) + B\right]^2} + \sqrt{\left[(D_o + r) - \frac{(D_o + r)r}{\sqrt{(D_o + r)^2 + x^2}}\right]^2 + \left[\left(x - \frac{r \times x}{\sqrt{(D_o + r)^2 + x^2}}\right) - B\right]^2}\} \tag{7.2-3}$$

The 'approximated D_0', i.e. the trilaterated ray-path, by STM should be transformed to FTM ray-path by applying the modification factor (M.F.) and the equation is expressed as below,

$$Estimated\ FTM\ Ray - path\ length =$$
$$Estimated\ STM\ Raypath\ length\ x\ Modification\ Factor\ (M.F.)$$
$$Modification\ Factor\ (M.F.) = \frac{FTM\ Raypath\ length}{STM\ Raypath\ length} \tag{7.2-4}$$

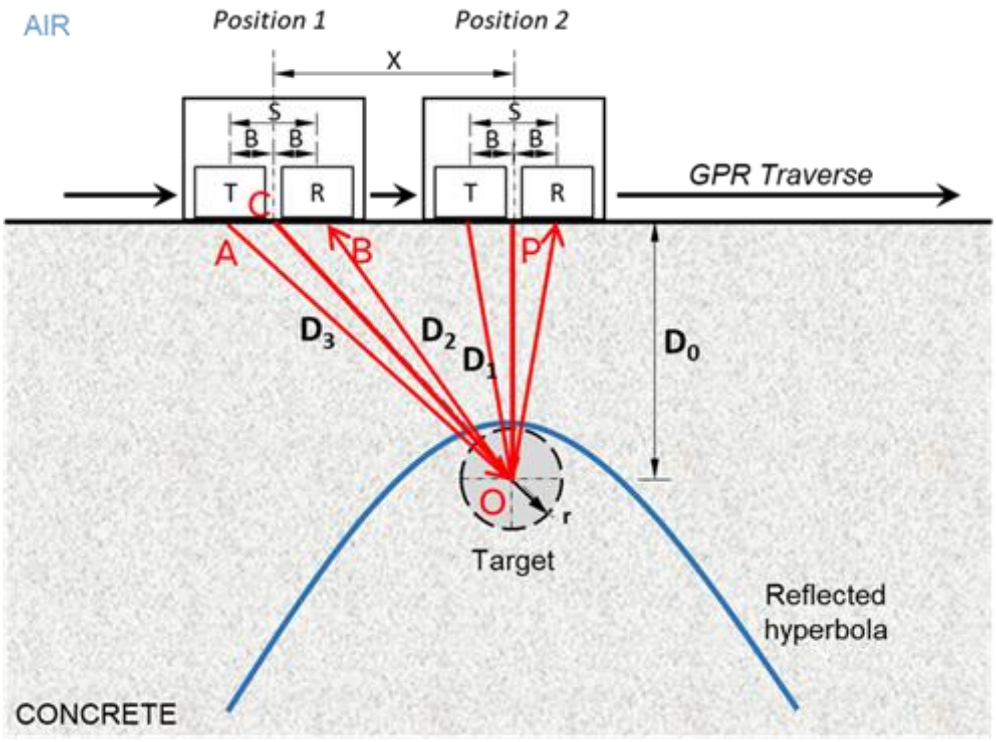

Figure 7.2-3 Schematic diagram of ray-path AOB by Semi-trilateration Model (STM) (Sham & Lai, 2016)

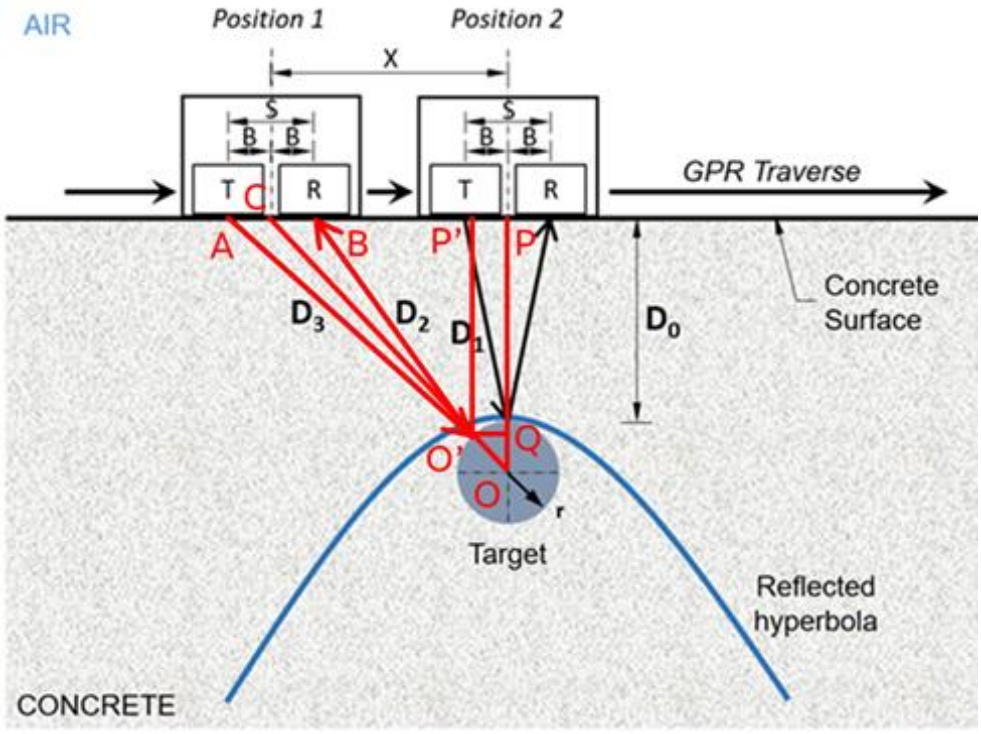

Figure 7.2-4 Schematic diagram of ray-path AO'B by Multi-trilateration Model (MTM) (Xie et al., 2018)

7.3 Contributions to knowledge

The research studies contribute to the development of standard models to evaluate all possible errors causing uncertainty during concrete cover depth measurement with a solution to model, correct and minimize the impact of possible errors. The developed algorithm provides a refinement/correction on the estimated concrete cover depth and its uncertainty estimation in concrete evaluation especially quality control and durability evaluation on the remaining service life of the structures. It raises the awareness of the often-neglected physical phenomena about near-field problems when GPR is used as a measurement tool and provides a modelling solution for the correction or minimization of the total errors. The developed methodology and correction model should be equally applicable to other GPR measurements on deeper objects making use of lower frequency antenna, especially underground utilities.

8 References

A.M. Alzahed and S.M. Mikki (2018). *Antenna RCS characterization using SEM approach.* Defence Research and Development Canada, retrieved from chrome-extension://efaidnbmnnnibpcajpcglclefindmkaj/viewer.html?pdfurl=https%3A%2F%2Fcradpdf.drdc-rddc.gc.ca%2FPDFS%2Func327%2Fp808085_A1b.pdf&clen=2891102&chunk=true.

Al-Nuaimy, W., Shihab, S., & Eriksen, A. (2004). *Data fusion for accurate characterisation of buried cylindrical objects using GPR.* Paper presented at the Proceedings of the Tenth International Conference on Grounds Penetrating Radar, 2004. GPR 2004.

Al-Qadi, I. L., & Lahouar, S. (2005). Measuring layer thicknesses with GPR–Theory to practice. *Construction and Building Materials, 19*(10), 763-772.

Al-Qadi, I. L., Lahouar, S., Jiang, K., McGhee, K. K., & Mokarem, D. (2005). Accuracy of ground-penetrating radar for estimating rigid and flexible pavement layer thicknesses. *Transportation Research Record, 1940*(1), 69-78.

Almeida, E. R., Porsani, J. L., Catapano, I., Gennarelli, G., & Soldovieri, F. (2015). Microwave tomography-enhanced GPR in forensic surveys: The case study of a tropical environment. *IEEE Journal of Selected Topics in Applied Earth Observations and Remote Sensing, 9*(1), 115-124.

André, F., Jonard, M., & Lambot, S. (2014). Non-invasive forest litter characterization using full-wave inversion of microwave radar data. *IEEE Transactions on Geoscience and Remote Sensing, 53*(2), 828-840.

Annan, A. (2009). Electromagnetic principles of ground penetrating radar. *Ground penetrating radar: theory and applications, 1*, 1-37.

Annan, A. P. (2004). *Ground Penetrating Radar Applications, Principles, Procedures*. Mississauga, Canada: Sensors and Software.

Anspach, J. H. (2002). *Standard guideline for the collection and depiction of existing subsurface utility data.* Paper presented at the Pipelines 2002: Beneath Our Feet: Challenges and Solutions.

Arras, K. O. (1998). An introduction to error propagation: Derivation, meaning and examples of cy= fx cx fx'. ETH Zurich.

ASTM International. (2011). Standard guide for using the surface ground penetrating radar method for subsurface investigation. ASTM International.

ASTM Standard D6432. (2019). *Standard Guide for Using the Surface Ground Penetrating Radar Method for Subsurface Investigation, ASTM International*. West Conshohocken, PA, 2011.

Australia, Standards. (2013). Classification of subsurface utility information (SUI). In. Standards Australia.

Balanis, C. (2005). A.,"Antenna Theory Analysis and Design," 3rd ed., JohnWiley& Sons. *Inc., Publication*.

Balanis, C. A. (2011). *Modern antenna handbook*: John Wiley & Sons.

Balanis, C. A. (2012). *Advanced engineering electromagnetics*: John Wiley & Sons.

Barnes, C. L., Trottier, J.-F., & Forgeron, D. (2008). Improved concrete bridge deck evaluation using GPR by accounting for signal depth–amplitude effects. *NDT & E International, 41*(6), 427-433.

Beek, V. A. (2000). *Dielectric Properties of Young Concrete*. PhD Thesis, Delft University.

Ben-Gal, I. (2007). Bayesian Networks (PDF). Ruggeri, Fabrizio; Kennett, Ron S.; Faltin, Frederick W." Encyclopedia of Statistics in Quality and Reliability". Encyclopedia of Statistics in Quality and Reliability. John Wiley & Sons. doi, 10, 9780470061572.

Bienkowski P. & Trzaska H., (2012). *Electromagnetic Measurements in the Near Field.* SciTech Publishing, Inc.

Benedetto, A., & Pajewski, L. (2015). Civil engineering applications of ground penetrating radar: Springer.

Benedetto, A., Tosti, F., Ciampoli, L. B., & D'amico, F. (2017). An overview of ground-penetrating radar signal processing techniques for road inspections. *Signal Processing, 132*, 201-209.

Bland, J. M., & Altman, D. G. (1996). Statistics notes: measurement error. *Bmj, 312*(7047), 1654.

Bleaney, B. I., Bleaney, B. I., & Bleaney, B. (2013). *Electricity and Magnetism, Volume 2* (Vol. 2): Oxford University Press.

Blischke, W. R., & Murthy, D. P. (2011). *Reliability: modeling, prediction, and optimization* (Vol. 767): John Wiley & Sons.

Boniger, U., & Tronicke, J. (2010). On the potential of kinematic GPR surveying using a self-tracking total station: Evaluating system crosstalk and latency. *IEEE Transactions on Geoscience and Remote Sensing, 48*(10), 3792-3798.

Boniger, U., & Tronicke, J. (2011). Subsurface utility extraction and characterization: Combining GPR symmetry and polarization attributes. *IEEE Transactions on Geoscience and Remote Sensing, 50*(3), 736-746.

Borgelt, C., & Kruse, R. (2002). Graphical Models---Methods for Data Analysis and Mining *John Wiley&amp*.

Borsuk, M. E., Stow, C. A., & Reckhow, K. H. (2004). A Bayesian network of eutrophication models for synthesis, prediction, and uncertainty analysis. *Ecological Modelling, 173*(2-3), 219-239.

G. Breed (2007). *Basic principles of electrically small antennas*. Summit Technical Media, LLC

Bristow, C. S., & Jol, H. M. (2003). *Ground penetrating radar in sediments*.

Bungey, J.H. (2004). Sub-surface radar testing of concrete: a review. *Construction and Building Materials*. 18(1), 1-8.

Campbell, J. B., & Wynne, R. H. (2011). *Introduction to remote sensing*: Guilford Press.

Cassidy, N.J. (2009). *Electrical and Magnetic Properties of Rocks, Soils and Fluids, Chapter 2 in Ground Penetrating Radar: Theory and Applications*. Jol H.M. Ed., Elsevier.

Celikyilmaz, A., & Turksen, I. B. (2009). Modeling uncertainty with fuzzy logic. *Studies in fuzziness and soft computing, 240*, 149-215.

Chan, C. Y., & Knight, R. J. (2001). Laboratory measurements of electromagnetic wave velocity in layered sands. *Water resources research, 37*(4), 1099-1105.

Cole, K. and Cole, R. (1941). Dispersion and Absorption in Dielectrics; I: Alternating Current Characteristics. *Journal of Chemical Physics*, 9, 341-351.

Concrete Society (1997). *Guidance on Radar Testing of Concrete Structures.* Concrete Society Technical Report 48.

Conyers, L. B. (2013). *Ground-penetrating radar for archaeology*: Altamira Press.

Cordua, K. S., Hansen, T. M., & Mosegaard, K. (2012). Monte Carlo full-waveform inversion of crosshole GPR data using multiple-point geostatistical a priori information. *Geophysics, 77*(2), H19-H31.

Costello, S., Chapman, D., Rogers, C., & Metje, N. (2007). Underground asset location and condition assessment technologies. *Tunnelling and Underground Space Technology, 22*(5), 524-542.

Daniels, D. J. (2004). *Ground penetrating radar* (Vol. 1): Iet.

Davis, J.L. and Annan, A.P. (1989). Ground-Penetrating Radar for High-Resolution Mapping of Soil and Rock Stratigraphy. *Geophysical Prospecting*, 37, 531-551.

Debye P. (1920). *Polar Molecules*. Chemical Publication Company.

Deng, R., & Liu, C. (1999). FM-CW radar performance in a lossy layered medium. *Journal of Applied Geophysics, 42*(1), 23-33.

Derobert, X., & Pajewski, L. (2018). *The GPR dataset of the IFSTTAR Geophysical Test Site.* Paper presented at the EGU General Assembly Conference Abstracts.

Dérobert, X., & Pajewski, L. (2018). TU1208 open database of radargrams: The dataset of the IFSTTAR geophysical test site. *Remote Sensing, 10*(4), 530.

Dobson M.C., Ulaby, F.T., Hallikainen, M.T. and El-Rayes, M.A. Microwave Dielectric (1985). Behavior of Wet Soil – Part II: Dielectric Mixing Models. *IEEE Transactions on Geoscience and Remote Sensing*, GE-23(1), 35-46.

Dojack L. (2012). Ground Penetrating Radar Theory, Data Collection, Processing, and Interpretation: A Guide for Archaeologists. Retrieved from https://open.library.ubc.ca/soa/cIRcle/collections/graduateresearch/42591/items/1.0086065

Dolgiy, A., Dolgiy, A., & Zolotarev, V. (2006). *Optimal radius estimation for subsurface pipes detected by ground penetrating radar.* Paper presented at the Proceedings 11th International Conference on Ground Penetrating Radar, Columbus, Ohio, USA.

Doolittle, J. A., & Asmussen, L. E. (1992). *The years of applications of ground penetrating radar by the United States department of Agriculture.* Paper presented at the Fourth International Conference on Ground Penetrating Radar.

Ekes, C., & Neducza, B. (2012). *Pipe condition assessments using pipe penetrating radar.* Paper presented at the 2012 14th International Conference on Ground Penetrating Radar (GPR).

Feldman, R. F. and Sereda, P. J., (1968). A model for hydrated Portland cement paste as deduced from sorption-length change and mechanical properties. *Matériaux et Construction*, 1(6), 509-520.

Ferrara, V., Pietrelli, A., Chicarella, S., & Pajewski, L. (2018). GPR/GPS/IMU system as buried objects locator. *Measurement, 114*, 534-541.

Fioranelli, F. (2013). Through-the-wall detection using ultra wide band frequency modulated interrupted continuous wave signals. Durham University,

Fitzgibbon, A., Pilu, M., & Fisher, R. B. (1999). Direct least square fitting of ellipses. *IEEE Transactions on pattern analysis and machine intelligence, 21*(5), 476-480.

Fleisch, D. (2008). *A student's guide to Maxwell's equations*: Cambridge University Press.

Friedman, N., Geiger, D., & Goldszmidt, M. (1997). Bayesian network classifiers. *Machine learning, 29*(2-3), 131-163.

G. Lu, W. Zhao, E. Forte, G. Tian, Y. Li and M. Pipan (2020). Multi-frequency and multi-attribute GPR data fusion based on 2-D wavelet transform. *Measurement* 166, 108243.

Galagedara, L., Parkin, G., Redman, J., Von Bertoldi, P., & Endres, A. (2005). Field studies of the GPR ground wave method for estimating soil water content during irrigation and drainage. *Journal of Hydrology, 301*(1-4), 182-197.

Gallagher, K., Sambridge, M., & Drijkoningen, G. (1991). Genetic algorithms: An evolution from Monte Carlo Methods for strongly non-linear geophysical optimization problems. *Geophysical Research Letters, 18*(12), 2177-2180.

Gamo, H. (1979). A general formulation of Faraday's law of induction. *Proceedings of the IEEE, 67*(4), 676-677.

Getzlaff, M. (2007). *Fundamentals of magnetism*: Springer Science & Business Media.

Giannakis, I., Giannopoulos, A., & Warren, C. (2015). A realistic FDTD numerical modeling framework of ground penetrating radar for landmine detection. *IEEE Journal of Selected Topics in Applied Earth Observations and Remote Sensing, 9*(1), 37-51.

Giannopoulos, A. (1998). The investigation of transmission-line matrix and finite-difference time-domain methods for the forward problem of ground probing radar. University of York,

Gilboa, I. (2009). *Theory of decision under uncertainty* (Vol. 45): Cambridge university press.

Gorur, K., Smit, M.K., and Witman, F.H. (1982). Microwave study of hydrating paste at early age. *Cement and Concrete Research*, 12, 447.

Grant, I. S., & Phillips, W. R. (2013). *Electromagnetism*: John Wiley & Sons.

Grote, K., Anger, C., Kelly, B., Hubbard, S., & Rubin, Y. (2010). Characterization of soil water content variability and soil texture using GPR groundwave techniques. *Journal of Environmental & Engineering Geophysics, 15*(3), 93-110.

Guy, E. D., Daniels, J. J., Radzevicius, S. J., & Vendl, M. A. (1999). Demonstration of using crossed dipole GPR antennae for site characterization. *Geophysical Research Letters, 26*(22), 3421-3424.

Halpern, J. Y. (2017). *Reasoning about uncertainty*: MIT press.

Hammersley, J. (2013). *Monte carlo methods*: Springer Science & Business Media.

Hansen, T. M., & Cordua, K. S. (2017). Efficient Monte Carlo sampling of inverse problems using a neural network-based forward—applied to GPR crosshole traveltime inversion. *Geophysical Journal International, 211*(3), 1524-1533.

Hao, T., Rogers, C. D. F., Metje, N., Chapman, D. N., Muggleton, J. M., Foo, K. Y., . . . Saul, A. J. (2012). Condition assessment of the buried utility service infrastructure. *Tunnelling and Underground Space Technology, 28*, 331-344. doi:10.1016/j.tust.2011.10.011

Hayakawa, H., & Kawanaka, A. (1998). Radar imaging of underground pipes by automated estimation of velocity distribution versus depth. *Journal of Applied Geophysics, 40*(1-3), 37-48.

Helton, J. C., Johnson, J. D., Sallaberry, C. J., & Storlie, C. B. (2006). Survey of sampling-based methods for uncertainty and sensitivity analysis. *Reliability Engineering & System Safety, 91*(10-11), 1175-1209.

HKIUS. (2012). Guide to utility survey by non-destructive method (using pipe/cable locator) in Hong Kong. In: HK: Utility Training Institute.

HKIUS. (2014). Particular specification for utility mapping by non-destructive methods. In. HKIUS-UT PS: HK: Utility Training Institute.

Hoeskstra P. and Doyle W.T. (1971). Dielectric relaxation of surface absorbed water. *Journal of Colloidal and Interface Science*, 79(11), 1699-1708.

Höfinghoff, J.-F., & Overmeyer, L. (2013). Resistive loaded antenna for ground penetrating radar inside a bottom hole assembly. *IEEE transactions on antennas and propagation, 61*(12), 6201-6205.

Hofmann-Wellenhof, B., Lichtenegger, H., & Collins, J. (2012). *Global positioning system: theory and practice*: Springer Science & Business Media.

Huang, C., & Su, Y. (2004). *A new GPR calibration method for high accuracy thickness and permittivity measurement of multi-layered pavement.* Paper presented at the Proceedings of the Tenth International Conference on Grounds Penetrating Radar, 2004. GPR 2004.

Hugenschmidt, J., & Loser, R. (2008). Detection of chlorides and moisture in concrete structures with ground penetrating radar. *Materials and Structures, 41*(4), 785-792.

Huisman, J., Hubbard, S., Redman, J., & Annan, A. (2003). Measuring soil water content with ground penetrating radar. *Vadose zone journal, 2*(4), 476-491.

Huisman, J. A., Hubbard, S. S., Redman, J. D., & Annan, A. P. (2003). Measuring soil water content with ground penetrating radar: A review. *Vadose zone journal, 2*(4), 476-491.

Huray, P. G. (2011). *Maxwell's equations*: John Wiley & Sons.

ICE. (2014). PAS 128: British standard: Specification for underground utility detection, verification and location In *British standard: Specification for underground utility detection, verification and location* British Standard Institute: Institute of Civil Engineer

Ihamouten, A., Dérobert, X., & Villain, G. (2010). *The effect of coupling on the determination of time zero for radar antennae.* Paper presented at the Proceedings of the XIII International Conference on Ground Penetrating Radar.

Imad A.Q., Wei X. and Roger R. (2010). Optimization of antenna configuration in multiple-frequency ground penetrating radar system for railroad substructure assessment. *NDT&E International*, 43, 20-28.

ISO-5725-1. (1994). Accuracy (trueness and precision) of measurement methods and results - Part 1: General principles and definitions. In: International Organization for Standardization.

J. Baili, S. Lahouar, M. Hergli, I. L. Al-Qadi, K. Besbes (2009). *NDT&E International* 42, 696-703.

Jacob, R. W., & Hermance, J. F. (2005). Random and non-random uncertainties in precision GPR measurements: Identifying and compensating for instrument drift. *Subsurface Sensing Technologies and Applications, 6*(1), 59-71.

Jacob, R. W., & Urban, T. (2016). Ground‐penetrating radar velocity determination and precision estimates using common‐midpoint (CMP) collection with hand‐picking, semblance analysis and cross‐correlation analysis: a case study and tutorial for archaeologists. *Archaeometry, 58*(6), 987-1002.

Jaw, S. W., & Hashim, M. (2013). Locational accuracy of underground utility mapping using ground penetrating radar. *Tunnelling and Underground Space Technology, 35*, 20-29.

JCGM. (2008). Evaluation of measurement data—Guide to the expression of uncertainty in measurement. *JCGM*.

Jiles, D. (2015). Introduction to magnetism and magnetic materials: CRC press.

Jol, H. M. (2009). Ground Penetrating Radar Theory and Applications: Oxford: Elsevier.

Kalhor, H. (1988). Comparison of Ampere's circuital law (ACL) and the law of Biot-Savart (LBS). *IEEE Transactions on Education, 31*(3), 236-238.

Kearey, P., Brooks, M. and Hill, I (2002). An introduction to geophysical exploration, 3rd edition, Blackwell, London, 262 P.

Killinger, D. (2014). Lidar (light detection and ranging). In *Laser Spectroscopy for Sensing* (pp. 292-312): Elsevier.

Kind T. (2008). Study of the Behaviour of a Multi-Offset Antenna Array on Railway Ballast. *GPR Conference 2008*, Birmingham, UK.

Kipnis, N. (2005). Chance in science: The discovery of electromagnetism by HC Oersted. *Science & Education, 14*(1), 1-28.

Klysz, G., & Balayssac, J. P. (2007). Determination of volumetric water content of concrete using ground-penetrating radar. *Cement and Concrete Research, 37*(8), 1164-1171. doi:10.1016/j.cemconres.2007.04.010

Klysz, G., Balayssac, J. P., & Laurens, S. (2004). Spectral analysis of radar surface waves for non-destructive evaluation of cover concrete. *NDT & E International, 37*(3), 221-227. doi:10.1016/j.ndteint.2003.09.006

Knoll, M. D. (1996). A petrophysical basis for ground penetrating radar and very early time electromagnetics: Electrical properties of sand-clay mixtures. University of British Columbia,

Kong, F.-N., & By, T. L. (1995). Performance of a GPR system which uses step frequency signals. *Journal of Applied Geophysics, 33*(1-3), 15-26.

Kubáček, L. (1996). Nonlinear error propagation law. *Applications of Mathematics, 41*(5), 329-345.

Kuikka, S., & Varis, O. (1997). Uncertainties of climatic change impacts in Finnish watersheds: a Bayesian network analysis of expert knowledge. *Boreal Environment Research, 2*, 109-109.

Lai, W.L.W, (2006). *Characterization of porous construction materials using electromagnetic radar wave*. Doctoral thesis, the Hong Kong Polytechnic University, Hong Kong. Retrieved from https://theses.lib.polyu.edu.hk/bitstream/200/2269/1/b20696735.pdf.

Lai W.L., Tsang W.F, Fang H. and Xiao D. (2006). Experimental determination of bulk dielectric properties and porosity of porous asphalt and soils using GPR and a cyclic moisture variation technique. *Geophysics*, 71(4) K93–K102.

Lai W. L. and Tsang W. F. (2008). Characterization of Pore Systems of Air/Water-cured Concrete Using Ground Penetrating Radar (GPR) through Continuous Water Injection. *Construction and Building Materials*, 25(3), 250-256.

Lai, W.L.W, Kind, T., & Wiggenhauser, H. (2011). Using ground penetrating radar and time-frequency analysis to characterize construction materials. *NDT & E International, 44*(1), 111-120.

Lai, W.L.W, Kou, S., & Poon, C. (2012). Unsaturated zone characterization in soil through transient wetting and drying using GPR joint time-frequency analysis and grayscale images. *Journal of Hydrology, 452*, 1-13.

Lai, W.L.W, Tsang, W., Fang, H., & Xiao, D. (2006). Experimental determination of bulk dielectric properties and porosity of porous asphalt and soils using GPR and a cyclic moisture variation technique. *Geophysics, 71*(4), K93-K102.

Lai, W.L.W, Kind, T., & Wiggenhauser, H. (2010). A Study of Concrete Hydration and Dielectric Relaxation Mechanism Using Ground Penetrating Radar and Short-Time Fourier Transform. *EURASIP Journal on Advances in Signal Processing, 2010*(1), 317216. doi:10.1155/2010/317216

Lai, W.L.W, Kind, T., & Wiggenhauser, H. (2011a). Frequency-dependent dispersion of high-frequency ground penetrating radar wave in concrete. *NDT & E International, 44*(3), 267-273. doi:10.1016/j.ndteint.2010.12.004

Lai, W.L.W, Kind, T., & Wiggenhauser, H. (2011b). Using ground penetrating radar and time-frequency analysis to characterize construction materials. *NDT and E International, 44*(1), 111-120. doi:10.1016/j.ndteint.2010.10.002

Lai, W.L.W., Kou, S. C., & Poon, C. S. (2012). Unsaturated zone characterization in soil through transient wetting and drying using GPR joint time-frequency analysis and grayscale images. *Journal of Hydrology, 452-453*, 1-13. doi:10.1016/j.jhydrol.2012.03.044

Lai, W.L.W, Kou, S. C., Tsang, W. F., & Poon, C. S. (2009). Characterization of concrete properties from dielectric properties using ground penetrating radar. *Cement and Concrete Research, 39*(8), 687-695. doi:10.1016/j.cemconres.2009.05.004

Lai, W.L.W, Derobert, X., & Annan, P. (2018). A review of Ground Penetrating Radar application in civil engineering: A 30-year journey from Locating and Testing to Imaging and Diagnosis. *NDT & E International, 96*, 58-78.

Lai, W.L.W, Kind, T., Kruschwitz, S., Wöstmann, J., & Wiggenhauser, H. (2014). Spectral absorption of spatial and temporal ground penetrating radar signals by water in construction materials. *NDT & E International, 67*, 55-63.

Lai, W.L.W, Kind, T., Sham, J. F.-C., & Wiggenhauser, H. (2016a). Correction of GPR wave velocity at different oblique angles between traverses and alignment of line objects in a common offset antenna setting. *NDT and E International, 82*, 36-43. doi:10.1016/j.ndteint.2016.03.003

Lai, W.L.W, Kind, T., Sham, J. F.-C., & Wiggenhauser, H. (2016b). Correction of GPR wave velocity at different oblique angles between traverses and alignment of line objects in a common offset antenna setting. *NDT & E International, 82*, 36-43.

Lai, W.L.W, (2006). Characterization of porous construction materials using electromagnetic radar wave. Doctoral thesis, the Hong Kong Polytechnic University, Hong Kong. Retrieved from https://theses.lib.polyu.edu.hk/bitstream/200/2269/1/b20696735.pdf.

Lai, W.L.W, Chang, R. K. W., Sham, J. F. C., & Pang, K. (2016). Perturbation mapping of water leak in buried water pipes via laboratory validation experiments with high-frequency ground penetrating radar (GPR). *Tunnelling and Underground Space Technology, 52*, 157-167. doi:10.1016/j.tust.2015.10.017

Lambot, S., Rhebergen, J., Van den Bosch, I., Slob, E., & Vanclooster, M. (2004). Measuring the soil water content profile of a sandy soil with an off-ground monostatic ground penetrating radar. *Vadose zone journal, 3*(4), 1063-1071.

Lambot, S., Slob, E., van den Bosch, I., Stockbroeckx, B., Scheers, B., & Vanclooster, M. (2004). Estimating soil electric properties from monostatic ground‐penetrating radar signal inversion in the frequency domain. *Water resources research, 40*(4).

Landau, L. D., Bell, J., Kearsley, M., Pitaevskii, L., Lifshitz, E., & Sykes, J. (2013). *Electrodynamics of continuous media* (Vol. 8): Elsevier.

Lau, K. W., Cheung W. Y., Lai W. L. & Sham F.C. (2021). Characterizing pipe leakage with a combination of GPR wave velocity algorithms. *Tunnelling and Underground Space Technology 109*, 103740.

Laurens S., Balayssac J.P., Rhazi J., Klysz G. and Arliguie G. (2005). Non-destructive evaluation of concrete moisture by GPR: experimental study and direct modeling. *Materials and Structures*, 38, 827-832.

Legislative Council Secretariat (2020). Building Management in Hong Kong. Statistical Highlights ISSH08/20-21. Hong Hong Special Administration Region. Retrieved from https://www.legco.gov.hk/research-publications/english/2021issh08-building-management-in-hong-kong-20201123-e.pdf

Levenberg, K. (1944). A method for the solution of certain non-linear problems in least squares. *Quarterly of applied mathematics, 2*(2), 164-168.

Li, S., Cai, H., Abraham, D. M., & Mao, P. (2016). Estimating features of underground utilities: Hybrid GPR/GPS approach. *Journal of Computing in Civil Engineering, 30*(1), 04014108.

Lindbäck, K. (2015). Hydrology and Bed Topography of the Greenland Ice Sheet: Last known surroundings. Acta Universitatis Upsaliensis,

Lindley, D. V. (2013). *Understanding uncertainty*: John Wiley & Sons.

Liu, H., Xie, X., & Sato, M. (2012). *Accurate thickness estimation of a backfill grouting layer behind shield tunnel lining by CMP measurement using GPR.* Paper presented at the 2012 14th International Conference on Ground Penetrating Radar (GPR).

Ludwig, A. (1971). Near-field far-field transformations using spherical-wave expansions. *IEEE transactions on antennas and propagation, 19*(2), 214-220.

Luo, T. X., Lai, W.L.W, Chang, R. K., & Goodman, D. (2019). GPR imaging criteria. *Journal of Applied Geophysics, 165*, 37-48.

Malaysia, National Mapping and Spatial Data Committee. (2006). Standard guideline for underground utility mapping. In: National Mapping and Spatial Data Committee.

Maxwell, J. C. (1890). The Scientific Papers of James Clerk Maxwell. (Vol. 2). University Press.

Maierhofer Ch and Wöstmann J. (1998). Investigation of dielectric properties of brick materials as a function of moisture and salt content using a microwave impulse technique at very high frequencies. *NDT&E International*, 31(4), 259-263.

McCann D. M. and Forde M. C. (2001). Review of NDT methods in the assessment of concrete and masonry structures. *NDT&E International*, 34(2), 71-84.

Malhotra, V.M. and Carino, N.J. Ed. (2006). *Handbook on Nondestructive Testing of Concrete*, 2nd Ed.

Mendel, J. M. (2000). Uncertainty, fuzzy logic, and signal processing. *Signal Processing, 80*(6), 913-933.

Misra, P., & Enge, P. (2006). Global Positioning System: signals, measurements and performance second edition. *Global Positioning System: Signals, Measurements And Performance Second Editions, 206*.

Mooney, C. Z. (1997). *Monte carlo simulation* (Vol. 116): Sage publications.

Moorman, B. J., & Michel, F. A. (2000). Glacial hydrological system characterization using ground-penetrating radar. *Hydrological Processes, 14*(15), 2645-2667.

Moré, J. J. (1978). The Levenberg-Marquardt algorithm: implementation and theory. In *Numerical analysis* (pp. 105-116): Springer.

Murphy, K. E. (2004). Light detection and ranging (LIDAR) mapping system. In: Google Patents.

Nielsen, L., Looms, M. C., Hansen, T. M., Cordua, K. S., & Stemmerik, L. (2010). Estimation of chalk heterogeneity from stochastic modeling conditioned by crosshole GPR traveltimes and log data. *Advances in near-surface seismology and ground-penetrating radar: SEG Geophysical Development Series, 15*, 379-398.

Nielsen, T. D., & Jensen, F. V. (2009). *Bayesian networks and decision graphs*: Springer Science & Business Media.

Nigel. J. Cassidy (2008). Frequency-dependent attenuation and velocity characteristics of nano-to-micro scale, lossy, magnetite-rich materials. *Near Surface Geophysics*, 2008, 341-354.

Neville A.M. (1995). *Properties of Concrete*, Final ed., Longman.

O'Leary, P. L., & Zsombor-Murray, P. (2004). Direct and specific least-square fitting of hyperbolæ and ellipses. *Journal of Electronic Imaging, 13*(3), 492-504.

P.C. Hewlett and M. Liska, (2019). *Lea's chemistry of cement and concrete*, Oxford: Butterworth-Heinemann, Fifth edition, ISBN: 9780081007952.

Panofsky, W. K., & Phillips, M. (2005). *Classical electricity and magnetism*: Courier Corporation.

Parkinson, B. W., Enge, P., Axelrad, P., & Spilker Jr, J. J. (1996). *Global positioning system: Theory and applications, Volume II*: American Institute of Aeronautics and Astronautics.

Pérez-Gracia, V., González-Drigo, R., & Di Capua, D. (2008). Horizontal resolution in a non-destructive shallow GPR survey: An experimental evaluation. *NDT & E International, 41*(8), 611-620.

PolyU, L. (2019b). Specifications for nondestructive testing, surveying, imaging and diagnosis for underground utilities-1.2 (Ground penetrating radar).

Pongsak W., Raktipong S., Somnuk T. & Nirattaya K. (2017). A new method to determine locations of rebars and estimate the cover thickness of RC structures using GPR data. *Construction and Building Materials 140,* 257-273.

Qian and Chen (1996), *Joint Time-Frequency Analysis, Methods and Applications*, Prentice Hall.

R.J.Oliveira, B. Caldeira, T. Teixido and J.F. Borges (2021). GPR clutter reflection noise-filtering through singular value decomposition in the bidimensional spectral domain. *MDPI, Remote Sens.* 2021, 13, 2005. https://doi.org/10.3390/rs13102005, retrieved from https://www.mdpi.com/journal/remotesensing.

Rating and Valuation Department (2021). Hong Kong Property Review 2021. Hong Hong Special Administration Region. Retrieved from https://www.rvd.gov.hk/en/publications/hkpr.html

Ray, W. (1979). Statistics for Experiments. An Introduction to Design, Data Analysis and Model Building. *Journal of the Royal Statistical Society: Series A (General), 142*(3), 381-382.

Reutebuch, S. E., Andersen, H.-E., & McGaughey, R. J. (2005). Light detection and ranging (LIDAR): an emerging tool for multiple resource inventory. *Journal of Forestry, 103*(6), 286-292.

Reynolds, J. M. (2011). An introduction to applied and environmental geophysics: John Wiley & Sons.

Richards, J. A., & Richards, J. (1999). *Remote sensing digital image analysis* (Vol. 3): Springer.

Ristic, A. V., Petrovacki, D., & Govedarica, M. (2009). A new method to simultaneously estimate the radius of a cylindrical object and the wave propagation velocity from GPR data. *Computers & Geosciences, 35*(8), 1620-1630.

Robert, C., & Casella, G. (2013). *Monte Carlo statistical methods*: Springer Science & Business Media.

S. Laurens, J.P. Balayssac, J. Rhazi, G. Klsz and G. Arliguie (2005). Non-destructive evaluation of concrete moisture by GPR: experimental study and direct modeling. *Materials and Structures*, 38, 827-832.

Sambridge, M., & Mosegaard, K. (2002). Monte Carlo methods in geophysical inverse problems. *Reviews of Geophysics, 40*(3), 3-1-3-29.

Schultz, J. J. (2012). The application of ground-penetrating radar for forensic grave detection. *A companion to forensic anthropology*, 85-100.

Seybold, J. S. (2005). *Introduction to RF propagation*: John Wiley & Sons.

Sham, J. F. C., & Lai, W.L.W (2016). Development of a new algorithm for accurate estimation of GPR's wave propagation velocity by common-offset survey method. *NDT and E International, 83*, 104-113. doi:10.1016/j.ndteint.2016.05.002

Shi, W. (2009). Principles of modeling uncertainties in spatial data and spatial analyses: CRC press.

Shihab, S., & Al-Nuaimy, W. (2005). Radius estimation for cylindrical objects detected by ground penetrating radar. *Subsurface Sensing Technologies and Applications, 6*(2), 151-166.

Silver, S. (Ed.). (1984). Microwave antenna theory and design (No. 19). Iet.

Skolnik, M. I. (1980). *Introduction to radar systems* (Vol. 3): McGraw-Hill New York.

Smithson, M. (2012). *Ignorance and uncertainty: Emerging paradigms*: Springer Science & Business Media.

Snelders, H. A. M. (1990). Oersted's discovery of electromagnetism. *Romanticism and the Sciences*, 228-240.

Solla, M., González-Jorge, H., Lorenzo, H., & Arias, P. (2013). Uncertainty evaluation of the 1 GHz GPR antenna for the estimation of concrete asphalt thickness. *Measurement, 46*(9), 3032-3040.

Soutsos, M.N., Bungey, J.H., Millard, S.G., Shaw, M.R. and Patterson, A. (2001). Dielectric Properties of Concrete and Their Influence on Radar Testing. *NDT&E International*, 34, 419-425.

Steelman, C. M., & Endres, A. L. (2012). Assessing vertical soil moisture dynamics using multi-frequency GPR common-midpoint soundings. *Journal of Hydrology, 436*, 51-66.

Strangway, D. W. (1967). Mineral magnetism. Society of Exploration Geophysicists' Mining Geophysics, 437.

Stutzman, W. L., & Thiele, G. A. (2012). *Antenna theory and design*: John Wiley & Sons.

T. T. Dinh, S. Hegler, M. Liebscher, I. N. Sosa, H. Li, D. Plettemeier, W. G. Drossel and V. Mechtcherine (2021). Dielectric material characterization of concrete in GHz range in dependence on pore volume and water content. *Construction and Building Materials*, 311.

Takahashi, K., Igel, J., & Preetz, H. (2011). Clutter modeling for ground-penetrating radar measurements in heterogeneous soils. *IEEE Journal of Selected Topics in Applied Earth Observations and Remote Sensing, 4*(4), 739-747.

Takahashi, K., Igel, J., & Preetz, H. (2012). Modeling of GPR clutter caused by soil heterogeneity. *International Journal of Antennas and Propagation, 2012*.

Takahashi, K., & Sato, M. (2013). *Imaging of buried structures by a GPR combined with a self-tracking total station.* Paper presented at the Proceedings of the 11th SEGJ International Symposium, Yokohama, Japan, 18-21 November 2013.

Tanikawa, T., Hirano, Y., Dannoura, M., Yamase, K., Aono, K., Ishii, M., . . . Kanazawa, Y. (2013). Root orientation can affect detection accuracy of ground-penetrating radar. *Plant and soil, 373*(1-2), 317-327.

Tannert, C., Elvers, H. D., & Jandrig, B. (2007). The ethics of uncertainty: In the light of possible dangers, research becomes a moral duty. *EMBO reports, 8*(10), 892-896.

Taylor, B. (1969). Methodus Incrementorum Directa et Inversa [Direct and Reverse Methods of Incrementation]. *Pearsonianis: prostant apud Gul. Innys*, 21-23.

Taylor, B. N. (2009). Guidelines for Evaluating and Expressing the Uncertainty of NIST Measurement Results (rev: Diane Publishing.

The Concrete Portal, Cement Chemistry: Hydration of cement. Retrieved from http://www.theconcreteportal.com/cem_chem.html

Tillard, S., & Dubois, J.-C. (1995). Analysis of GPR data: Wave propagation velocity determination. *Journal of Applied Geophysics, 33*(1-3), 77-91.

Tiwari S. & Soni A. (2019). Structure health monitoring of housing project: A case study. *Materials Today: Proceedings 47 (2021),* 3783-3786.

Topp, G. C., Davis, J., & Annan, A. P. (1980). Electromagnetic determination of soil water content: Measurements in coaxial transmission lines. *Water resources research, 16*(3), 574-582.

Travassos, X., Avila, S., Adriano, R. d. S., & Ida, N. (2018). A Review of Ground Penetrating Radar Antenna Design and Optimization. *Journal of Microwaves, Optoelectronics and Electromagnetic Applications, 17*(3), 385-402.

Tsang, L., Kong, J. A., & Shin, R. T. (1985). Theory of microwave remote sensing.

Urbini, S., Vittuari, L., & Gandolfi, S. (2001). GPR and GPS data integration: examples of application in Antarctica.

Von Hippel, A. R., & Morgan, S. (1955). Dielectric materials and applications. *Journal of The Electrochemical Society, 102*(3), 68C.

W. L. Lai and H. Wiggenhauser (2010). A study of concrete hydration and dielectric relaxation mechanism using Ground Penetrating Radar and Short-Time Fourier Transform. *EURASIP Journal on Advances in Signal Processing*, Volume 2010.

W. L. Lai and K. H. Wiggenhauser (2011). Using ground penetrating radar and time-frequency analysis to characterize construction materials. *NDT&E International* 44, 111-120.

W.W.L. Lai, T. Kind, S. Kruschwitz and J. Wostmann (2014). Spectral absorption of spatial and temporal ground penetrating radar signals by water in construction materials. *NDT&E International* 67, 55-63.

Wang, J.R. and Schmugge, T.J. (1980). An Empirical Model for the Complex Dielectric Permittivity of Soils as a Function of Water Content. *IEEE Transactions on Geoscience and Remote Sensing*, GE-18(4), 288-295.

West, L.J. and Handley, K. (2003). Radar Frequency Dielectric Dispersion in Sandstone: Implications for Determination of Moisture and Clay Content. *Water Resources Research*, 39(2), 1026-1037.

William, L. (2007). Fundamentals of geophysics.

Wong, P., Lai, W.L.W, & Sato, M. (2016). *Time-frequency spectral analysis of step frequency continuous wave and impulse ground penetrating radar.* Paper presented at the 2016 16th International Conference on Ground Penetrating Radar (GPR).

Wu, R., Gu, K., Li, J., Bradley, M., Habersat, J., & Maksymonko, G. (2003). Propagation velocity uncertainty on GPR SAR processing. *IEEE Transactions on Aerospace and Electronic Systems, 39*(3), 849-861.

X. Liu, J. Chen, X. Cui, Q. Liu, X. Cao and X.H. Chen (2017). Measurement of soil water content using ground penetrating radar: a review of current methods. *International Journal of Digital Earth*, retrieved from https://www.researchgate.net/publication/321884763.

Xie, F., & Lai, W.L.W. (Under Review). GPR Uncertainty Modelling and Analysis of Object Depth based on Single Trilateration of Ray-paths.

Xie, F., Lai, W.L.W, & Dérobert, X. (Accepted). GPR-based Depth Measurement of Buried Objects based on Constrained Least-square Fitting Method of Reflections.

Xie, F., Lai, W.L.W, & Dérobert, X. (Under Review). GPR Uncertainty Modelling and Analysis of Object Depth based on Constrained Least-square.

Xie, F., Sham, J. F.-C., Lai, W.L.W, & Dérobert, X. (2018). *A modified algorithm for accurate GPR wave velocity estimation with common offset setting antenna.* Paper presented at the 2018 17th International Conference on Ground Penetrating Radar (GPR).

Xie, F., Wu, C. G.-W., Lai, W.L.W, & Sham, J. F.-C. (2018). Correction of multi-frequency GPR wave velocity with distorted hyperbolic reflections from GPR surveys of underground utilities. *Tunnelling and Underground Space Technology, 76*, 76-91.

Xiu, D., & Karniadakis, G. E. (2003). Modeling uncertainty in flow simulations via generalized polynomial chaos. *Journal of computational physics, 187*(1), 137-167.

Yelf, R. (2004). *Where is true time zero?* Paper presented at the Proceedings of the Tenth International Conference on Grounds Penetrating Radar, 2004. GPR 2004.

Yilmaz, Ö. (2001). Seismic data analysis: Processing, inversion, and interpretation of seismic data: Society of exploration geophysicists.

Zhao, S., & Al-Qadi, I. (2017). Pavement drainage pipe condition assessment by GPR image reconstruction using FDTD modeling. *Construction and Building Materials, 154*, 1283-1293.

Zheng, H.-T., Kang, B.-Y., & Kim, H.-G. (2006). An ontology-based Bayesian network approach for representing uncertainty in clinical practice guidelines. In *Uncertainty reasoning for the semantic web I* (pp. 161-173): Springer.